SPACE-TIME KINETICS AND TIME-EIGENFUNCTIONS

by

Yan Cao

A dissertation submitted in partial fulfillment
of the requirements for the degree of
Doctor of Philosophy
(Nuclear Engineering and Radiological Sciences)
in the University of Michigan
2008

Doctoral Committee:

Professor John C. Lee, Chair
Professor James P. Holloway
Professor Edward Larsen
Professor William R. Martin
Professor Kenneth G. Powell

ACKNOWLEDGEMENTS

The author would like to express her special gratitude to Professor John C. Lee, for his invaluable technical and career guidance over the past five years. This thesis would not have been possible without his instructions. Special thanks go to Professor James P. Holloway, Professor Edward Larsen and Professor William R. Martin for their thoughtful suggestions and comments about this thesis. Thanks are also extended to Professor Kenneth G. Powell for serving on the dissertation committee.

The author is also thankful to Dr. Viktoriya V. Kulik and Dr. David Villamarín Fernández for their assistance. Thanks also go to Dr. Gerardo Aliberti at the Argonne National Laboratory for his assistance in using the ERANOS computer code.

Thanks also go to the faculty, the staff and the students in the Nuclear Engineering and Radiological Sciences department for their goodwill and friendship. Special thanks go to the Barbour scholarship program at the University of Michigan, the OScillations in Minerve of isOtopes in "Eupraxic" Spectra Experiments project, the Reactor-Accelerator Coupling Experiment (RACE) project and the Advanced Fuel Cycle Initiative (AFCI) of the U.S. Department of Energy for their financial support.

The author would like to thank her husband, Dan Xu, for his precious love and support. The deepest gratitude also goes to the author's families for their understanding and full support.

TABLE OF CONTENTS

CHAPTER

LIST OF FIGURES

Figure

LIST OF TABLES

LIST OF APPENDICES

Appendix

CHAPTER I

Introduction

1.1 Nuclear Energy and Nuclear Wastes

In the past sixty years, nuclear energy has greatly supported the growing economy of the world. According to the latest data from the International Atomic Energy Agency (IAEA), there are currently 439 commercial nuclear power plants in operation, with a total capacity of 372.202 GWe and supplying 16% of the total electric energy demand of the world. Meanwhile, to support a continuously expanding economy, 34 new nuclear power plants with a total capacity of 28.193 GWe are under construction, with more than half of them being built in China, India and Russia [1]. As nuclear energy continues to be one of the most important energy sources, two of the main potential road-blocks for the further development of the nuclear energy industry are its ability for sustaining long-term energy production and the nuclear waste management.

In the earth's crust, uranium is a widely spread radioactive metal. Its abundance is about 3 ppm (parts per million), which is 500 times larger than gold, and it can be found in rocks, soils, rivers and sea water. The average abundance of the uranium ore is only about 0.25% in the United States, and the ore is usually manufactured into the so-called "yellow cake", which contains about 70% - 90% of U_3O_8. Therefore, to obtain 1 ton of natural uranium, it requires more than 400 tons of uranium ore. Typically, 99% of the uranium ore, which contains almost all the radioactivity and residual materials, are left as mine tailings, creating a large inventory of low-level nuclear wastes [2, 3].

Natural uranium contains two major isotopes ^{235}U and ^{238}U with the abundance of 0.7204% and 99.274% respectively [4]. ^{235}U is an even-old isotope and is fissionable by absorbing an external neutron with any kinetic energy. However, ^{238}U is only fissionable with neutrons, which kinetic energy is larger than roughly about 1 MeV. Other even-odd atoms such as ^{233}U and ^{239}Pu are very similar to ^{235}U. They are often called fissile materials. ^{232}Th, ^{238}U and ^{240}Pu, which have an energy threshold to undergo fission, are called fertile materials. The probability for an atom to undergo fission by absorbing an external neutron is dependent on the neutron energy, and usually the probability is larger for fissile materials interacting with thermal neutrons. Therefore, most of the current nuclear power plants are thermal reactors, which use light materials such as water, heavy water or carbon to slow down fast neutrons, so as to maximize the probability of fission reactions in a nuclear reactor. ^{235}U is the major fuel isotope utilized in current nuclear power plants. Its concentration in a typical nuclear fuel rod is about 3.5%-5%, and it is enriched from natural uranium. The depleted uranium left from the enrichment process is a source of low-level nuclear wastes, which need to be buried in specific repositories.

A nuclear fuel rod is irradiated in the nuclear power plant. After 12-24 months, it is discharged from the nuclear power plant with about 1% ^{235}U left, together with 95% of ^{238}U, 3% of fission products and others materials. For a typical fission reaction [2]

$$ {}_0^1\mathrm{n} + {}^{235}\mathrm{U} \rightarrow \left({}^{236}\mathrm{U}\right)^* \rightarrow \quad \text{fission} \quad \text{products}, \tag{1.1} $$

where the fission products are usually highly radioactive. Meanwhile, fertile nuclei in the fuel rods can also absorb neutrons to form fissile nuclides, e.g.,

$$ {}_{0}^{1}\mathrm{n} + {}^{238}\mathrm{U} \rightarrow \left({}^{239}\mathrm{U}\right)^{*} \rightarrow {}^{239}\mathrm{Pu} + \gamma. \tag{1.2} $$

With successive neutron absorptions, heavier radioactive nuclides with long half-lives, e.g., Pu, Am, and Cm, are built up in the fuel rods before the fuel is discharged from the reactor. For a typical nuclear power plant with an initial loading of 1 ton of ^{235}U, there will be roughly 250 kg of ^{235}U and 22.7 tons of ^{238}U left in the spent fuel. In addition, 266 kg of Pu will also be generated, together with about 946 kg of fission products and other minor actinides in the spent fuel rods [5]. Due to the high radioactivity of the discharged fuel rods, they are classified as high-level nuclear wastes and are required to be further processed or be stored in a geological repository, such as the Yucca Mountain repository.

The extent of the nuclear power industry and the insufficient use of uranium with current nuclear power technologies could result in an eventual shortage of nuclear fuel supplies. Specifically, a typical fission reaction produces about 200 MeV energy. Thus, a 1.0 GWe nuclear power plant with a capacity factor of 80% consumes about 1 ton of ^{235}U annually [5]. According to the British Geological Survey, the total known and economically recoverable uranium in the world is about 4,743,000 tons in 2007 [6], which may last less than 150 years with the current rate of consumption. Although it is possible to find more uranium ores with new exploration technologies, a safe disposal of nuclear waste, and the production of plutonium in nuclear power plants, with weapons proliferation potential, are critical issues which have to be addressed in the near future.

A geological repository is a potential way of solving the nuclear waste problem. Regardless of the high cost of building such a repository, if all the spent nuclear fuel is vitrified and stored, the cumulated amount of spent nuclear fuel will reach about 200,000 tons by the year of 2020, which will fill up 3 Yucca Mountain repositories, each with the capacity of 70,000 metric tons [5, 7]. Another possible way to solve the nuclear waste problem is to reprocess the spent nuclear fuel and transmute the radioactive nucleus in advanced reactors. The fuel reprocessing separates out Pu and burns it up in nuclear reactors, and the transmutation technology transfers long-lived radioactive nuclides to stable or short-lived nuclides.

The goal of reprocessing and transmutation is to destroy plutonium and other actinides as much as possible. This technology can also help lower the requirements for the geological repository. To illustrate, we show in Figure 1.1 the relative radiotoxicity of spent nuclear fuel with or without actinides [8, 9]. With actinides separated out from the spent fuel, the life time of the engineering barrier to prevent the radioactive nuclides from leaking out of the repository may be reduced from millions of years to less than a thousand years. As a result, many technical requirements for designing the geological repository can be simplified. For instance, materials such as borosilicate glass are known to be durable for thousands of years and will then serve as a good waste form for the nuclear waste.

1.2 The ADS system

In a nuclear reactor, the destruction rate of actinides is often dependent on the neutron energy spectrum of the reactor. Usually, a fast neutron spectrum is more attractive in terms of incinerating Pu and other actinides, due to the fact that fast neutrons can induce fission interactions with the actinides to supply additional neutrons in a fast reactor [10]. The Accelerator Driven Subcritical (ADS) system is one type of reactor which has been investigated in the past decades to incinerate actinides

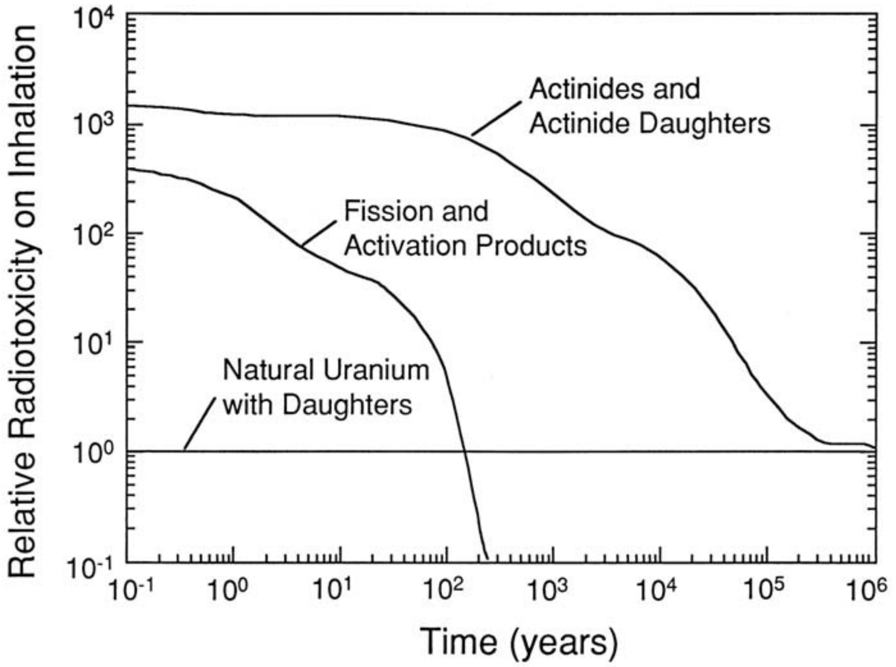

Figure 1.1: Relative radiotoxicity on inhalation of spent nuclear fuel with a burnup of 38 megawatt days/kg U. The radiotoxicity values are relative to the radiotoxicity (horizontal line) of the quantity of uranium ore that was originally mined to produce the fuel (eight tons of natural uranium yields one ton of enriched uranium, 3.5% ^{235}U).[8]

and to transmute long-lived radioactive nuclides. The nuclear fuel configuration is subcritical, and an external neutron source is placed in the reactor to support a steady power level in the ADS reactor.

Figure 1.2 shows a design of an ADS system, which has three major components: an accelerator, a neutron target and a subcritical reactor. In this conceptual design, protons are first accelerated with an energy up to GeV by a linear accelerator. The high-energy proton beam hits the neutron target which is located at the center of a subcritical core to generate high-energy neutrons. The neutrons then leak out of the target region and interact with nuclear fuels to produce energy.

Compared with critical reactors, where the fission chain is self-sustained, the advantage of using such a subcritical system lies in the inherent safety feature of a subcritical reactor. Specifically, the reactor power is fully determined by the intensity

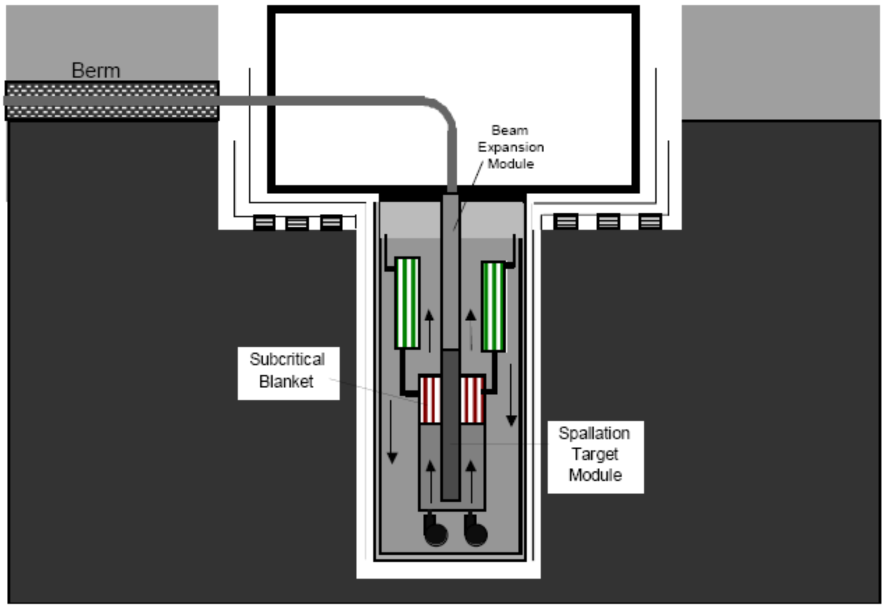

Figure 1.2: A reference core of the ADS system [11].

of the external neutron source, and the system can be shut down easily by simply turning off the accelerator. Due to this inherent safety feature, it is also possible to incinerate the minor actinides, which have small delayed neutron fractions and may be difficult to serve as fuel for critical reactors [5]. In addition, long-lived fission products, e.g. ^{99}Tc and ^{129}I, can also be transmuted in such a system with external neutrons.

The accelerator in the ADS system has to be operated with a high level of performance, in order to maintain a steady power level to the electric grid and to avoid frequent thermal transients. Usually only the linear accelerator is possible to supply such a high energy beam with large intensities. The major technical challenge for the neutron target is to achieve a high production rate of neutrons as well as the management of the high thermal power generated in the target.

Overall, as an integrated system, the ADS system also requires an optimization design on the safety control of the reactor power and the subcritical level of the reactor. Namely, to retain the advantages over critical reactors, the subcritical reactor must be designed to remain subcritical during any transient conditions. As the neutron physics is quite different between subcritical and critical reactors, tools such as numerical simulation code packages and experimental methods which were used in conventional critical reactors have to be verified and validated before they are applied to analyze the ADS system.

1.3 The MUSE (MUltiplication avec Source Externe) experimental program

In the nuclear engineering field, a critical reactor often means that if we freeze the reactor at any moment, the number of neutrons generated by fission or other interactions in the reactor is equal to the number of neutrons destructed by absorption and other processes such as neutrons leaking out of the system. The effective multiplication factor k_{eff} is used to measure the degree of a reactor deviating from its critical status. Conceptually, k_{eff} can be defined as a scalar, such that if the number of neutrons generated by each fission interaction is scaled by this number, the reactor is then artificially critical. Thus, k_{eff} is a global parameter which characterizes the behavior of the entire reactor [12]. In practical applications, another global parameter named as reactivity ρ is also used for convenience. It is defined as $\rho = (k_{eff} - 1)/k_{eff}$.

One of the conventional methods, which was used to measure k_{eff} or ρ for reactors not far from critical status, e.g., $k_{eff} \sim 0.99$, is the pulsed-neutron experiment. To perform the experiment, external neutrons are pulsed into the reactor. Detectors, usually ^{235}U fission chambers, are placed at certain positions in the reactor to monitor the decay of the neutron flux. The reactivity are then inferred from the measured detector responses, based on the α-method or the area-ratio method. Usually, for close-to-critical reactors, the measured reactivities obtained from the local observations are not sensitive to detector positions, and their values are close to the real ρ of the reactor. However, for sufficiently subcritical reactors, e.g., $k_{eff} \sim 0.95$, both methods have to be examined and validated carefully.

The MUSE program is in the 5^{th} European framework to study the reactor physics of the ADS system [13]. Specifically, it performs a series of zero-power pulsed-neutron experiments with the goal of improving the current understanding of the kinetics behavior of a subcritical reactor. More importantly, the program also aims to validate experimental methods which could be used to measure the reactivity of a subcritical reactor.

The MUSE program started in 1995 and was led by the French Atomic Energy Commission (CEA, Commissariat l'nergie atomique) in cooperation with other European countries. Experiments were performed in the MASURCA facility, which is a fast research reactor located at Cadarache, France. Figure 1.3 shows the X-Y and Y-Z views of a Monte Carlo model of this subcritical reactor.

In the 4^{th} phase of the MUSE program, the deuterons are accelerated by a GENEPI accelerator with an average energy about 250 keV [14], and are focused and delivered through a small window opening at the middle plane of the subcritical reactor, as shown as the white region in the X-Y and Y-Z views. The neutron target is a 50 mm thick copper disk placed at the center of the subcritical reactor, with titanium doped with deuterium or tritium [15]. A lead buffer shown as an orange region in both figures is placed at the back of the neutron target to simulate the neutron spectrum from a spallation neutron source. Therefore, the external neutron source can be assumed as an isotropic source.

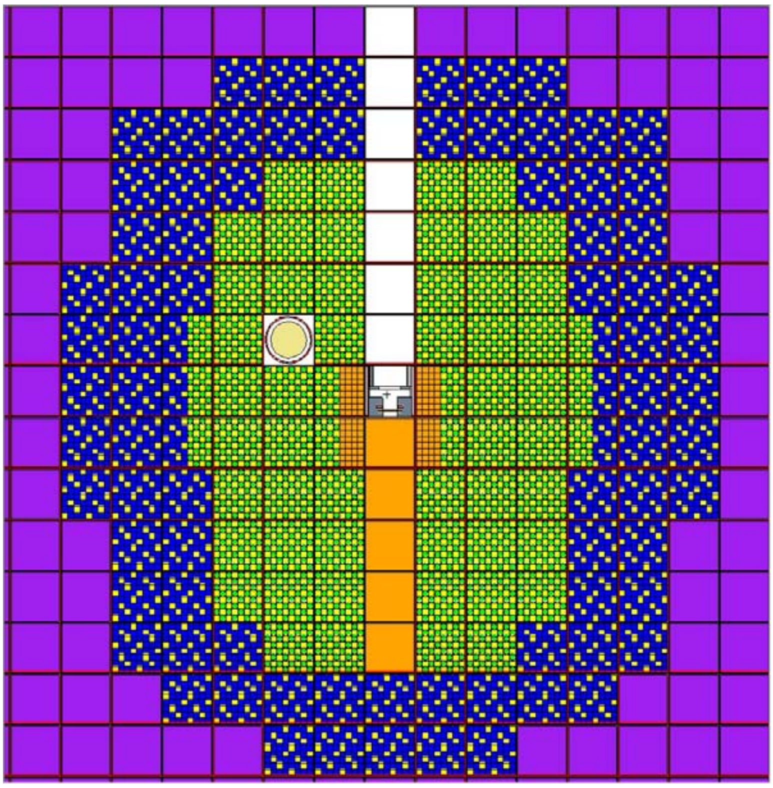

(a) X-Y view

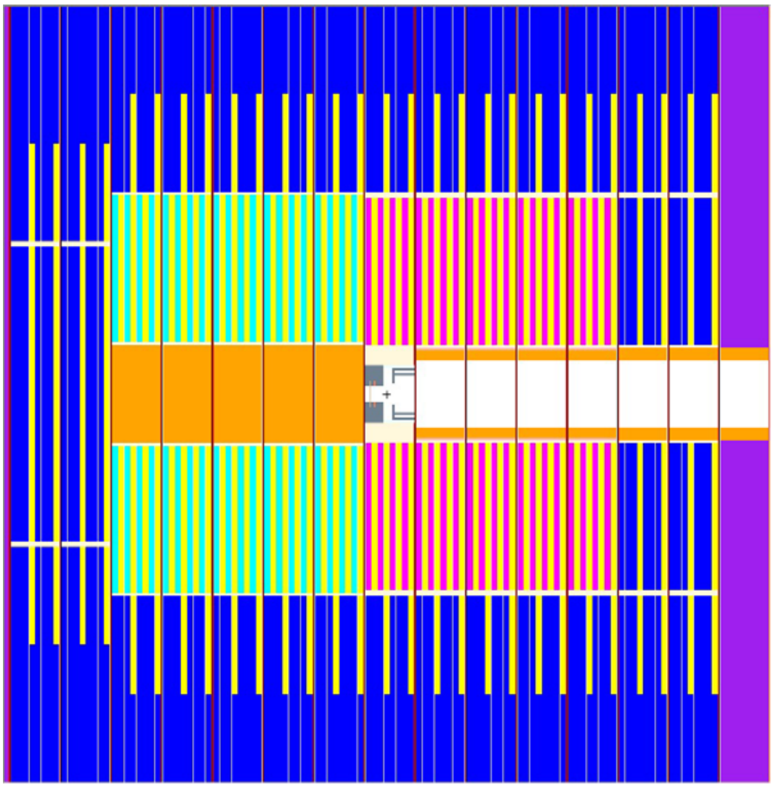

(b) Y-Z view

Figure 1.3: A Monte Carlo model of the MUSE-4 SC0 MASURCA research reactor (a) X-Y view at plane $z = 0$ (b) Y-Z view at $x = 0$.

The subcritical reactor uses U-Pu mixed oxide (MOX) fuel. Dimensions of each fuel subassembly are 0.106 × 0.106 × 1.642 m, and is composed of fuel pellets and metal sodium in a steel wrapper shown as the left plot in Figure 1.4. With different Pu concentrations in the MOX fuel, the fuel rods are marked as green, cyan, and magenta regions in the X-Y and Y-Z view, respectively. The reactor is cooled by nature circulation of air. The solid sodium rods, marked as yellow regions in the Monte Carlo model, are placed in the fuel subassembly to simulate the neutron spectrum of a sodium cooled fast reactor. The Monte Carlo model of the reflector region is also shown as the right plot in Figure 1.4. Each reflector subassembly also consists of solid sodium rods and steel blocks. The purple region as shown in the X-Y view is stainless steel which acts as the shield of the subcritical reactor. Finally, control rods, which are usually a strong neutron absorber, e.g., B_4C, can be inserted into the reactor as shown in the X-Y view.

In the MUSE-4 program, pulsed-neutron experiments are performed to evaluate the applicability of both the α-method and the area-ratio method in measuring the reactivity of an ADS system. The pulsed-neutron source is either a D-T or a D-D source generated by the GENEPI accelerator, which works at a frequency of 1 Hz. The average energy of the external neutron source is 14 MeV for the D-T source and 2.5 MeV for the D-D source. The source intensities are 3.3×10^6 n/pulse and 3.0×10^4 n/pulse for the D-T and D-D sources, respectively. The subcritical reactor is at different configurations, e.g., SC0, SC2, and SC3, by arranging the fuel assemblies. In addition, by placing the four safety rods vertically at different positions, the reactor can also achieve different subcritical levels, e.g., the SC0 close-to-critical configuration with $\rho = -500$ pcm and the SC0 subcritical configuration with $\rho = -3000$ pcm. The Monte Carlo model shown in Figure 1.3 is the SC0 subcritical configuration with the control rod SR1 inserted into the reactor.

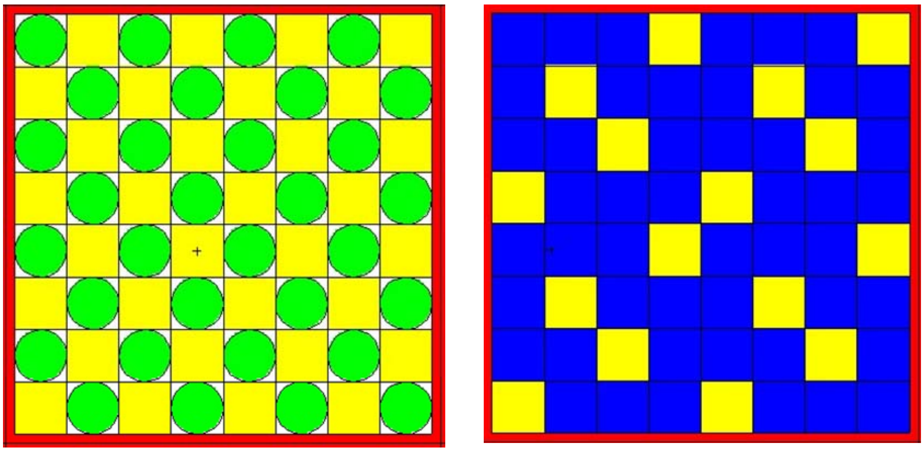

Figure 1.4: A Monte Carlo model of the nuclear fuel subassembly and the reflector subassembly.

1.4 The objective and the structure of the thesis

The MUSE-4 pulsed-neutron experimental data were analyzed explicitly by Villamarin in his PhD thesis [15]. Overall, for the MUSE-4 SC0 subcritical configurations, the reactivity obtained from both the α-method and the area-ratio method are sensitive to detector positions. In particular, with the area-ratio method, the maximum difference between the reactivities measured at different detector positions is about 2 \$, with an average value of about -12 \$ and the measured effective delayed neutron fraction $\beta = 0.00334 \pm 0.00006$. For subcritical reactor configurations with large subcriticality, the α-method becomes difficult to be applied to the experimental data.

To investigate the spatial effects in the MUSE-4 experimental data, Carta et al. reproduced the spatially dependent reactivities from the numerical simulations at most of the detector positions using the area-ratio method [16]. However, Carta's analysis can not reproduce the measured reactivity, which possesses the largest spatial effect. Furthermore, the reason that the reactivities obtained from both the α-method and the area-ratio method are spatially dependent in the MUSE-4 pulsed-neutron experiments is not explained in his paper.

Recently, another type of spatial correction method called the modified area-ratio method was also proposed by Kulik [17] to analyze the spatial effects in the MUSE-4 experiments. The method eliminates spatial effects in the experiments through direct time-dependent numerical simulations of the pulsed-neutron experiment. The method was demonstrated by the numerical tests to be capable of obtaining consistent reactivities at different detector positions. However, the modified area-ratio method requires a numerical simulation of thousands of neutron pulses, making a spatial correction with such a method impractical to the MUSE-4 area-ratio experimental data.

The area-ratio method is one of the traditional methods to measure the reactivity of a close-to-critical reactor. Its spatial dependence in a subcritical reactor was also studied over the years. For instance, Gozani in 1962 introduced the extrapolated area-ratio method [18] to eliminate the spatial effects induced by high-order prompt-neutron harmonics. However, later pulsed-neutron experiments performed by Master et al. [19] showed that the reactivity obtained from the extrapolated area-ratio is even more sensitive to the detector positions than the original area-ratio method. Therefore, the importance of the high-order prompt-neutron harmonics in the area-ratio method was extensively studied [20, 21]. The basic approach is to expand the detector responses with a set of modal terms to obtain a spatial correction f at each detector position with all the high-order harmonics included. For instance, Preskitt et al. first applied the modal expansion technique to the extrapolated area-ratio method [22], and discovered that the spatial effects of the extrapolated area-ratio method are strongly dependent on the “kinetics distortion” factor in the subcritical reactor. In practical applications, due to the difficulty of obtaining high-order prompt-neutron harmonics, the contributions of high-order prompt-neutron harmonics to the spatial correction factor f are ignored, and most of the spatial correction factors are only made based on the fundamental mode [23, 22].

Another approach to study the spatial effects in the area-ratio method was suggested by Bell[24]. In particular, the spatial dependence of the area-ratio method can be obtained directly from steady-state numerical simulations. For practical purposes, the spatial correction factor derived from Bell's method is easy to apply because it does not require any dynamics simulations of the pulsed-neutron experiment. It is this method that Carta used in his paper to reproduce the MUSE-4 area-ratio experimental data [16].

To eliminate the spatial effects in the area-ratio method rather than to reproduce the experimental result, we will derive a spatial correction factor f from Bell's method in this thesis. The capability for f to eliminate the spatial effects in the area-ratio method will be validated by numerical tests. However, with f derived from Bell's method, we are still unable to explain why the reactivity obtained from the area-ratio method is spatially dependent in a subcritical reactor.

According to modal analysis methods, the spatial effects are known to be induced by the high-order harmonics contaminations. In this thesis, we apply the modal expansion technique to the area-ratio method. Specifically, spatial correction factors corresponding to the high-order harmonics are derived and compared with the spatial correction factor f obtained from Bell's method. To explicitly evaluate the spatial effects induced by the high-order harmonics, we first use the Krylov subspace method to calculate the high-order harmonics. Therefore, the spatial effects induced by high-order contaminations can be evaluated by the numerical tests. In addition, a new spatial correction factor f_p with all the high-order prompt-neutron harmonics included is also derived from our modal analysis. With this new spatial correction factor f_p, we are able to both correct and explain the spatial dependence in the MUSE-4 area-ratio experimental data.

The α-method is another traditional method to measure the reactivity from a pulsed-neutron experiment. To apply the method, the detector responses subject to a neutron pulse is fitted by the exponential decay in the prompt-neutron decay region to obtain a decay constant. The reactivity is then obtained with the decay constant and the mean generation time Λ measured from the experiment. If the decay constant is position dependent, the reactivity obtained from the α-method is spatially dependent. For the MUSE-4 experimental data, it is found that for deep subcritical reactor, the decay constants vary continuously over the time and space domains. Therefore, the traditional α-method is difficult to apply. In recent years, the modified α-method was proposed by Kulik to eliminate the spatial effects in the α-experimental data[17]. Like the modified area-ratio method, the spatial effects are eliminated by direct numerical simulations of the pulsed-neutron experiment. However, the modified α-method only requires numerical simulation for a single neutron pulse. In this thesis, we will also use this method to obtain reactivities from the MUSE-4 experimental data. The only drawback of the modified α-method is that its accuracy depends highly on the accuracy of the numerical model.

On the other hand, the reactivity obtained from the traditional α-method might be significantly underestimated, even though it is not sensitive to the detector position. It is because the mean generation time Λ is usually measured in a reference reactor, which might be significantly different from the mean generation time in a subcritical reactor. With prompt-neutron harmonics calculated via Krylov subspace methods, we are able to examine the variation of the mean generation time explicitly for reactors at different subcritical levels through numerical simulations. In addition, the spatial dependence of the decay constants can be easily explained by the modal analysis approach, and a method of eliminating the spatial dependence in the MUSE-4 pulsed-neutron experiment is also proposed in this thesis.

In summary, we apply numerical simulations to the pulsed-neutron experiments to analyze the spatial effects. The space- and time-dependent neutron balance equation is usually solved in the numerical simulations. The rest of the thesis is organized as follows. In Chapter II, we start with a derivation of the time-dependent neutron balance equation. Two eigenvalue problems, of which the eigenfunctions are the expansion functions in the our modal analysis, will be derived explicitly. We also derive the area-ratio method and the traditional α-method in Chapter III from the point kinetics equations for the pulsed-neutron experiments. Then, Chapter IV focuses on analyzing the spatial effects both in the area-ratio method and in the α-method. The spatial correction factor f will be derived from Bell's method. The modal expansion technique is applied to the area-ratio method, and correction factors corresponding to the prompt-neutron harmonics are also derived from the modal analysis. In addition, we also derive the α-method from the time-dependent neutron balance equations, with a calibration factor for the mean generation time Λ. Then, in Chapter V, we present our implementation of the Krylov subspace method to calculate the high-order harmonics of the two eigenvalue problems. In Chapter VI, the spatial correction factors derived in Chapter IV are verified with FX2-TH numerical simulations. The spatial effects induced by the high-order harmonics in the area-ratio method are evaluated via the modal expansion method. The variation of the mean generation time is also evaluated. Finally, in Chapter VII, the spatial effects in the MUSE-4 experimental data are analyzed for both the area-ratio method and the α-method. We present a summary and conclusions of the thesis in Chapter VIII, with several numerical algorithms detailed in Appendices A and B. The four-group cross sections of a FX2-TH numerical model in Chapter VI are included in Appendix C.

CHAPTER II

The Space-Time Kinetics

2.1 The time-dependent neutron balance equation

The time-dependent transport or diffusion equation characterizes the overall reactor behavior and can be obtained by setting up a neutron balance [24] in a differential element $dVdEd\mathbf{\Omega}$ as shown in Figure 2.1,

$$\begin{aligned}\text{Rate of change of the number of neutrons} &= \text{rate of neutron production} \\ &- \text{rate of neutron destruction.} \quad (2.1)\end{aligned}$$

We denote the angular neutron number density $N(\mathbf{r}, E, \mathbf{\Omega}, t)$ to represent the number density of neutrons at time t, in unit volume around position $\mathbf{r}$, unit energy interval at E and unit solid angle around direction $\mathbf{\Omega}$. The rate of change of the number of neutrons in a volume element dV at $\mathbf{r}$, within dE at E, within $d\mathbf{\Omega}$ at $\mathbf{\Omega}$, and at time t can be written as

$$\text{Rate of change of the number of neutrons} = \frac{\partial N(\mathbf{r}, E, \mathbf{\Omega}, t)}{\partial t} dVdEd\mathbf{\Omega}. \qquad (2.2)$$

Neutrons will be removed from the volume element dV by leaking out through the surfaces or leaving $d\mathbf{\Omega}dE$ by colliding. We use the operator $\mathbf{L}(\mathbf{r}, E, \mathbf{\Omega}, t)$ to represent

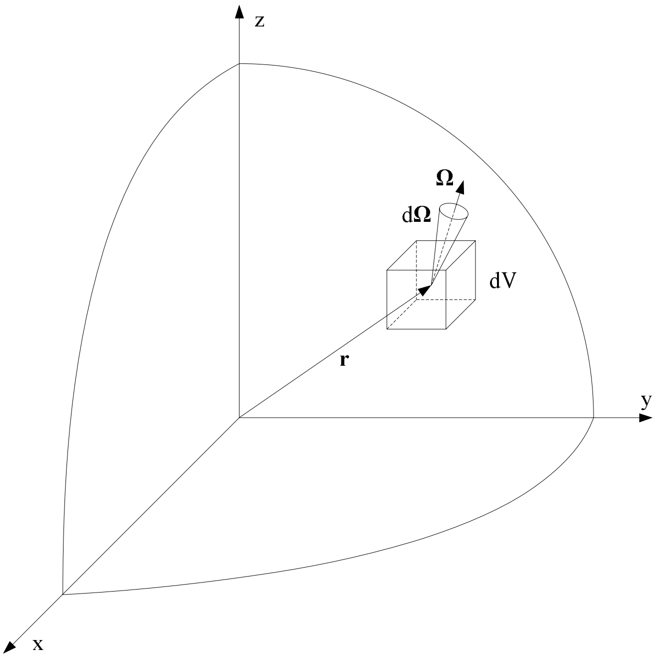

Figure 2.1: A schematic review of the volume element in the reactor.

the neutron destruction process in $dVdEd\Omega$ at time t:

$$\begin{aligned}\mathbf{L}(\mathbf{r},E,\mathbf{\Omega},t)vN(\mathbf{r},E,\mathbf{\Omega},t)dVdEd\mathbf{\Omega} &= v\mathbf{\Omega}\cdot\nabla N(\mathbf{r},E,\mathbf{\Omega},t)dVdEd\mathbf{\Omega} \\ &+ \Sigma_t(\mathbf{r},E,t)vN(\mathbf{r},E,\mathbf{\Omega},t)dVdEd\mathbf{\Omega}, \quad (2.3)\end{aligned}$$

where the first term on the RHS representing the leakage rate, and the second term representing the neutron collision rate. Here, Σ_t is the total cross section of the material at $(\mathbf{r},E,t)$, and v is the neutron speed. Meanwhile, in the volume element dV, neutrons are scattered into $d\mathbf{\Omega}dE$ from $d\mathbf{\Omega}'dE'$, and the scattering process is denoted by the operator $\mathbf{S}$ with

$$\begin{aligned}\mathbf{S}(\mathbf{r},E,t)vN(\mathbf{r},E,\mathbf{\Omega},t)dVdEd\mathbf{\Omega} &= \int_{4\pi}d\mathbf{\Omega}'\int_0^\infty dE'\Sigma_s(\mathbf{r},E'\to E,\mathbf{\Omega}'\to\mathbf{\Omega},t) \\ &\times v'N(\mathbf{r},E',\mathbf{\Omega}',t)dVdEd\mathbf{\Omega}. \qquad (2.4)\end{aligned}$$

Most importantly, neutrons are also generated from neutron fission reactions in $dVd\mathbf{\Omega}dE$ represented by the operator $\mathbf{F}$:

$$\begin{aligned}\mathbf{F}(\mathbf{r},E,t)vN(\mathbf{r},E,\mathbf{\Omega},t)dVdEd\mathbf{\Omega} &= \frac{1}{4\pi}\int_{4\pi}d\mathbf{\Omega}'\int_0^\infty dE'\nu\Sigma_f(\mathbf{r},E',t) \\ &\times\; v'N(\mathbf{r},E',\mathbf{\Omega}',t)dVdEd\mathbf{\Omega}, \qquad (2.5)\end{aligned}$$

where ν is the average number of fission neutrons released per fission. In a typical fission reaction, most of fission neutrons are released promptly within 10^{-14} s, e.g.,

$$^{235}\mathrm{U} +_0^1 \mathrm{n} \longrightarrow {}^{87}\mathrm{Br} + {}^{146}\mathrm{Ln} + 3_0^1\mathrm{n} + \gamma. \qquad (2.6)$$

These neutrons are often called prompt neutrons. There is also a small fraction of fission neutrons, less than 1%, which are released from fission products after beta decays, e.g.,

$$^{87}\mathrm{Br} \xrightarrow[T=55s]{\beta} \left(^{87}\mathrm{Kr}\right)^* \rightarrow {}^{86}\mathrm{Kr} +_0^1 \mathrm{n}. \qquad (2.7)$$

These neutrons are called delayed neutrons, and their release time is determined by the half-life of the beta decay process ranging from less than a second to a minute [2]. Fission products, such as ^{87}Br in this example, are called the delayed-neutron precursors. For a nuclear fission reaction, a multitude of delayed-neutron precursors are produced. For convenience, they are grouped into six groups according to their half-lives. If the fraction of precursors generated per fission for the i^{th} precursor group is denoted as β_i, the average number of prompt neutrons generated from each fission reaction is then $(1-\beta)\,\nu$ with $\beta = \sum_i \beta_i$. Therefore, the neutron production rate in $dVd\mathbf{\Omega}dE$ at time t can be obtained as

$$\begin{aligned}\text{rate of neutron production} &= S(\mathbf{r},E,\mathbf{\Omega},t)vN(\mathbf{r},E,\mathbf{\Omega},t)dVdEd\mathbf{\Omega}\\ &+ (1-\beta)\,\chi_p(E)\mathbf{F}(\mathbf{r},t)vN(\mathbf{r},E,\mathbf{\Omega},t)dVdEd\mathbf{\Omega}\\ &+ \sum_{i=1}^{6}\chi_{d,i}(E)\lambda_i C_i(\mathbf{r},t)dVdEd\mathbf{\Omega}\\ &+ Q(\mathbf{r},E,\mathbf{\Omega},t)dVdEd\mathbf{\Omega}, \end{aligned} \tag{2.8}$$

where χ_p is the prompt neutron spectrum, and $\chi_{d,i}$ is the delayed-neutron spectrum for the i^{th} precursor group. We also introduce C_i as the number density of the i^{th} precursor group with decay constant λ_i, and Q as the external source.

Finally, the continuous neutron transport equation can be obtained by inserting Equations 2.2 through 2.5 and Equation 2.8 back into Equation 2.1 and cancelling $dVdEd\mathbf{\Omega}$ on both sides:

$$\frac{\partial N}{\partial t} + \mathbf{L}vN = \mathbf{S}vN + (1-\beta)\,\chi_p\mathbf{F}vN + \sum_{i=1}^{6}\chi_{d,i}\lambda_i C_i + Q. \tag{2.9}$$

where λ_i is the decay constant of the i^{th} precursor group. In practice, the angular neutron flux defined as $\Phi(\mathbf{r},E,\mathbf{\Omega},t) = vN(\mathbf{r},E,\mathbf{\Omega},t)$ is used more often than N, and the neutron transport equation can be rewritten as

$$\frac{1}{v}\frac{\partial \Phi}{\partial t} + \mathbf{L}\Phi = \mathbf{S}\Phi + (1-\beta)\,\chi_p\mathbf{F}\Phi + \chi_d\lambda C + Q. \tag{2.10}$$

For convenience, we will only include one group of precursor density function, and any equations we derive later can be easily extended into a six-group formulation.

Similar to the neutron balance equation, a balance equation for the precursor density $C(\mathbf{r},t)$ can also be derived as

$$\frac{\partial C(\mathbf{r},t)}{\partial t} + \lambda C(\mathbf{r},t) = \beta\int_{4\pi} d\mathbf{\Omega}\mathbf{F}(\mathbf{r},E,t)\Phi(\mathbf{r},E,\mathbf{\Omega},t), \tag{2.11}$$

where the second term on the LHS stands for the destruction rate of the delayed-neutron precursors, and the RHS stands for the production rate of the precursors in unit volume at $\mathbf{r}$ and at time t.

In a nuclear reactor, the destruction operator $\mathbf{L}$, the scattering operator $\mathbf{S}$ and the fission production operator $\mathbf{F}$ are determined by the material properties of the reactor. They can be time-dependent functions as the temperatures of the materials change in the reactor or due to actual time-dependent changes in the material compositions. Pulsed-neutron experiments are performed in a subcritical reactor operated at "zero-power". Thus, in the rest of this thesis, these operators are assumed to be time independent. Additionally, we will also integrate the transport equations over Ω for the 4π sphere and obtain the time-dependent diffusion equations:

$$\begin{aligned}\frac{1}{v}\frac{\partial\phi(\mathbf{r},E,t)}{\partial t}+\mathbf{L}(\mathbf{r},E)\phi(\mathbf{r},E,t) &= (1-\beta)\,\chi_p(E)\mathbf{F}(\mathbf{r},E)\phi(\mathbf{r},E,t)\\ &+ \chi_d(E)\lambda C(\mathbf{r},t)+Q(\mathbf{r},E,t), \qquad (2.12)\\ \frac{\partial C(\mathbf{r},t)}{\partial t}+\lambda C(\mathbf{r},t) &= \beta\mathbf{F}(\mathbf{r},E)\phi(\mathbf{r},E,t), \qquad (2.13)\end{aligned}$$

where the scalar flux is defined as $\phi(\mathbf{r},E,t)=\int_{4\pi}d\mathbf{\Omega}\Phi(\mathbf{r},E,\mathbf{\Omega},\mathbf{t})$, and the scattering term is combined into the destruction operator $\mathbf{L}$. The methodologies we will use in this thesis are valid both with the diffusion and transport equations. For simplicity, we will use the diffusion equations for the rest of the thesis unless otherwise indicated.

2.2 The static k-eigenfunctions and the α-eigenfunctions

In Chapter I, we defined the multiplication factor k_{eff} such that if the number of neutrons generated by each fission interaction is scaled by k_{eff}, the reactor is then artificially critical, i.e., time-independent. With the time-dependent neutron diffusion equation derived above, we can then obtain a mathematical definition of k_{eff} by setting all the time-derivatives to zero for a source free medium, and eliminating the precursor density function $C(\mathbf{r},t)$ from the equation:

$$\mathbf{L}\phi_k(\mathbf{r},E) = \frac{1}{k}\chi(E)\mathbf{F}\phi_k(\mathbf{r},E), \tag{2.14}$$

where $\chi(E) = (1-\beta)\,\chi_p(E) + \beta\chi_d(E)$ is the total fission spectrum. For a nuclear reactor, it is conceptually possible to find a positive k to make the system steady-state. Therefore, the existence of a positive k with its corresponding eigenfunction also positive everywhere is guaranteed. Equation 2.14 is often called the k-eigenvalue equation, which may have an infinite number of discrete eigenvalues. The corresponding eigenfunctions are referred to as k-modes or λ-modes. The multiplication factor k_{eff} is the maximum positive k-eigenvalue. The reactivity for each k-eigenvalue is then defined accordingly as $\rho_n = (k_n - 1)/k_n$, $n = 0, 1, 2, \cdots$, with ρ_0 as the static reactivity. In the nuclear engineering field, the k-modes are widely used for close-to-critical reactors. However, the shape of the fundamental k-mode does not represent any real neutron flux distribution except when the reactor is critical.

Usually, the k-modes are not orthogonal to each other. Instead, we define the adjoint k-eigenvalue problem as

$$\mathbf{L}^+\phi^+_{m,k} = \frac{1}{k_m}\left[\chi\mathbf{F}\right]^+\phi^+_{m,k}, \tag{2.15}$$

where $\mathbf{L}^+$ and $[\chi\mathbf{F}]^+$ are the adjoint operators of $\mathbf{L}$ and $\chi\mathbf{F}$, respectively. The function $\phi^+_{m,k}$ is called the m^{th}-order adjoint k-mode, which is then biorthogonal to the forward k-modes,

$$\int dV \int_0^\infty dE\phi^+_{m,k}\chi\mathbf{F}\phi_{n,k} = \left\langle \phi^+_{m,k},\ \chi\mathbf{F}\phi_{n,k}\right\rangle_{\mathbf{r},E} = \gamma_n\delta_{mn}, \tag{2.16}$$

with $\gamma_n = \left\langle \phi^+_{n,k},\ \chi\mathbf{F}\phi_{n,k}\right\rangle_{\mathbf{r},E}$.

There is also another type of eigenvalue problem in which the fundamental mode can be real and be measured. It is derived by assuming an exponential solution of the time-dependent diffusion equation,

$$\phi(\mathbf{r}, E, t) = \phi_\alpha(\mathbf{r}, E)e^{\alpha t}, \tag{2.17}$$

$$C(\mathbf{r}, t) = C_\alpha(\mathbf{r})e^{\alpha t}. \tag{2.18}$$

Therefore, after the external neutron source vanishes, the time-dependent neutron equations can be reduced to

$$\left[\frac{\alpha}{v} + \mathbf{L}\right]\phi_\alpha(\mathbf{r}, E) = (1-\beta)\,\chi_p\mathbf{F}\phi_\alpha(\mathbf{r}, E) + \chi_d\lambda C_\alpha(\mathbf{r}), \tag{2.19}$$

$$[\alpha + \lambda]\,C_\alpha = \beta\mathbf{F}\phi_\alpha(\mathbf{r}, E). \tag{2.20}$$

This eigenvalue problem is often referred to as the α-eigenvalue problem. Its eigenfunctions are called α-modes, period modes or natural modes. By solving Equation 2.20 for C_α and substituting it back into Equation 2.19, a nonlinear equation is obtained for the α-eigenvalue problem,

$$\left[\frac{\alpha}{v} + \mathbf{L}\right]\phi_\alpha = \left[(1-\beta)\,\chi_p + \frac{\chi_d\beta\lambda}{\alpha+\lambda}\right]\mathbf{F}\phi_\alpha. \tag{2.21}$$

Then the corresponding precursor density C_α can be calculated as

$$C_\alpha = \frac{\beta}{\lambda+\alpha}\mathbf{F}\phi_\alpha. \tag{2.22}$$

Unlike the k-eigenvalue problem, the α-eigenvalue problem may not be guaranteed to have a dominant discrete eigenvalue, specifically if the reactor size is too small, or if there is an infinite path for neutrons to follow (with zero velocity or an infinite dimension in some direction). However, in a subcritical reactor which is not very far away from critical, a discrete dominant eigenvalue is generally assumed to exist [24]. In real applications, with more assumptions assumed, e.g., the multi-group approximation to the continuous energy variable, the existence of the fundamental α-eigenvalue is more theoretically valid [25].

In Equation 2.21, the value of the neutron velocity v is a very large number, e.g., 2.2×10^5 [cm/s] for thermal neutrons with energy about 0.0253 eV, and the value of the precursor decay constant λ is very small, e.g., the largest decay constant is about 2.7 s^{-1} for the MUSE-4 subcritical reactor. Therefore, the α-eigenfunctions can be divided into two classes: (1) the "prompt" α-eigenfunctions which are obtained by assuming $\alpha \gg \lambda$ so that the second term on the RHS of Equation 2.21 can be ignored:

$$\left[\frac{\alpha}{v} + \mathbf{L}\right] \phi_p = (1-\beta)\,\chi_p \mathbf{F} \phi_p, \tag{2.23}$$

and (2) the "delayed" α-eigenfunctions equation which are obtained by assuming $\alpha \sim \lambda$, so that the "time-absorption" term α/v in Equation 2.21 can be ignored:

$$\mathbf{L}\phi_d = \left[(1-\beta)\,\chi_p + \frac{\chi_d \beta \lambda}{\alpha + \lambda}\right] \mathbf{F} \phi_d. \tag{2.24}$$

The corresponding eigenfunctions ϕ_p and ϕ_d are then called the prompt-neutron α-modes and the delayed-neutron α-modes, respectively.

For a critical system, because the neutron flux ϕ is time invariant, i.e., $\alpha_0 = 0$ in Equation 2.21 and $k = 1$ in Equation 2.14, the fundamental k-mode and the fundamental α-mode satisfy the same equation, and consequently, are identical. For a non-critical system, if the prompt-neutron fission spectrum χ_p and the delayed-neutron fission spectrum χ_d are identical, we could then define

$$\frac{1}{k_n} = \left[(1-\beta) + \frac{\beta\lambda}{\alpha_n + \lambda}\right]. \tag{2.25}$$

Thus, the delayed α-eigenvalue problem in Equation 2.24 is equivalent to the k-eigenvalue problem as defined in Equation 2.14, and the n^{th} delayed α-mode is then similar to the n^{th} k-mode, for $n = 0, 1, \cdots$. However, the shape of the prompt α-modes will always be significantly different from the k-modes, due to the presence of the "time-absorption" term.

Similar to the k-eigenvalue problem, an adjoint problem can also be defined for the α-eigenvalue problem. For the prompt α-modes, the adjoint eigenvalue problem is defined as

$$\left[\frac{\alpha}{v} + \mathbf{L}^{+}\right] \phi_p^{+} = (1-\beta)\left[\chi_p \mathbf{F}\right]^{+} \phi_p^{+}. \tag{2.26}$$

Therefore, the adjoint prompt α-modes are biorthogonal to the direct prompt α-modes,

$$\left\langle \phi_{m,p}^{+},\ v^{-1}\phi_{n,p} \right\rangle_{\mathbf{r},E} = \gamma_n \delta_{mn}. \tag{2.27}$$

The definition of the adjoint α-modes with delayed neutrons included [24] can also be written as

$$\alpha \begin{bmatrix} \frac{1}{v} & 0 \\ 0 & 1 \end{bmatrix} \begin{bmatrix} \phi_\alpha^{+} \\ C_\alpha^{+} \end{bmatrix} = \begin{bmatrix} (1-\beta)\left[\chi_p \mathbf{F} - \mathbf{L}\right]^{+} & \beta \mathbf{F}^{+} \\ \chi_d \lambda & -\lambda \end{bmatrix} \begin{bmatrix} \phi_\alpha^{+} \\ C_\alpha^{+} \end{bmatrix}, \tag{2.28}$$

with the following biorthogonal property holds:

$$\left\langle \phi_{m,\alpha}^{+}, v^{-1}\phi_{n,\alpha} \right\rangle_{\mathbf{r},E} + \left\langle C_{m,\alpha}^{+}, C_{n,\alpha} \right\rangle_{\mathbf{r},E} = \gamma_n \delta_{m,n}. \tag{2.29}$$

2.3 Numerical methods to solve the neutron balance equation

In order to analyze or predict the space- and time-dependent behavior of a nuclear reactor, it is important to solve the time-dependent neutron diffusion or transport equations. However, it is usually not an easy task, mainly because the neutron balance equations are coupled partial-differential integral equations with various continuous variables, e.g., position $\mathbf{r}$ (x, y, z), energy E, direction $\mathbf{\Omega}$ $(\mu,\ \theta)$, and time t for the transport equations.

2.3.1 The direct method

A straightforward way to solve the space- and time-dependent equations is to discretize the spatial variables directly [26]. First of all, we discretize the space variable **r** and energy E by partitioning the reactor into several separate volume elements in multiple energy groups. The neutron diffusion equations are converted to a set of first-order differential equations in each volume element and can be solved by the finite difference method over the time interval $[t_j,\, t_{j+1}]$ for volume element at $\mathbf{r}_i$ and at energy group E_g:

$$\frac{\partial \phi(\mathbf{r}_i, E_g, t)}{\partial t} = \frac{\phi(\mathbf{r}_i, E_g, t_{j+1}) - \phi(\mathbf{r}_i, E_g, t_j)}{t_{j+1} - t_j} \tag{2.30}$$

The direct method is always time-consuming, due to the large number of meshes obtained, and it often takes a significant amount of computational time even for time-independent calculations. In addition, the diffusion equations also form a “stiff” system, due to the presence of the prompt and delayed neutrons. It not only requires an extremely fine time step to accurately describe the prompt-neutron behavior, usually on the order of μs, but also requires the calculation extended into a large number of time steps to represent the delayed-neutron behavior. Therefore, the direct method is normally used only for reference calculations.

2.3.2 The space-time factorization method

The space-time factorization method was developed initially as an alternative to the direct method to solve the space-time neutron diffusion or transport equations with less computational efforts. The basic idea of this method is to factorize the neutron flux into two parts [26]:

$$\phi(\mathbf{r}, E, t) = T(t)\psi(\mathbf{r}, E, t), \tag{2.31}$$

where the amplitude function T depends only on time t and is easy to calculate, while the shape function ψ varies slowly in the time domain. The shape function is often expensive to calculate due to its spatial and energy dependence, but can be obtained accurately with large time-steps. The factorization in Equation 2.31 is not unique. In order to obtain a unique ψ, a normalization is applied:

$$\left\langle \omega, \frac{1}{v}\psi \right\rangle_{\mathbf{r},E} = \int dV \int_0^\infty dE\omega(\mathbf{r},E)v^{-1}\psi(\mathbf{r},E,t) = \gamma, \tag{2.32}$$

where ω is an arbitrary weight function and γ is a constant.

To calculate ψ, we first substitute Equation 2.31 back into the neutron diffusion equation 2.12 to obtain:

$$\frac{1}{v}\frac{\partial \psi}{\partial t} + \mathbf{L}\psi = (1-\beta)\,\chi_p\mathbf{F}\psi + \frac{1}{T}\chi_d\lambda C + \frac{1}{T}Q - \frac{1}{v}\frac{\psi}{T}\frac{dT}{dt}. \tag{2.33}$$

With the amplitude function T determined at t_j, Equation 2.33 may be solved by the backward finite-difference scheme with a large time step $\tau_j = t_j - t_{j-1}$:

$$\begin{aligned} \frac{1}{v}\left[\frac{1}{\tau_j} + \frac{1}{T_j}\frac{dT(t_j)}{dt}\right]\psi_j + \mathbf{L}\psi_j &- \left[(1-\beta)\chi_p\right]\mathbf{F}\psi_j - \frac{1}{T_j}Q_j \\ &= \frac{1}{T_j}\chi_d\lambda C_j + \frac{1}{v}\frac{1}{\tau_j}\psi_{j-1}, \end{aligned} \tag{2.34}$$

in which all the terms on the LHS are evaluated at time t_j, and C_j on the RHS is calculated by

$$\left[\frac{1}{\tau_j} + \lambda\right] C_j = \beta\mathbf{F}\phi_{j-1}. \tag{2.35}$$

On the other hand, with the shape function calculated, the time-dependent neutron balance equations 2.12 and 2.13 can be multiplied by a weight function ω on both sides and integrated over the space and energy domain to yield

$$\frac{dT(t)}{dt} = \frac{\rho(t)-\beta(t)}{\Lambda(t)}T(t) + \lambda c(t) + Q(t), \tag{2.36}$$

$$\frac{dc(t)}{dt} = \frac{\beta(t)}{\Lambda(t)}T(t) - \lambda c(t), \tag{2.37}$$

with kinetics parameters $\rho(t)$, $\beta(t)$, and $\Lambda(t)$ defined in terms of the weight function

ω and the shape function ψ as

$$\Lambda(t) = \frac{\gamma}{\langle \omega, \chi \mathbf{F} \psi \rangle_{\mathbf{r},E}}, \tag{2.38}$$

$$\rho(t) = \frac{\langle \omega, [\chi \mathbf{F} - \mathbf{L}] \, \psi \rangle_{\mathbf{r},E}}{\langle \omega, \chi \mathbf{F} \psi \rangle_{\mathbf{r},E}}, \tag{2.39}$$

$$\beta(t) = \frac{\langle \omega, \beta \chi_d \mathbf{F} \psi \rangle_{\mathbf{r},E}}{\langle \omega, \chi \mathbf{F} \psi \rangle_{\mathbf{r},E}}. \tag{2.40}$$

Here, β is called the effective delayed-neutron fraction and Λ is the neutron mean generation time, which can be interpreted as the average neutron life time in a subcritical reactor [12]. Equation 2.36 and 2.37 are called the quasi-static space-time kinetics equations, and the detailed derivations of them can be also found in Bell's book [24].

In the actual implementation of the space-time factorization method, the shape function ψ is first approximated by a known function in a large time step. This time step is referred to as the shape step. With the approximate ψ, the kinetics parameters β, ρ and Λ are calculated within the shape step. Equation 2.36 and 2.37 are then solved for the amplitude function T with fine time steps, which are called the amplitude steps. With the calculated T, ψ is updated to obtain a new T. The iteration stops when ψ is converged, and the numerical calculation then moves to another shape step. Usually, the shape steps are several times larger than the amplitude steps. The space-time factorization method is an effective method to solve the time-dependent neutron balance equation, and is implemented in many numerical codes.

2.3.3 The modal expansion method

Compared with the space-time factorization method, which calculates the spatial and energy distributions of ϕ and C within each shape step, the modal-expansion method utilizes the pre-computed space- and energy-dependent expansion functions, e.g., the eigenfunctions of the α-eigenvalue problem, to approximate the time-dependent solution:

$$\begin{bmatrix} \phi(\mathbf{r}, E, t) \\ \\ C(\mathbf{r}, t) \end{bmatrix} = \sum_n A_n(t) \begin{bmatrix} \phi_n^\alpha(\mathbf{r}, E) \\ \\ C_n^\alpha(\mathbf{r}) \end{bmatrix}, \tag{2.41}$$

where $A_n(t)$ is the expansion coefficient for the n^{th} α-modes.

In order to obtain the expansion coefficients, the modal expansions are directly substituted back into the neutron balance equations. For notational convenience, we write the equations in a matrix form as

$$\sum_n \frac{dA_n(t)}{dt} \begin{bmatrix} \frac{1}{v} & 0 \\ \\ 0 & \lambda \end{bmatrix} \begin{bmatrix} \phi_{n,\alpha} \\ \\ C_{n,\alpha} \end{bmatrix} = \sum_n A_n(t) \begin{bmatrix} (1-\beta)\chi_p \mathbf{F} - \mathbf{L} & \chi_d \lambda \\ \\ \beta \mathbf{F} & -\lambda \end{bmatrix} \begin{bmatrix} \phi_{n,\alpha} \\ \\ C_{n,\alpha} \end{bmatrix} + Q(\mathbf{r}, E, t). \tag{2.42}$$

If the adjoint function $\left[\phi^+_{m,\alpha} \; C^+_{m,\alpha}\right]$ is applied to both sides of Equation 2.42, and by integrating over the energy and space domain, the expansion coefficient $A_n(t)$ can then be obtained by solving the first-order differential equation:

$$\frac{dA_n(t)}{dt} = -\alpha_n A_n(t) + \frac{1}{\gamma_n} \left\langle \phi^+_{n,\alpha}, Q \right\rangle_{\mathbf{r},E}, \tag{2.43}$$

with $\gamma_n = \left\langle \phi^+_{n,\alpha}, v^{-1}\phi_{n,\alpha} \right\rangle_{\mathbf{r},E} + \left\langle C^+_{n,\alpha}, C_{n,\alpha} \right\rangle_{\mathbf{r},E}$

Nowadays, the modal expansion method is not popular anymore in solving the space-time neutron diffusion equations, mainly because a large number of modes are required in order to obtain a sufficiently accurate solution, especially in regions with large spatial perturbations. However, the modal expansion techniques remains a useful tool when analyzing the spatial effects in pulsed-neutron experiments as demonstrated in the next chapter.

2.4 Space-time kinetics codes

In practical applications, there are several numerical code packages available to solve the time-dependent neutron balance equation. The FX2-TH code and the ERANOS code package are the two main numerical codes we use to simulate the pulsed-neutron experiments in this thesis work.

The FX2-TH code is a 2-dimensional reactor kinetics code with the thermal-hydraulic feedback implemented, and was developed at Argonne National Laboratory (ANL) in the 1970s [27]. It solves the multi-group diffusion equation by discretizing the spatial variables with the mesh-centered finite-difference method. For a k-eigenvalue problem, the SLOR (Successive Line Over-Relaxation) method is used to solve the inner iterations, and the power iteration method is applied to solve the outer iteration. The time-dependent diffusion equations are solved by the space-time factorization method, with the amplitude function and the shape function calculated in tandem.

The ERANOS code package was recently developed by CEA in the framwork of the European collaboration for fast reactor analysis [28]. It includes a lattice physics module ECCO, which utlizes the JEFF data library in the code package and has a resonance self-shielding treatment based on the sub-group method [29]. The ERANOS code package was capable of solving a 3-D, diffusion problem. The VARIANT module can solve the steady-state neutron diffusion equations with the variational nodal method [30]. The KIN3D module, which is based upon the VARIANT module, solves the time-dependent diffusion problem, with either the direct method or the space-time factorization method applied [31].

2.5 The point kinetics equations

In the past, despite that the time-dependent neutron balance equation can accurately describe the kinetics behavior of a nuclear reactor, it is often the point kinetics equations that were widely used in analyzing and predicting the time behavior of nuclear power plants. The point kinetics equations do not treat the reactor as a "point". Instead, it assumes that the time-dependent neutron flux ϕ is separable in the time domain from the energy and space domains. In other words, according to the space-time factorization method we discussed in section 2.3.2, the shape flux ψ is a time-independent function. The time-dependent neutron flux ϕ can then be simply written as

$$\phi(\mathbf{r}, E, t) = T(t)\psi(\mathbf{r}, E). \tag{2.44}$$

Therefore, the kinetics parameters ρ, β and λ are all constants. The quasi-static space-time kinetics equations are then reduced to the point kinetics equations:

$$\frac{dT}{dt}(t) = \frac{\rho - \beta}{\Lambda}T(t) + \lambda c(t) + Q(t), \tag{2.45}$$

$$\frac{dc}{dt}(t) = \frac{\beta}{\Lambda}T(t) - \lambda c(t). \tag{2.46}$$

Typically, for a close-to-critical reactor, the time-dependent shape function is always close to the fundamental k-mode. As a result, the point kinetics equations can describe the reactor dynamics behavior quite well for relatively small perturbations. With the point kinetics approximation, the amplitude function $T(t)$ is then proportional to the reactor power, and the reactivity of the reactor can be obtained easily by a number of methods, e.g., the rod drop method, the α-method, the area-ratio method and the Rossi-α method.

CHAPTER III

The Pulsed-Neutron Experiments

To measure the reactivity of a subcritical reactor, one of the simplest methods is to measure the detector responses subject to a short neutron pulse. Usually, the neutron pulse width ΔT is chosen to be small enough and the neutron pulse period T is required to be large enough such that the prompt neutrons die away quickly between the pulses. Figure 3.1 shows a typical detector response obtained from a pulsed-neutron experiment in a subcritical reactor. It rises to a peak and then dies away quickly, which represents the fast emission of prompt neutrons in the reactor. The peak is due to the contributions of the high-order prompt-neutron modes to the detector readings. After a short period of time, the detector responses decay much more slowly to represent the emission of delayed neutrons in the reactor.

3.1 The area-ratio method

One of the methods which can be used to obtain the reactivity from the pulsed-neutron experiment is the area-ratio method. For this method, the detector responses are often recorded after thousands of neutron pulses are injected into the system so that a constant delayed neutron background is achieved. The pulsed period T is chosen to be relatively small compared with the shortest half life of delayed-neutron precursors. Consequently, the change in the delayed neutron background

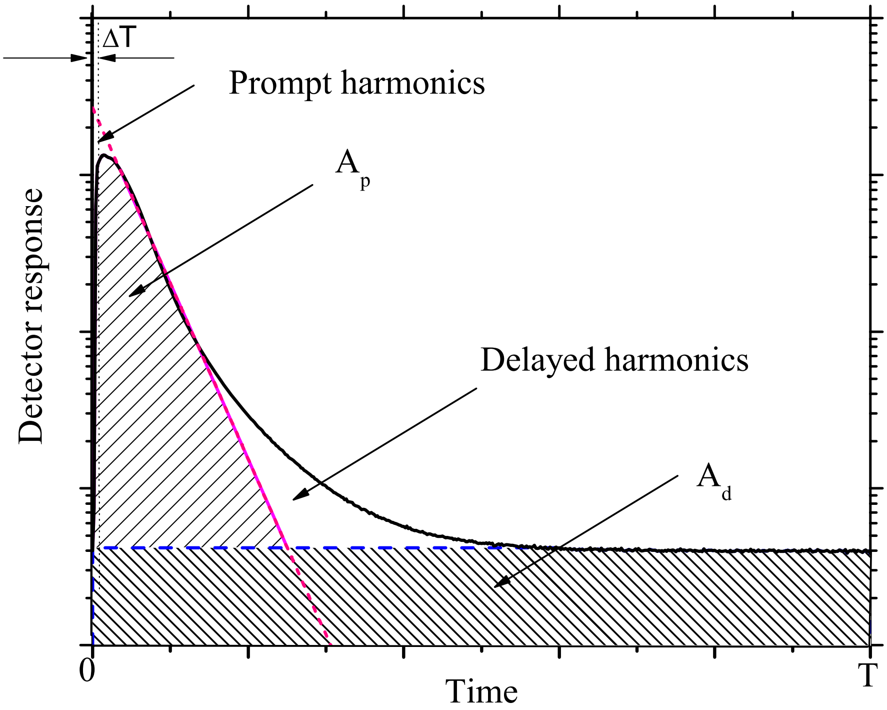

Figure 3.1: Illustration of the simple area-ratio method in a pulsed-neutron experiment.

is negligible within the neutron pulse period. Therefore, in Figure 3.1, the delayed neutron background can be treated as constant.

The area-ratio method is normally referred to as the Sjöstrand method, which states that in a pulsed-neutron experiment, the reactivity in dollars of the subcritical system is given by the negative ratio of the prompt-neutron area A_p and the delayed-neutron area A_d measured by neutron detectors [32],

$$\frac{\rho}{\beta} = -\frac{A_p}{A_t - A_p} = -\frac{A_p}{A_d}. \tag{3.1}$$

In practice, the delayed-neutron area A_d is simply the integration of the delayed neutron background over the pulse period. The prompt-neutron area A_p is obtained by integrating the total detector response subtracted by the delayed-neutron area as shown in Figure 3.1

The area-ratio method in Equation 3.1 is first derived based on the assumption that the subcritical reactor is a point reactor. Namely, the number of neutrons produced in one generation is simply the number of neutrons in its previous generation times the multiplication factor k_{eff} of the subcritical system, and the total number of neutrons generated by the external source S_0 in the reactor can be calculated by summing all the neutrons over successive generations,

$$A_t = \frac{S_0}{1 - k_{eff}} \tag{3.2}$$

Similarly, we also assume that the number of prompt neutrons produced at one generation is equal to $k\,(1-\beta)$ times the source from the previous generation. Therefore, the total number of prompt neutrons A_p produced by the external source is calculated as

$$A_p = \frac{S_0}{1 - k_{eff}(1-\beta)}, \tag{3.3}$$

where β is the delayed-neutron fraction, and is normally treated as a constant [33]. Therefore, the area-ratio of the prompt neutrons and the delayed neutrons can be calculated as

$$\begin{aligned} \frac{A_p}{A_d} &= \frac{S_0/(1 - k_{eff}(1-\beta))}{S_0/(1 - k_{eff}) - S_0/(1 - k_{eff}(1-\beta))} \\ &= -\frac{\rho}{\beta}, \end{aligned} \tag{3.4}$$

which verifies Equation 3.1.

3.1.1 The area-ratio method from the point kinetics equations

The area-ratio method can also be derived from the point kinetics equations. The amplitude function $T(t)$ of the point kinetics equation is partitioned into a prompt part T_p and a delayed part T_d:

$$T_t(t) = T_p(t) + T_d(t), \tag{3.5}$$

where T_t is also the total detector response, and satisfies the point kinetics equations:

$$\frac{dT_t(t)}{dt} = \frac{\rho-\beta}{\Lambda}T_t(t) + \lambda C + Q(t), \tag{3.6}$$

$$\frac{dC(t)}{dt} = \frac{\beta}{\Lambda}P_t(t) - \lambda C(t). \tag{3.7}$$

In an actual pulsed-neutron experiment, because the pulse width ΔT is much smaller than the pulse period T, the external source can be treated as a delta function:

$$Q(t) = Q_0\delta(t). \tag{3.8}$$

The prompt neutrons die out quickly within a very short period of time, and no delayed neutrons contribute to the prompt part T_p. Thus, for T_p, the contributions from the delayed neutrons is ignored and we obtain

$$\frac{dT_p(t)}{dt} = \frac{\rho-\beta}{\Lambda}T_p(t) + Q_0\delta(t), \tag{3.9}$$

with the initial condition $T_p(0^-) = T_p(T^-) = 0$. Furthermore, when the delayed neutron equilibrium status is achieved, the delayed neutron flux reaches a constant level. Therefore, we have another set of initial conditions $T_t(0^-) = T_t(T^-)$ and $C(0^-) = C(T^-)$ for the point kinetics equations.

The prompt neutron area A_p is obtained by integrating the prompt part T_p over the pulse period:

$$A_p = \int_0^T T_p(t)dt = \frac{Q_0\Lambda}{\beta-\rho}. \tag{3.10}$$

Likewise, the total neutron area A_t can be obtained by integrating Equations 3.6 and 3.7 and canceling out the delayed-neutron precursor C to yield:

$$A_t = \int_0^T T_t(t)dt = \frac{Q_0\Lambda}{-\rho}. \tag{3.11}$$

Thus, the area-ratio A_p/A_d can be obtained as

$$\frac{A_p}{A_d} = \frac{A_p}{A_t - A_p} = \frac{\Lambda/(\beta-\rho)}{\Lambda/(\beta-\rho) - \Lambda/\rho} = -\frac{\rho}{\beta}, \tag{3.12}$$

which also verifies Equation 3.1.

In an actual experiment, the external neutron source is always localized in some area, and the shape function of a subcritical reactor never follows the exact shape of the fundamental k-mode. Thus, the point kinetics equations are only approximately applicable in a subcritical reactor. In addition, the neutron detector can only measure the local variation of the neutron flux. Therefore, the area ratio of the prompt neutrons and delayed neutrons is a local value and may be spatially dependent. As illustrated in Figure 3.1, intuitively, the spatial effects are dependent on both the high-order prompt-neutron harmonics and the delayed-neutron harmonics in the reactor.

3.1.2 The extrapolated area-ratio method

In the past, a couple of methods were proposed to reduce or eliminate the spatial effects by eliminating the high-order prompt-neutron harmonics. One such example is the extrapolated area-ratio method [18]. In this method, the reactivity in dollars equals the negative ratio of the extrapolated prompt-neutron area A_p^* to the delayed-neutron area A_d:

$$\left(\frac{\rho}{\beta}\right)^{GO} = -\left[\frac{A_p^*}{A_d}\right], \tag{3.13}$$

and the reactivity is often referred to as Gozani's reactivity.

The prompt-neutron area A_p^* is obtained by fitting the detector response with an exponential function, and extrapolating the prompt-neutron decay back to the beginning of the neutron pulse as shown in Figure 3.2. Both the simple area-ratio method and the extrapolated method were used to obtain reactivities in the past. However, very distinct spatial effects were reported for the two methods in the pulsed-neutron experiments [34, 19]. In this thesis, we will analyze the spatial effects of both methods explicitly, and derive different spatial correction factors to help understand the differences between these two methods.

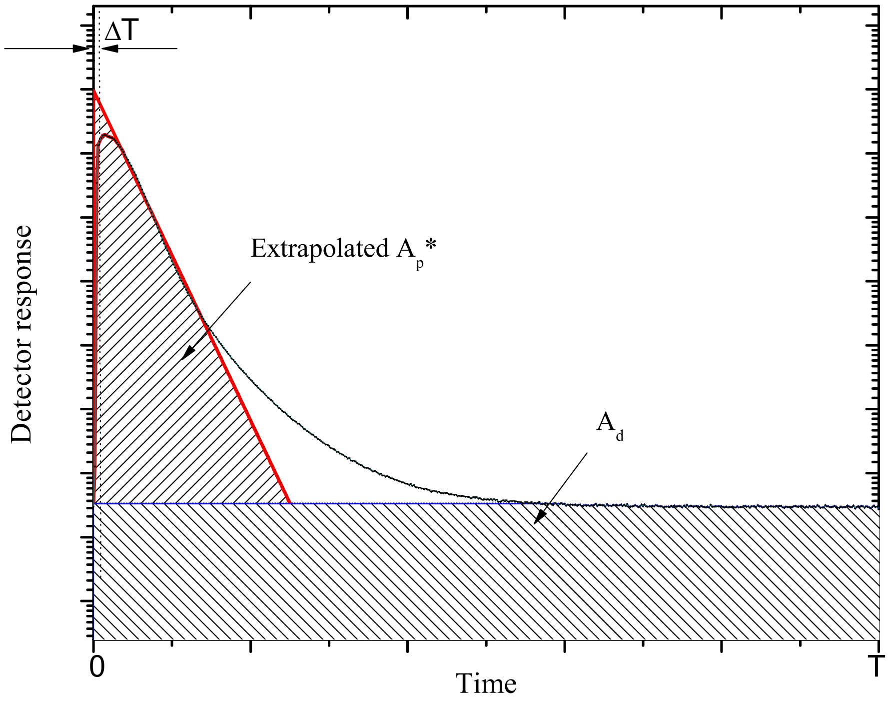

Figure 3.2: Illustration of the extrapolated area-ratio method in a pulsed-neutron experiment.

3.2 The α-method

The α-method is another approach to obtain the reactivity of a subcritical reactor from pulsed-neutron experiments. Unlike the area-ratio method, the detector responses in the α-method can be recorded after a single pulse. This method can also be directly derived from the point kinetics equations. For convenience, we rewrite Equation 3.9 for prompt neutrons only:

$$\frac{dT_p}{dt} = \frac{\rho - \beta}{\Lambda} T_p(t) + Q(t). \tag{3.14}$$

Its solution follows an exponential decay after the external neutron source is turned off with a decay constant equal to

$$\alpha = \frac{\rho - \beta}{\Lambda}, \tag{3.15}$$

which can be measured directly from the experimental data by exponential fitting. If the kinetics parameters β and Λ of the system are determined separately, the reactivity ρ of the subcritical reactor can then be obtained easily as

$$\rho = \beta + \alpha\Lambda. \tag{3.16}$$

CHAPTER IV

Spatial Effects in the Pulsed Neutron Experiments

As shown in Chapter III, both the area-ratio method and the α-method can be derived from the point kinetics equations, by separating the prompt neutron part T_p from the total neutron detector response T_t. For a subcritical reactor far from critical, the point kinetics equations are only approximately applicable. Therefore, to explore the spatial effects in the two methods, we start with the time-dependent neutron balance equations:

$$\begin{aligned} \frac{1}{v}\frac{\partial\phi(\mathbf{r},E,t)}{\partial t} + \mathbf{L}(\mathbf{r},E)\phi(\mathbf{r},E,t) &= (1-\beta)\,\chi_p(E)\mathbf{F}(\mathbf{r},E)\phi(\mathbf{r},E,t) \\ &+ \chi_d(E)\lambda C(\mathbf{r},t) + Q(\mathbf{r},E,t), \qquad (4.1) \\ \frac{\partial C(\mathbf{r},t)}{\partial t} + \lambda C(\mathbf{r},t) &= \beta\mathbf{F}(\mathbf{r},E)\phi(\mathbf{r},E,t), \qquad (4.2) \end{aligned}$$

with the corresponding initial conditions $\phi_t(\mathbf{r},E,0^-) = \phi_t(\mathbf{r},E,T^-)$ and $C(\mathbf{r},0^-) = C(\mathbf{r},T^-)$ when the delayed-neutron equilibrium status is reached. Similarly, we also divide the total time-dependent neutron flux ϕ_t into a prompt-neutron part ϕ_p and a delayed-neutron part ϕ_d:

$$\phi_t(\mathbf{r},E,t) = \phi_p(\mathbf{r},E,t) + \phi_d(\mathbf{r},E,t). \qquad (4.3)$$

Because the prompt neutron flux dies out very quickly within a short period of time, the time-dependent prompt-neutron flux then satisfies

$$\begin{aligned}\frac{1}{v}\frac{\partial\phi_p(\mathbf{r},E,t)}{\partial t}+\mathbf{L}(\mathbf{r},E)\phi_p(\mathbf{r},E,t) &= (1-\beta)\,\chi_p(E)\mathbf{F}(\mathbf{r},E)\phi_p(\mathbf{r},E,t)\\ &+ Q(\mathbf{r},E,t),\end{aligned}\tag{4.4}$$

with initial conditions $\phi_p(\mathbf{r},E,0^-)=\phi_p(\mathbf{r},E,T^-)=0$. Therefore, the neutron areas A_p and A_d can be obtained by integrating the detector responses over the pulse period T:

$$A_p(\mathbf{r}_D) = \int_0^T \langle\Sigma_d(\mathbf{r}_D,E),\phi_p(\mathbf{r}_D,E,t)\rangle_E\,dt,\tag{4.5}$$

$$A_d(\mathbf{r}_D) = \int_0^T \langle\Sigma_d(\mathbf{r}_D,E),\phi_d(\mathbf{r}_D,E,t)\rangle_E\,dt,\tag{4.6}$$

where $\Sigma_d(\mathbf{r}_D,E)$ is the detector response function at energy E.

4.1 The area-ratio method

4.1.1 Bell's spatial correction factor

To explore the spatial effects in the area-ratio method, we want to relate the static reactivity ρ with the measured A_p and A_d. First, we integrate the neutron balance equations 4.1 through 4.4 over the pulse period T and obtain

$$\mathbf{L}\int_0^T \phi_p dt = (1-\beta)\,\chi_p\mathbf{F}\int_0^T\phi_p dt+\int_0^T Q dt,\tag{4.7}$$

$$\mathbf{L}\int_0^T \phi_t dt = \chi\mathbf{F}\int_0^T\phi_t dt+\int_0^T Q dt.\tag{4.8}$$

If we define the time-integrated prompt neutron flux as $\hat{\phi}_p(\mathbf{r},E)=\int_0^T\phi_p(\mathbf{r},E,t)dt$, and the time-integrated total neutron flux as $\hat{\phi}_t(\mathbf{r},E)=\int_0^T\phi_t(\mathbf{r},E,t)dt$, $\hat{\phi}_p$ and $\hat{\phi}_t$ are then the solutions of the static diffusion or transport equations:

$$\mathbf{L}\hat{\phi}_p = (1-\beta)\,\chi_p\mathbf{F}\hat{\phi}_p+\int_0^T Q dt,\tag{4.9}$$

$$\mathbf{L}\hat{\phi}_t = \chi\mathbf{F}\hat{\phi}_t+\int_0^T Q dt.\tag{4.10}$$

The prompt neutron area A_p and the total neutron area A_t can then be directly calculated as

$$A_p = \left\langle \Sigma_d, \int_0^T \phi_p dt \right\rangle_E = \left\langle \Sigma_d, \hat{\phi}_p \right\rangle_E, \tag{4.11}$$

$$A_t = \left\langle \Sigma_d, \int_0^T \phi_t dt \right\rangle_E = \left\langle \Sigma_d, \hat{\phi}_t \right\rangle_E. \tag{4.12}$$

The delayed neutron area A_d can be obtained as

$$A_d = \left\langle \Sigma_d, \int_0^T \phi_d dt \right\rangle_E = \left\langle \Sigma_d, \hat{\phi}_d \right\rangle_E = \left\langle \Sigma_d, \hat{\phi}_t - \hat{\phi}_p \right\rangle_E. \tag{4.13}$$

Remarkably, this observation leads to a direct way of correcting the spatial effects in the area-ratio method. Specifically, we start with the following identity:

$$\frac{\rho}{\beta} = -\left[\frac{A_p}{A_d}\right] \times \left[\frac{A_d}{A_p} \cdot \frac{-\rho}{\beta}\right]. \tag{4.14}$$

Therefore, we can define a spatial correction factor $f(\mathbf{r}_D)$ as

$$f(\mathbf{r}_D) = -\left[\frac{A_d(\mathbf{r}_D)}{A_p(\mathbf{r}_D)}\right] \cdot \left[\frac{\rho}{\beta}\right]. \tag{4.15}$$

If A_p, A_d, ρ and β could be obtained from numerical simulations, the spatial correction factor f can then be calculated easily. Due to the cross section data uncertainties, the geometry errors, etc., the neutron areas calculated through Equations 4.11 and 4.12 are not exactly the same as in the actual experiment. Nevertheless, with a sufficiently accurate numerical model, f can account for the spatial effects in the area-ratio method adequately, because any systematic errors in the numerical model will be reduced in calculating the ratio by Equation 4.15. The reactivity of the reactor can then be determined by

$$\frac{\rho}{\beta} = -\left[\frac{A_p(\mathbf{r}_D)}{A_d(\mathbf{r}_D)}\right]^{exp} \cdot f(\mathbf{r}_D)^{cal}. \tag{4.16}$$

It was Bell [24] who first suggested using Equations 4.11 and 4.13 to calculate the prompt- and delayed-neutron areas numerically. Therefore, we also call the spatial correction factor f defined in Equation 4.15 as Bell's spatial correction factor. Equations 4.9 through 4.12 were used to reproduce some of the MUSE-4 experimental data [16] successfully. Bell's spatial correction factor f is easy to calculate, because it only requires to solve two steady-state fixed source problems for the time-integrated flux $\hat{\phi}_p$ and $\hat{\phi}_t$, and to calculate two constants ρ and β. In order to eliminate the spatial effects, the numerical model should be as accurate as possible. The Monte Carlo method is capable of accurately modeling the reactor geometry and neutron physics in the reactor.

The limitation of this spatial correction factor is that it cannot give physical explanation of the spatial variations observed in the experiments. Specifically, it cannot predict how the experimental results will be spatially dependent without direct numerical simulations. With this spatial correction factor, it is also unclear how the high-order harmonics affect the experimental result in the area-ratio method, and whether the high-order harmonics can be ignored in calculating the spatial correction factors. Therefore, to understand the role of the high-order harmonics in the area-ratio method, the modal expansion techniques is used in the next to physically explain the spatial dependence in the area-ratio method.

4.1.2 The modal expansion method to the area-ratio method

In order to study the spatial effects in the area-ratio method, instead of integrating the time-dependent neutron balance equations 4.1 through 4.4 directly, we derive the area-ratio method starting with the time-dependent neutron balance equations. First, the modal expansion technique is applied to the prompt-neutron flux with the prompt α-modes as the expansion functions:

$$\phi_p(\mathbf{r}, E, t) \quad = \quad \sum_m^M A_m(t)\phi_{m,p}(\mathbf{r}, E), \tag{4.17}$$

where $A_m(t)$ is the expansion coefficient for the m^{th} mode. Usually, in pulsed-neutron experiments, the external neutron source varies in the time domain, and it can be represented as

$$Q(\mathbf{r}, E, t) = Q_0(\mathbf{r}, E)\delta Q(t). \tag{4.18}$$

Therefore, by substituting Equations 4.17 and 4.18 back into Equation 4.4, we obtain

$$\sum_m^M \frac{\phi_{m,p}}{v}\frac{dA_m(t)}{dt} = \sum_m^M \left[(1-\beta)\chi_p\mathbf{F} - \mathbf{L}\right]\phi_{m,p}A_m(t) + Q_0\delta Q. \tag{4.19}$$

If we multiply both sides of Equation 4.19 by the adjoint prompt α-mode $\phi^+_{k,p}$ and integrate it over the space and energy domain, with Equations 2.26 and 2.27, the coefficient $A_m(t)$ is then determined by a first-order differential equation

$$\frac{dA_m(t)}{dt} = \alpha_m A_m(t) + \frac{\left\langle \phi^+_{m,p}, Q_0\right\rangle_{\mathbf{r},E}}{\left\langle \phi^+_{m,p}, 1/v\phi_{m,p}\right\rangle_{\mathbf{r},E}}\delta Q(t), \tag{4.20}$$

and its solution can be written as

$$A_m(t) \;=\; \frac{\left\langle \phi^+_{m,p}, Q_0\right\rangle_{\mathbf{r},E}}{\left\langle \phi^+_{m,p}, 1/v\phi_{m,p}\right\rangle_{\mathbf{r},E}} e^{\alpha_m t}\int_0^t \delta Q(t')e^{-\alpha_m t'}dt'. \tag{4.21}$$

Because the pulsed width ΔT is very small compared with the pulse period T, the external source could then be treated as a δ-function. The total prompt neutron area A_p can then be also calculated as

$$A_p = \int_0^T \left\langle \Sigma_d(\mathbf{r}_D), \phi_p(\mathbf{r}_D, E, t)\right\rangle_E dt = \sum_m^M \frac{A_m(0)}{-\alpha_m}\left\langle \Sigma_d, \phi_{m,p}\right\rangle_E, \tag{4.22}$$

where

$$A_m(0) = \frac{\left\langle \phi^+_{m,p}, Q_0\right\rangle_{\mathbf{r},E}}{\left\langle \phi^+_{m,p}, 1/v\phi_{m,p}\right\rangle_{\mathbf{r},E}}. \tag{4.23}$$

In a nuclear reactor, the delayed-neutron precursors are often immobile, and the delayed-neutron α-modes can be approximated by the k-modes. Therefore, we expand the time-integrated delayed-neutron flux directly with the k-modes as the expansion functions:

$$\hat{\phi}_d(\mathbf{r},E) \;=\; \sum_n^N B_n \phi_{n,k}(\mathbf{r},E), \tag{4.24}$$

where B_n is the expansion coefficient of the n^{th} term. In order to find the expansion coefficients B_n, we integrate Equations 4.1 through 4.4 over the pulse period $[0,T]$. By eliminating the precursor density functions C, the time-integrated prompt neutron flux and the time-integrated delayed-neutron flux hold the relationship:

$$[\mathbf{L}-\chi\mathbf{F}]\,\hat{\phi}_d = \chi_d \beta \mathbf{F} \hat{\phi}_p. \tag{4.25}$$

Then, if the modal expansions in Equations 4.17 and 4.24 are substituted back into the above relationship, we obtain

$$\sum_n^N B_n\,[\mathbf{L}-\chi\mathbf{F}]\,\phi_{n,k} = \sum_n^N B_n \left[\frac{1}{k_n}-1\right] \chi\mathbf{F}\phi_{n,k} = \sum_m^M \chi_d \beta \frac{A_m(0)}{-\alpha_m}\mathbf{F}\phi_{m,p}. \tag{4.26}$$

By multiplying both sides with the adjoint k-mode $\phi^+_{n,k}$ and integrating over the pulse period $[0,T]$, the expansion coefficient B_n can then be obtained as

$$B_n \rho_n = -\frac{\sum_m^M \left\langle \phi^+_{n,k}, \chi_d \beta \frac{A_m(0)}{-\alpha_m} \mathbf{F}\phi_{m,p} \right\rangle_{\mathbf{r},E}}{\left\langle \phi^+_{n,k}, \chi\mathbf{F}\phi_{n,k}\right\rangle_{\mathbf{r},E}}, \quad n = 0,1,2,\cdots, \tag{4.27}$$

where $\rho_n = (k_n - 1)/k_n$, and ρ_0 is the static reactivity ρ. Consequently, the delayed-neutron area can be obtained by summing over all modal terms as

$$\begin{aligned} A_d &= \sum_n^N \langle \Sigma_d, B_n \phi_{n,k} \rangle_E \\ &= B_0 \langle \Sigma_d, \phi_{0,k} \rangle_E \left[1 + \sum_{n=1}^N \frac{B_n \langle \Sigma_d, \phi_{n,k}\rangle_E}{B_0 \langle \Sigma_d, \phi_{0,k}\rangle_E} \right]. \end{aligned} \tag{4.28}$$

To relate the static reactivity ρ with the area-ratio A_p/A_d, we divide Equation 4.28 by Equation 4.22 on both sides to solve for B_0:

$$\frac{1}{B_0} \;=\; \left[\frac{A_p}{A_d}\right] \left[\frac{\langle \Sigma_d, \phi_{0,k}\rangle_E}{\sum_m^M \frac{A_m(0)}{-\alpha_m} \langle \Sigma_d, \phi_{m,p}\rangle_E} \right] \left[1 + \sum_{n=1}^N \frac{B_n \langle \Sigma_d, \phi_{n,k}\rangle_E}{B_0 \langle \Sigma_d, \phi_{0,k}\rangle_E} \right]. \tag{4.29}$$

The B_0 term can also be evaluated from Equation 4.27 with $n = 0$. Thus, by eliminating B_0 in Equation 4.29, we obtain

$$\rho_0 = -\left[\frac{A_p}{A_d}\right]\left[\frac{\displaystyle\sum_m^M \frac{A_m(0)}{\alpha_m}\frac{\left\langle \phi_{0,k}^+, \chi_d \beta \mathbf{F} \phi_{m,p}\right\rangle_{\mathbf{r},E}}{\left\langle \phi_{0,k}^+, \chi \mathbf{F} \phi_{0,k}\right\rangle_{\mathbf{r},E}}}{\displaystyle\sum_m^M \frac{A_m(0)}{\alpha_m}\frac{\left\langle \Sigma_d, \phi_{m,p}\right\rangle_E}{\left\langle \Sigma_d, \phi_{0,k}\right\rangle_E}}\right]\left[1+\sum_{n=1}^N \frac{B_n \left\langle \Sigma_d, \phi_{n,k}\right\rangle_E}{B_0 \left\langle \Sigma_d, \phi_{0,k}\right\rangle_E}\right] \tag{4.30}$$

In addition, if we define β_{eff} similar to Equation 2.40:

$$\beta_{eff} = \frac{\left\langle \phi_{0,k}^+, \chi_d \beta \mathbf{F} \phi_{0,k}\right\rangle_{\mathbf{r},E}}{\left\langle \phi_{0,k}^+, \chi \mathbf{F} \phi_{0,k}\right\rangle_{\mathbf{r},E}}, \tag{4.31}$$

Equation 4.30 can be rewritten as

$$\frac{\rho_0}{\beta_{eff}} = -\left[\frac{A_p(\mathbf{r}_D)}{A_d(\mathbf{r}_D)}\right] \cdot f_p(\mathbf{r}_D) \cdot f_d(\mathbf{r}_D), \tag{4.32}$$

where f_p and f_d are the spatial correction factors to the area-ratio method, corresponding to the prompt-neutron harmonics and the delayed-neutron harmonics, respectively,

$$f_p = \left[\frac{\displaystyle\sum_m^M \frac{A_m(0)}{\alpha_m}\frac{\left\langle \phi_{0,k}^+, \chi_d \beta \mathbf{F} \phi_{m,p}\right\rangle_{\mathbf{r},E}}{\left\langle \phi_{0,k}^+, \chi_d \beta \mathbf{F} \phi_{0,k}\right\rangle_{\mathbf{r},E}}}{\displaystyle\sum_m^M \frac{A_m(0)}{\alpha_m}\frac{\left\langle \Sigma_d, \phi_{m,p}\right\rangle_E}{\left\langle \Sigma_d, \phi_{0,k}\right\rangle_E}}\right], \tag{4.33}$$

$$f_d = \left[1+\sum_{n=1}^N \frac{B_n \left\langle \Sigma_d, \phi_{n,k}\right\rangle_E}{B_0 \left\langle \Sigma_d, \phi_{0,k}\right\rangle_E}\right]. \tag{4.34}$$

As shown in Equation 4.33, the prompt-neutron harmonics affect the area-ratio results in a complicated manner. If we only consider the spatial effects induced by the fundamental prompt mode, i.e., $m = 0$, in Equation 4.33, the correction factor f_p is then reduced to

$$f_p^0(\mathbf{r}_D) = \left[\frac{\left\langle \phi_{0,k}^+, \chi_d \beta \mathbf{F} \phi_{0,p}\right\rangle_{\mathbf{r},E}}{\left\langle \phi_{0,k}^+, \chi_d \beta \mathbf{F} \phi_{0,k}\right\rangle_{\mathbf{r},E}} \cdot \frac{\left\langle \Sigma_d, \phi_{0,k}\right\rangle_E}{\left\langle \Sigma_d \phi_{0,p}\right\rangle_E}\right], \tag{4.35}$$

which is the traditional "kinetics distortion" factor originally suggested by Gozani [35]. However, our derivation also indicates that the spatial correction factor for the area-ratio method is not solely determined by the kinetics distortion factor, but also dependent on the difference between the high-order prompt α-modes and the fundamental k-mode. The spatial distributions of the high-order prompt α-modes always deviate substantially from that of the fundamental k-mode. Therefore, f_p might be significantly different from f_p^0.

In addition, the summation of the infinite series in the denominator and numerator of Equation 4.33 is nothing but a modal expansion of the time-integrated prompt-neutron flux $\hat{\phi}_p$

$$\hat{\phi}_p = \int_0^T \phi_p(\mathbf{r}, E, t)dt = \sum_m^M \frac{A_m(0)}{-\alpha_m}\phi_{m,p}. \tag{4.36}$$

Thus, with all the high-order prompt α-modes included, the spatial correction factor f_p eventually converges to a prompt correction factor f_p^∞:

$$f_p^\infty(\mathbf{r}_D) = \left[\frac{\left\langle \phi_{0,k}^+, \chi_d \beta \mathbf{F} \hat{\phi}_p \right\rangle_{\mathbf{r},E}}{\left\langle \phi_{0,k}^+, \chi_d \beta \mathbf{F} \phi_{0,k} \right\rangle_{\mathbf{r},E}} \cdot \frac{\left\langle \Sigma_d, \phi_{0,k} \right\rangle_E}{\left\langle \Sigma_d, \hat{\phi}_p \right\rangle_E}\right], \tag{4.37}$$

which indicates that the spatial variations of the area-ratio method induced by the prompt-neutron harmonics are determined by the difference between the time-integrated prompt-neutron flux $\hat{\phi}_p$ and the fundamental k-mode $\phi_{0,k}$. If $\hat{\phi}_p$ and $\phi_{0,k}$ are properly normalized so that

$$\left\langle \phi_{0,k}^+, \chi_d \beta \mathbf{F} \hat{\phi}^p \right\rangle_{\mathbf{r},E} = \left\langle \phi_{0,k}^+, \chi_d \beta \mathbf{F} \phi_{0,k} \right\rangle_{\mathbf{r},E}, \tag{4.38}$$

f_p^∞ is simply the ratio of $\phi_{0,k}$ and ϕ_p at detector position $\mathbf{r}_D$, i.e.,

$$f_p^\infty(\mathbf{r}_D) = \frac{\left\langle \Sigma_d, \phi_{0,k} \right\rangle_E}{\left\langle \Sigma_d, \hat{\phi}_p \right\rangle_E}. \tag{4.39}$$

Similar to f_p, with all the delayed α-modes included, the spatial correction factor f_d is determined by the differences between the high-order k-modes and the fundamental k-mode, and it converges to a delayed correction factor defined by

$$f_d^{\infty}(\mathbf{r}_D) = \left[\frac{\left\langle \Sigma_d, \int_0^T \phi_d dt \right\rangle_E}{B_0 \left\langle \Sigma_d, \phi_{0,k} \right\rangle_E} \right] = \left[\frac{\left\langle \Sigma_d, \hat{\phi}_d \right\rangle_E}{B_0 \left\langle \Sigma_d, \phi_{0,k} \right\rangle_E} \right]. \tag{4.40}$$

Compared with the spatial correction factor f obtained from Bell's method in Equation 4.15, f_p^{∞} is easier to calculate because it does not require the calculation of β_{eff}. In addition, with the spatial correction factor f_p^{∞}, the spatial dependence of the area-ratio method can be simply determined by the difference of the two flux distributions. Thus, the correction factor f_p^{∞} we derived can give physically intuitive explanation on the spatial dependence in the area-ratio method. Specifically, we will compare the two flux distributions in Section 6.1.2 to analyze the spatial effects in the area-ratio method. We will also use it to explain the spatial dependence observed in the MUSE-4 pulsed-neutron experiment as shown in Section 7.2.3. Because the spatial correction factors f_p and f_d are always obtained through Equations 4.37 and 4.40, for notational simplicity, we will refer to f_p^{∞} and f_d^{∞} as f_p and f_d, respectively, for the rest of the thesis.

Finally, the total spatial corrections can be calculated as

$$f^m = f_p \times f_d. \tag{4.41}$$

With Equations 4.37, 4.40, and 4.27, the prompt correction factor f_p together with delayed correction factor f_d returns to Bell's correction factor f:

$$\begin{aligned}
f^m &= \left[\frac{\left\langle \phi_{0,k}^{+}, \chi_d \beta \mathbf{F} \hat{\phi}_p \right\rangle_{\mathbf{r},E}}{\left\langle \phi_{0,k}^{+}, \chi_d \beta \mathbf{F} \phi_{0,k} \right\rangle_{\mathbf{r},E}} \cdot \frac{\left\langle \Sigma_d, \phi_{0,k} \right\rangle_E}{\left\langle \Sigma_d, \hat{\phi}_p \right\rangle_E}\right] \left[\frac{\left\langle \Sigma_d, \hat{\phi}_d \right\rangle_E}{B_0 \left\langle \Sigma_d, \phi_{0,k} \right\rangle_E}\right] \\
&= \left[\frac{\left\langle \phi_{0,k}^{+}, \chi_d \beta \mathbf{F} \hat{\phi}_p \right\rangle_{\mathbf{r},E}}{\left\langle \phi_{0,k}^{+}, \chi_d \beta \mathbf{F} \phi_{0,k} \right\rangle_{\mathbf{r},E}} \cdot \frac{\left\langle \Sigma_d, \hat{\phi}_d \right\rangle_E}{\left\langle \Sigma_d, \hat{\phi}_p \right\rangle_E}\right] \frac{1}{B_0} \\
&= -\frac{\left\langle \Sigma_d, \hat{\phi}_d \right\rangle_E}{\left\langle \Sigma_d, \hat{\phi}_p \right\rangle_E} \cdot \frac{\rho_0 \left\langle \phi_{0,k}^{+}, \chi \mathbf{F} \phi_{0,k} \right\rangle_{\mathbf{r},E}}{\left\langle \phi_{0,k}^{+}, \chi_d \beta \mathbf{F} \phi_{0,k} \right\rangle_{\mathbf{r},E}} \\
&= -\frac{A_d}{A_p} \cdot \frac{\rho_0}{\beta} = f. \qquad (4.42)
\end{aligned}$$

Thus, the modal analysis we presented here stands as a way to explore the role of high-order harmonics played in the area-ratio method, and how the spatial effects from the prompt-neutron harmonics and the delayed-neutron harmonics could be separated. The spatial correction factors for the area-ratio method are derived rigorously. Equations 4.39 and 4.40 also indicate that for a subcritical reactor, the spatial correction factor f_p and f_d can not be 1.0 everywhere in the reactor because of the different spatial distributions of the time-integrated prompt flux $\hat{\phi}_p$ and the fundamental k-mode $\phi_{0,k}$. Thus, our modal analysis also shows that for subcritical reactors, the area-ratio method is always spatially dependent.

4.1.3 The modal expansion method to the extrapolated area-ratio method

In the past, a modal analysis was performed by Preskitt, et al. [22] to obtain the space-time corrections for the extrapolated area-ratio method. However, their derivations could not identify the spatial effects induced by the prompt-neutron harmonics and delayed-neutron harmonics separately. With similar steps for the area-ratio method, we may also obtain both f_p and f_d for the extrapolated area-ratio method.

In particular, in the extrapolated area-ratio method, the extrapolated prompt neutron area A_p^* is the fundamental term of the prompt neutron area A_p and can be obtained from Equation 4.22:

$$A_p^*(\mathbf{r}_D) = \frac{A_0(0)}{-\alpha_0}\left\langle \Sigma_d, \phi_{0,p} \right\rangle_E \tag{4.43}$$

Thus, to study the spatial effects in the extrapolated area-ratio method, we relate the reactivity ρ with the area-ratio A_p^*/A_d. With similar derivations to the area-ratio method, if we divide Equation 4.28 by Equation 4.43 on both sides, the expansion coefficient B_0 is obtained as

$$\frac{1}{B_0} = \left[\frac{A_p^*}{A_d}\right]\left[\frac{\left\langle \Sigma_d, \phi_{0,k} \right\rangle_E}{\frac{A_0(0)}{-\alpha_0}\left\langle \Sigma_d, \phi_{0,p} \right\rangle_E}\right]\left[1 + \sum_{n=1}^{N} \frac{B_n \left\langle \Sigma_d, \phi_{n,k} \right\rangle_E}{B_0 \left\langle \Sigma_d, \phi_{0,k} \right\rangle_E}\right]. \tag{4.44}$$

Then, by substituting Equation 4.44 back into Equation 4.27, we obtain the reactivity in dollars:

$$\frac{\rho_0}{\beta_{eff}} = -\left[\frac{A_p^*(r_D)}{A_d(r_D)}\right] \cdot f_{p,e} \cdot f_{d,e} \tag{4.45}$$

where the spatial correction factors $f_{p,e}$ and $f_{d,e}$ are defined as

$$f_{p,e} = \left[\frac{-\alpha_0 \frac{\left\langle \phi_{0,k}^+, \chi_d \beta \mathbf{F} \hat{\phi}_p \right\rangle_{\mathbf{r},E}}{\left\langle \phi_{0,k}^+, \chi_d \beta \mathbf{F} \phi_{0,k} \right\rangle_{\mathbf{r},E}}}{A_0(0) \frac{\left\langle \Sigma_d, \phi_{0,p} \right\rangle_E}{\left\langle \Sigma_d, \phi_{0,k} \right\rangle_E}}\right], \tag{4.46}$$

$$f_{d,e} = \left[1 + \sum_{n=1}^{N} \frac{B_n \left\langle \Sigma_d, \phi_{n,k} \right\rangle_E}{B_0 \left\langle \Sigma_d, \phi_{0,k} \right\rangle_E}\right]. \tag{4.47}$$

Like from the area-ratio method, the reactivity obtained from the extrapolated area-ratio method will also be contaminated by the high-order delayed-neutron harmonics. Moreover, the spatial effects induced by the prompt-neutron harmonics are solely determined by the kinetics distortion factor, which is significantly different from the simple area-ratio method. Usually, the kinetics distortion is manifest in the region with low absorption cross sections, i.e., the reflector and shield regions. Thus, from our modal analysis, we can conclude that the reactivity derived from the extrapolated area-ratio method is expected to exhibit strong spatial dependence in the regions where kinetics distortion is significant. In addition, our modal analysis also confirms that the spatial dependence in the area-ratio method is significantly different from that in the extrapolated area-ratio method, due to the presence of the high-order prompt-neutron harmonics in the subcritical reactor.

4.2 The α-method

4.2.1 α-method with the space-time kinetics

Unlike the area-ratio method, the α-method is only related to the prompt neutron decay in a subcritical reactor. Therefore, to study the spatial effects in the α-method, we first derive a formula similar to Equation 3.16 when the point kinetics approximation is not valid, requiring the use of Equation 4.4 for the prompt-neutron flux only.

For convenience, we rewrite Equation 4.4 as

$$\frac{1}{v}\frac{\partial \phi_p}{\partial t} + \mathbf{L}\phi_p \quad = \quad (1-\beta)\,\chi_p \mathbf{F}\phi_p + Q_0 \delta Q(t). \tag{4.48}$$

The modal expansion of Equation 4.17 is also utilized to expand the prompt-neutron flux ϕ_p, with the expansion coefficient $A_m(t)$ obtained in Equation 4.21. Then, the detector response measured at the detector position $\mathbf{r}_D$ in the pulsed-neutron experiment is

$$R(\mathbf{r}_D, t) = \langle \Sigma_d(\mathbf{r}_D, E), \phi_p(\mathbf{r}, E, t)\rangle_E = \sum_m^M A_m(t)\,\langle \Sigma_d, \phi_{m,p}\rangle_E\,. \tag{4.49}$$

For the α-method, we are interested in the detector responses in the prompt-neutron decay region after the neutron pulsed is turned off. Thus, for $t > \Delta T$, the expansion coefficient $A_m(t)$ in Equation 4.21 can be also be rewritten as

$$A_m(t) = A_m(\Delta T)e^{\alpha_m(t-\Delta T)}, \tag{4.50}$$

where $A_m(\Delta T)$ is the coefficient $A_m(t)$ evaluated at the time point $t = \Delta T$ when the neutron pulse is turned off, and α_m is the m^{th} eigenvalue of the prompt α-eigenvalue as defined in Equation 2.23. Thus, the detector response can be expressed as the summation of multiple exponential terms

$$R(\mathbf{r}_D, t) = \sum_{m}^{M} A_m(\Delta T) \left\langle \Sigma_d, \phi_{m,p} \right\rangle_E e^{\alpha_m(t-\Delta T)}, \tag{4.51}$$

and the slowest decay constant α_0 can be retrieved from the measured detector responses R by the standard exponential fitting technique after all the high-order prompt-neutron harmonics decay away.

With the measured decay constant α_0 from the pulsed-neutron experiment, in order to obtain the reactivity ρ of the reactor, we first rewrite the adjoint k-eigenvalue problem as

$$\mathbf{L}^+ \phi_{0,k}^+ \quad = \quad (1-\rho) \left[\chi \mathbf{F}\right]^+ \phi_{0,k}^+. \tag{4.52}$$

If we multiply both sides of the above equation by $\phi_{0,p}$, and integrate over the space and energy domains, ρ can be obtained as

$$\rho = \frac{\left\langle \left[\chi \mathbf{F} - \mathbf{L}\right]^+ \phi_{0,k}^+, \phi_{0,p} \right\rangle_{\mathbf{r},E}}{\left\langle \left[\chi \mathbf{F}\right]^+ \phi_{0,k}^+, \phi_{0,p} \right\rangle_{\mathbf{r},E}} = \frac{\left\langle \phi_{0,k}^+, \left[\chi \mathbf{F} - \mathbf{L}\right] \phi_{0,p} \right\rangle_{\mathbf{r},E}}{\left\langle \phi_{0,k}^+, \chi \mathbf{F} \phi_{0,p} \right\rangle_{\mathbf{r},E}}. \tag{4.53}$$

Then, according to the definition of the prompt α-eigenvalue problem as shown in Equation 2.23, the reactivity ρ in Equation 4.53 can be calculated by

$$\begin{aligned}
\rho \quad &= \quad \frac{\left\langle \phi_{0,k}^+, \left[(1-\beta)\chi_p \mathbf{F} - \mathbf{L}\right] \phi_{0,p} \right\rangle_{\mathbf{r},E}}{\left\langle \phi_{0,k}^+, \chi \mathbf{F} \phi_{0,p} \right\rangle_{\mathbf{r},E}} + \frac{\left\langle \phi_{0,k}^+, \chi_d \beta \mathbf{F} \phi_{0,p} \right\rangle_{\mathbf{r},E}}{\left\langle \phi_{0,k}^+, \chi \mathbf{F} \phi_{0,p} \right\rangle_{\mathbf{r},E}} \\
&= \quad \frac{\left\langle \phi_{0,k}^+, \alpha_0 v^{-1} \phi_{0,p} \right\rangle_{\mathbf{r},E}}{\left\langle \phi_{0,k}^+, \chi \mathbf{F} \phi_{0,p} \right\rangle_{\mathbf{r},E}} + \frac{\left\langle \phi_{0,k}^+, \chi_d \beta \mathbf{F} \phi_{0,p} \right\rangle_{\mathbf{r},E}}{\left\langle \phi_{0,k}^+, \chi \mathbf{F} \phi_{0,p} \right\rangle_{\mathbf{r},E}} \\
&= \quad \alpha_0 \bar{\Lambda}_0 + \bar{\beta},
\end{aligned} \tag{4.54}$$

with the decay constant α_0 obtained from the measurement, and the mean generation time Λ_0 and the effective delayed-neutron fraction β defined similar to Equation 2.38 and 2.40:

$$\bar{\Lambda}_0 = \frac{\left\langle \phi_{0,k}^{+}, v^{-1}\phi_{0,p} \right\rangle_{\mathbf{r},E}}{\left\langle \phi_{0,k}^{+}, \chi\mathbf{F}\phi_{0,p} \right\rangle_{\mathbf{r},E}}, \tag{4.55}$$

$$\bar{\beta} = \frac{\left\langle \phi_{0,k}^{+}, \chi_d\beta\mathbf{F}\phi_{0,p} \right\rangle_{\mathbf{r},E}}{\left\langle \phi_{0,k}^{+}, \chi\mathbf{F}\phi_{0,p} \right\rangle_{\mathbf{r},E}}. \tag{4.56}$$

In practice, one of the technical difficulties of applying the α-method is that the detector responses might not follow a single-exponential decay in any interval within the neutron pulse period. If we take the logarithm of the detector responses as shown in Equation 4.51,

$$\alpha(\mathbf{r_D}, t) = \frac{\partial \ln R(\mathbf{r}_D, t)}{\partial t} = \frac{\partial}{\partial t}\left[\sum_{m}^{M} A_m(\Delta T)\left\langle \Sigma_d, \phi_{m,p} \right\rangle_E e^{\alpha_m(t-\Delta T)}\right], \tag{4.57}$$

the decay constant is a space- and time-dependent function due to the high-order harmonics contaminations. If all the high-order modal terms with $m \geq 1$ damped away, the eigenvalue α_0 corresponding to the fundamental prompt α-mode is the asymptotic value of $\alpha(\mathbf{r}_D, t)$, and is spatially independent. In other words, theoretically, a spatially independent and time-invariant decay constant can always be obtained if we wait long enough in the pulsed-neutron experiment, with delayed neutrons ignored. However, due to the limited efficiency of the neutron detectors, the fundamental exponential decay curve might not be separated from high-order modal terms before the detector responses die out. Thus, it may be infeasible to retrieve the fundamental decay constant α_0 from the experimental data.

4.2.2 The modified α-method

The modified α-method is a way of obtaining the reactivity from pulsed-neutron experiments, if the fundamental decay constant can not be properly retrieved. It was proposed by Kulik [17] to eliminate the spatial variations in the MUSE-4 pulsed-neutron experiments. The advantage of this method is that it does not require the calculation of any decay constant to obtain the reactivity. Therefore, this method provides a good way of obtaining reactivities for a subcritical reactor, if the decay constant obtained from the experimental data is spatially dependent.

The modified α-method is derived from the quasi-static space-time kinetics equations with delayed neutrons ignored in the prompt-neutron decay period. If we use $\phi^+_{0,k}$ as the weighting function and assume that the delayed-neutron flux is negligible compared with the prompt-neutron flux, Equation 2.36 can be reduced to

$$\frac{dT(t)}{dt} = \frac{\rho(t) - \beta(t)}{\Lambda(t)} T(t), \tag{4.58}$$

where $\beta(t)$, $\rho(t)$ and $\Lambda(t)$ are kinetics parameters defined in Equation 2.38, 2.39 and 2.40, respectively. According to the definition of the adjoint k-eigenvalue Equation 2.15, the reactivity $\rho(t)$ can be reduced to

$$\begin{aligned} \rho(t) &= \frac{\left\langle [\chi\mathbf{F} - \mathbf{L}]^+ \phi^+_{0,k}, \psi \right\rangle_{\mathbf{r},E}}{\left\langle [\chi\mathbf{F}]^+ \phi^+_{0,k}, \psi \right\rangle_{\mathbf{r},E}} \\ &= 1 - \frac{\left\langle \mathbf{L}^+ \phi^+_{0,k}, \psi \right\rangle_{\mathbf{r},E}}{\left\langle [\chi\mathbf{F}]^+ \phi^+_{0,k}, \psi \right\rangle_{\mathbf{r},E}} = 1 - \frac{1}{k_0} = \rho_0, \end{aligned} \tag{4.59}$$

where ρ_0 is the static reactivity of the subcritical system. Thus, by integrating Equation 4.58 over an interval $[t_1,\ t_2]$ within the prompt-neutron decay region, ρ_0 can be easily obtained as

$$\rho_0 = \beta + \frac{T(t_2) - T(t_1)}{\int_{t_1}^{t_2} T(t)/\Lambda(t) dt}, \tag{4.60}$$

where β is usually a constant during the transient.

In order to obtain ρ_0, the amplitude function $T(t)$ has to be calculated first. In the pulsed-neutron experiment, the detector response measured at detector position

$\mathbf{r}_D$ can be expressed as

$$R(\mathbf{r}_D, t) = \langle \Sigma_d(\mathbf{r}_D, E), \phi(\mathbf{r}, E, t) \rangle_E = T(t) \langle \Sigma_d, \psi \rangle_E . \tag{4.61}$$

Therefore, if the shape function term $\langle \Sigma_d, \psi \rangle_E$ can be calculated numerically, the amplitude function at position $\mathbf{r_D}$ can be obtained by combining the measured detector response R with the calculated shape function:

$$T(\mathbf{r}_D, t) = \frac{R(\mathbf{r}_D, t)}{\langle \Sigma_d, \psi \rangle_E^{cal}} . \tag{4.62}$$

Then ρ_0 can be obtained at each detector position via Equation 4.60, with T calculated from Equation 4.62, and $\beta(t)$ and $\Lambda(t)$ calculated from the numerical simulations.

Theoretically, $[t_1,\ t_2]$ can be any interval within the prompt neutron decay period. Therefore, the modified α-method is capable of obtaining reactivities, even though high-order modal terms do not decay away. A drawback of this method is that the accuracy of the reactivity is highly related to the accuracy of the numerical simulations.

For instance, if we assume that $[t_1,\ t_2]$ is located in the prompt neutron decay region where all the high-order harmonics decayed away, the neutron flux is the fundamental modal term

$$\phi(\mathbf{r}, E, t) = T(t)\psi(\mathbf{r}, E, t) = A_0(t)\phi_{0,p}(\mathbf{r}, E), \tag{4.63}$$

and the shape function ψ is equal to the time-independent fundamental α-mode $\phi_{0,p}$. The amplitude function $T(t)$ is the coefficient $A_0(t)$ corresponding to the fundamental modal term. Then, the quasi-static $\Lambda(t)$ between $[t_1,\ t_2]$ can be calculated as

$$\Lambda(t) \quad = \quad \frac{\gamma}{\left\langle \phi_{0,k}^{+}, \chi \mathbf{F} \phi_{0,p} \right\rangle_{\mathbf{r},E}} = \frac{\left\langle \phi_{0,k}^{+}, v^{-1} \phi_{0,p} \right\rangle_{\mathbf{r},E}}{\left\langle \phi_{0,k}^{+}, \chi \mathbf{F} \phi_{0,p} \right\rangle_{\mathbf{r},E}} = \bar{\Lambda}_0, \tag{4.64}$$

which is a constant and equivalent to $\bar{\Lambda}_0$ defined in Equation 4.55. Similarly, $\beta(t)$ is also a constant in the time interval $[t_1,\ t_2]$ and is equivalent to $\bar{\beta}_0$. According to the modified α-method, the static reactivity can be obtained as

$$\rho_0 = \bar{\beta}_0 + \bar{\Lambda}_0 \frac{R(\mathbf{r}_D, t_2) - R(\mathbf{r}_D, t_1)}{\int_{t_1}^{t_2} R(\mathbf{r}_D, t)dt} = \bar{\beta}_0 + \bar{\Lambda}_0 \alpha_0, \tag{4.65}$$

where α_0 is the fundamental decay constant obtained from the measured detector responses. Thus, the modified α-method is equivalent to the α-method as shown in Equation 4.54, with the fundamental decay constant measured from the experimental data but the mean generation time calculated directly from the numerical simulations. In actual pulsed-neutron experiments, it is often difficult to accurately calculate the mean generation time $\Lambda(t)$ for a subcritical reactor using numerical methods, due to the errors in modeling the reactor geometry, material compositions and neutron cross section data. Thus, any systematic error in the numerical model will directly affect the reactivity obtained from the modified α-method.

4.2.3 The mean generation time correction factor

For the traditional α-method, the kinetics parameter $\bar{\Lambda}_0$ and $\bar{\beta}$ are measured in a reference configuration, which is close-to-critical and similar to the subcritical reactor in material compositions and geometry configurations. However, the mean generation time of the subcritical reactor might be significantly different from that of a reference configuration. Thus, to obtain a better approximation of the mean generation time of the subcritical reactor, we propose to use the measured mean generation time Λ^m_{ref} in a reference reactor calibrated by a correction factor f_Λ, which is calculated from the numerical simulations.

The simplest correction factor is the ratio of Λ_{sub} and Λ_{ref} calculated from the numerical simulations for the reference configuration and for the subcritical configuration, respectively:

$$f_\Lambda = \left[\frac{\Lambda_{sub}}{\Lambda_{ref}}\right]^{cal}. \tag{4.66}$$

Then, the mean generation time Λ for the subcritical configuration is obtained by

$$\Lambda = \Lambda_{ref}^{m} f_\Lambda. \tag{4.67}$$

Because the correction factor f_Λ is the ratio of two quantities obtained from the same numerical model, the systematic modeling error is then expected to be reduced.

Overall, the traditional α-method measures the prompt-neutron decay constant α from the measured detector responses, and calculates the reactivity with the kinetics parameter Λ and β measured in a reference reactor. There are two major technical difficulties with this method. For a subcritical reactor, the first one is that the fundamental prompt-neutron decay constant may not be properly retrieved from the experimental data. The modified α-method of Equation 4.60 is a good way of obtaining reactivities for this case. Another difficulty is that the mean generation time Λ varies from the reference reactor to the subcritical reactor. The measured Λ in the reference reactor can be calibrated with a correction factor f_Λ, which can be obtained from numerical simulations.

CHAPTER V

Krylov Subspace Methods to Obtain the Time-Eigenfunctions

5.1 Eigenvalue problems

In pulsed neutron experiments performed to measure the reactivity of a system, the difference between the α- and k-modes reveals the presence of the spectral and spatial effects of the area-ratio methods. To apply the method developed in Chapter IV, it is crucial to be able to calculate both the k- and α-modes corresponding to the reactor configuration. Furthermore, the α-modes are the appropriate ones in reactor dynamics studies, when the time-dependent behavior of the system is of primary interest. For instance, Kaplan [36] fully discussed the nice finality property of the α-modes, i.e., the expansion coefficients are independent of the number of terms retained, which renders them more useful than the k-modes in a modal expansion of the time-dependent flux.

For convenience, we rewrite the k-eigenvalue problem as

$$\mathbf{L}\phi = \frac{1}{k}\chi\mathbf{F}\phi. \tag{5.1}$$

We also rewrite the α-eigenvalue problem of a reactor system as

$$\frac{1}{\alpha}\begin{bmatrix}\phi \\ C\end{bmatrix} = \left\{\begin{bmatrix}\frac{1}{v} & 0 \\ 0 & 1\end{bmatrix}^{-1}\mathbf{A}_\alpha\right\}^{-1}\begin{bmatrix}\phi \\ C\end{bmatrix}, \tag{5.2}$$

where the system matrix $\mathbf{A}_\alpha$ is defined as

$$\mathbf{A}_\alpha = \begin{bmatrix} (1-\beta)\,\chi_p\mathbf{F} - \mathbf{L} & \chi_d\lambda \\ \beta\mathbf{F} & -\lambda \end{bmatrix}. \tag{5.3}$$

For a critical system, i.e., with $k_0 = 1$ and $\alpha = 0$, the fundamental k-mode and α-mode satisfy the same equation and are identical. However, for high-order modes or non-critical systems, the two eigenvalue equations are not equivalent.

Traditionally, the fundamental k-mode is calculated by the power iteration method. A drawback of this method is that it is only designed to calculate the fundamental mode. Although the high-order modes can be obtained by filtering out the converged low-order modes, the method is not efficient in cases where the low-order modes are not dominant. With delayed neutrons ignored, the fundamental prompt α-mode can also be obtained by an approach which varies the α/v term in a k-mode calculation,

$$\left[\frac{\alpha}{v} + \mathbf{L}\right]\phi = \frac{1}{k}\left[(1-\beta)\,\chi_p\right]\mathbf{F}\phi, \tag{5.4}$$

till $k = 1$. However, with this approach, the α/v term may lead to a problem which has zero or negative absorption cross sections and is difficult to solve. In addition, the high-order prompt α-modes are hard to obtain by this approach.

Recently, to obtain prompt α-eigenvalues, Modak [37] used the orthmin(k) method to minimize the residual norm:

$$||r|| = \left|\left|\left[(1-\beta)\,\chi\mathbf{F} - \mathbf{L}\right]\phi - \frac{\alpha}{v}\phi\right|\right|. \tag{5.5}$$

With this method, in order to converge to a desired high-order mode, a sufficiently accurate initial guess has to be supplied. For an asymmetric heterogeneous reactor, this is usually not a trivial task. At the same time, the method is not efficient since only one mode can be obtained at each iteration.

The Arnoldi method is known as a powerful method to calculate multiple eigenvectors of a linear system simultaneously. It is easy to be applied by using the ARPACK software [38] which implements the Implicit Restarted Arnoldi Method (IRAM) efficiently. Lathouwers [39] applied ARPACK to obtain the prompt α-modes for a 1-D transport problem. Warsa, et al. [40] also used this package to calculate high-order k-modes and compared the efficiency of IRAM with the power iteration method explicitly.

In this chapter, we present our calculations of α-modes and k-modes for 2-D diffusion problems. With the ARPACK software, we are able to obtain not only the fundamental and high-order prompt α-modes, but also the first few delayed α-modes. In the next section, we briefly describe the Arnoldi method, and how this method is applied to solve the k- and α-eignevalue problems. The implementation of the Arnoldi method for both α-modes and k-modes requires an inner-outer iteration scheme, and normally the inner iteration takes most of the CPU time. Therefore, we will also focus on describing the inner iteration solvers, including SOR (Successive Overrelaxation), LSQR, GMRES (Generalized Minimum RESidual) and BICGSTAB (BiConjugate-Gradient STABilized). Preconditioners which help to accelerate the inner iterations are also discussed. Finally, IRAM is compared with the power iteration method in terms of both efficiency and accuracy. The fundamental and high-order α-modes are verified by examining a modal expansion of the time-dependent flux for a pulsed-neutron experiment in a subcritical reactor.

5.2 Outer iterative solvers

5.2.1 The power iteration method

To obtain the eigenvalue which is the largest in magnitude (LM) of a typical eigenvalue problem,

$$\mathbf{A}x = \lambda x, \tag{5.6}$$

the traditional power iteration method starts from an arbitrary initial vector x_0 and computes $\mathbf{A}x_0$, $\mathbf{A}^2x_0$, $\cdots$ till the sequence is converged. At the m^{th} step, the LM eigenvalue can be estimated as

$$\lambda_{m,0} = \frac{||\mathbf{A}x_{m-1}||}{||x_{m-1}||} = \frac{||\mathbf{A}^m x_0||}{||\mathbf{A}^{m-1}x_0||}. \tag{5.7}$$

The vector which the sequence converges to is the corresponding eigenvector and is denoted as $\hat{x}_0$. The great advantage of the power iteration method is its simplicity. In the above iterative procedure, the method only requires a matrix-vector operation,

$$x_m = \mathbf{A}x_{m-1}, \tag{5.8}$$

with given vector x_{m-1}. In the nuclear engineering field, the system matrix $\mathbf{A}$ is usually a large sparse matrix. Direct methods, e.g., QR algorithm, will easily destroy the sparse property of $\mathbf{A}$. Since the power iteration method only requires a matrix-vector operation, it saves the computational storage and is easy to implement.

The power iteration method also has several disadvantages. First of all, it is designed only to calculate the dominant eigenvalue. Theoretically, high-order eigenvalues and eigenvectors can also be obtained with this method by filtering out low-order modes. For instance, to obtain the eigenvector which corresponds to the second largest eigenvalue in magnitude, the power iteration method is first utilized to obtain $\hat{x}_0$ with the arbitrary initial guess x_0. Then, the power iteration restarts with an updated initial guess x_1 which is calculated as

$$x_1 = x_0 - \frac{\langle x_0, \hat{x}_0 \rangle}{\langle \hat{x}_0, \hat{x}_0 \rangle} \hat{x}_0. \tag{5.9}$$

The converged vector of the second power iteration sequence is the desired eigenvector $\hat{x}_1$. Apparently, in order to obtain the n^{th}-mode, the power iteration method has to be restarted at least n times.

Another disadvantage of the power iteration method is that the method discards the old information as it proceeds. In other words, at the m^{th} step, only $\mathbf{A}^m x_0$ and $\mathbf{A}^{m-1} x_0$ are saved. As a result, the calculations of high-order eigenvalues need to largely repeat the calculations done in the previous power iterations. For simplicity, we assume the eigenvectors $\hat{x}_0, \hat{x}_1, \cdots$ are orthogonal to each other and are complete. The arbitrary initial guess x_0 can then be expanded as

$$x_0 = a_0 \hat{x}_0 + a_1 \hat{x}_1 + \cdots + a_n \hat{x}_n + \cdots , \tag{5.10}$$

where a_n is the expansion coefficient corresponding to the n^{th} eigenvector. In order to obtain $\hat{x}_1$, the power iteration has to be performed twice. At the m^{th} step of the first power iteration, the matrix-vector operation is performed m times to obtain the vector $x_{m,0}$,

$$x_{m,0} = \mathbf{A}^m x_0 = a_0 \mathbf{A}^m \hat{x}_0 + a_1 \mathbf{A}^m \hat{x}_1 + \cdots + a_n \mathbf{A}^m \hat{x}_n + \cdots , \tag{5.11}$$

and in the second iteration, the matrix-vector operation has to be performed another m times to obtain the vector $x_{m,1}$,

$$x_{m,1} = \mathbf{A}^m x_1 = a_1 \mathbf{A}^m \hat{x}_1 + \cdots + a_n \mathbf{A}^m \hat{x}_n + \cdots , \tag{5.12}$$

However, if the results of every matrix-vector operation in the first power iteration is saved, the sequence in the second power iteration can be obtained directly. For instance, $x_{m,1}$ can be rewritten as

$$x_{m,1} = \mathbf{A}^m x_1 = \mathbf{A}^m x_0 - \frac{\langle x_0, \hat{x}_0 \rangle}{\langle \hat{x}_0, \hat{x}_0 \rangle} \mathbf{A}^m \hat{x}_0 = x_{m,0} - \frac{\langle x_0, \hat{x}_0 \rangle}{\langle \hat{x}_0, \hat{x}_0 \rangle} \lambda_0^m \hat{x}_0. \tag{5.13}$$

Yet, an additional disadvantage of the power iteration method is that its convergence rate is highly dependent on the dominance ratio γ which is defined as

$$\gamma = \frac{\lambda_1}{\lambda_0}, \tag{5.14}$$

where λ_0 and λ_1 are the largest and the second largest eigenvalues in magnitude of the system, respectively. The power iteration stops when the direction of the vector x_m is sufficiently close to the direction of $\hat{x}_0$. By substituting Equation 5.6 into the Equation 5.11, the normalized x_m could be obtained as

$$x_m = a_0 \hat{x}_0 + a_1 \left(\frac{\lambda_1}{\lambda_0} \right)^m \hat{x}_1 + \cdots + a_n \left(\frac{\lambda_n}{\lambda_0} \right)^m \hat{x}_n + \cdots . \tag{5.15}$$

If γ is close to 1, a large m is required for x_m to converge to $\hat{x}_0$.

5.2.2 The Arnoldi method

The Arnoldi method [41] is designed to retain all the past information in the power iteration method. Its basic idea is to build an orthogonal basis $\mathbf{V}_m = [v_1, v_2, \cdots v_m]$ of the Krylov subspace $\mathcal{K}_m$ which is spanned by the power iteration sequence:

$$\mathcal{K}_m(\mathbf{A}, x_0) = \operatorname{span} \left\{ x_0, \mathbf{A}x_0, \mathbf{A}^2 x_0, \cdots , \mathbf{A}^{m-1} x_0 \right\}. \tag{5.16}$$

The steps of building $\mathbf{V}_m$ is often referred to as the Arnoldi process. It starts with an arbitrary initial guess x_0, and sets the first basis vector v_1 equal to x_0. Then, at the m^{th} Arnoldi step, the basis vector v_m is obtained from the modified Gram-Schmidt method as

$$v_m = \mathbf{A} v_{m-1} - \sum_{l=1}^{m-1} \langle \mathbf{A} v_{m-1}, v_l \rangle v_l. \tag{5.17}$$

To write the Arnoldi process in a matrix form, we obtain

$$\mathbf{A}\mathbf{V}_m = \mathbf{V}_m\mathbf{H}_m + h_{m+1,m}e^T v_{m+1}, \tag{5.18}$$

where the vector e_m is a unit vector with only the m^{th} element nonzero, and $\mathbf{H}_m$ is an upper Hessenberg matrix, with its element $h_{i,j}$ defined as

$$h_{i,j} = \begin{cases} \langle \mathbf{A}v_j, v_i \rangle & j \geq i \\ \|v_{i+1}\| & j = i+1 \end{cases} \tag{5.19}$$

The Arnoldi process stops when $h_{m+1,m}$ vanishes. Then the system matrix $\mathbf{A}$ is transformed into the upper Hessenberg matrix $\mathbf{H_m}$ with $\mathbf{V}_m$ as the transforming matrix,

$$\mathbf{A}\mathbf{V}_m = \mathbf{V}_m\mathbf{H}_m. \tag{5.20}$$

Therefore, if y is an eigenvector of $\mathbf{H}_m$ corresponding to the eigenvalue λ, we can obtain

$$\mathbf{A}\mathbf{V}_m y = \mathbf{V}_m\mathbf{H}_m y = \lambda\mathbf{V}_m y, \tag{5.21}$$

which indicates that λ is also an eigenvalue of $\mathbf{A}$, with the eigenvector calculated as

$$x = \mathbf{V}_m y. \tag{5.22}$$

Usually, the dimension m of the Krylov subspace or the dimension of $\mathbf{H}_m$ is much smaller than the dimension of $\mathbf{A}$. The eigenvalues and eigenvectors of $\mathbf{H}_m$ can be obtained easily by simple methods, e.g., the QR algorithm. Therefore, multiple eigenvalues and eigenvectors can be obtained simultaneously within one Arnoldi process. In addition, the Arnoldi method also preserves the simplicity of the power iteration method. In particular, the Arnoldi process only requires a matrix-vector operation except for the additional arithmetical calculations.

The difficulty of implementing the Arnoldi method lies in the fact that m is unknown. For some problems, m becomes so large that a large memory is required to store the orthogonal vectors. Additionally, the number of matrix-vector operation also increases linearly as m increases. Due to the computer round-off errors, if m is large, it is also very difficult to maintain the orthogonality between a large set of vectors. The loss of orthogonality leads to severe numerical difficulties, such as missing eigenvectors or producing suspicious duplicated eigenvectors [38].

5.2.3 The Implicit Restarted Arnoldi method (IRAM)

The implicit restarting is an efficient way to overcome the intractable requirements for the computational storage and time by the Arnoldi method. The implicit restarting technique can also avoid the need to maintain a large vector set $\mathbf{V}_m$ in the Arnoldi method. The basic strategy is to restart the Arnoldi process after every m steps of the orthogonalization with a new starting vector, which is updated to enhance the components in the directions of the desired eigenvectors as well as to depress the components in other directions.

If the first k dominant eigenvalues are of primary interest, the best choice of the initial guess is

$$x_0 = a_0\hat{x}_0 + a_1\hat{x}_1 + \cdots + a_k\hat{x}_k, \tag{5.23}$$

in which $\hat{x}_k$ is the eigenvector corresponding to the k^{th} eigenvalue we are interested in. Then the Arnoldi process stops at its k^{th} step, and the k eigenvalues are obtained.

Usually, it is impossible to pick up such a perfect initial guess. Instead, a Krylov subspace with dimension $m = k + j$ and $j >= k$ is constructed by the Arnoldi process. The initial guess x_0 is randomly picked, so that x_0 may have significant components in all the eigenvector directions,

$$x_0 = a_0\hat{x}_0 + a_1\hat{x}_1 + \cdots + a_k\hat{x}_k + \cdots . \tag{5.24}$$

We first perform m Arnoldi steps with the initial guess x_0. Then the eigenvalues of $\mathbf{H}_m$ are calculated. Those eigenvalues are often referred to as Ritz values of $\mathbf{A}$. Although they are not exact eigenvalues of $\mathbf{A}$, they are good approximations to the exact ones. The eigenvectors x obtained from Equation 5.22 also indicate the approximate locations of the real eigenvectors.

In the next step, we update the initial vector x_0 in a way such that the components of x_0 in some of the undesired-eigenvector directions, e.g., $\hat{x}_{k+1}$, $\hat{x}_{k+2}$, $\cdots$, $\hat{x}_m$, are reduced. This procedure can also be viewed by operating a polynomial $p(\lambda_k)$ on each of the expansion term in equation 5.24:

$$x_0 = a_0 p(\lambda_0)\hat{x}_0 + a_1 p(\lambda_1)\hat{x}_1 + \cdots + a_n p(\lambda_k)\hat{x}_k + \cdots , \tag{5.25}$$

where λ_k is the k^{th} eigenvalue of $\mathbf{A}$. To suppress the component of x_0 in the $\hat{x}_{k+1}$, $\cdots$, $\hat{x}_m$ directions, the ideal polynomial is

$$p(\lambda) = (\lambda - \lambda_k)(\lambda - \lambda_{k+1}) \cdots (\lambda - \lambda_{m-1}). \tag{5.26}$$

Because the real eigenvalues are unknown, they are replaced by the Ritz values calculated from the previous Arnoldi process. This process to update x_0 can be easily realized by the QR shift algorithm.

In IRAM, the dimension of the Krylov subspace m is usually small and fixed, and the orthogonality can be easily fulfilled numerically. On the other hand, there is also no systematic way to determine an optimal value of m. To use the ARPACK software, it is only required that m is no less than twice the number of the desired eigenvectors [38]. Generally, a large m will always lead to a faster convergence of IRAM, at the expense of increased computational costs for each iteration. For instance, to seek the dominant eigenvalue λ_0, the convergence rate of IRAM with $m = 3$ is often comparable to λ_3/λ_0.

In addition, the power iteration method can also be seen as a special example of the restarted Arnoldi method, with the subspace dimension $m = 1$, and the updating polynomial $p(\lambda)$ to be

$$p(\lambda) = \frac{\lambda}{\lambda_0}. \tag{5.27}$$

As we have discussed in Section 5.2.1, the convergence rate of the power iteration method for λ_0 is then determined by the dominance ratio λ_1/λ_0.

5.2.4 ARPACK and applications to k- and α-modes

ARPACK (Arnoldi PACKage) is a group of FORTRAN 77 subroutines which implement the Implicit Restarted Arnoldi Method to solve eigenvalue problems for sparse matrices [38]. It only requires a user-supplied subroutine to perform the matrix-vector operation. With this package, in principle, we are able to calculate multiple eigenvalues at various positions of the spectrum, such as LM and SM, which represent the largest and smallest eigenvalues in magnitude. However, similar to the power iteration method, it is more effective in calculating the dominant eigenvalues. For eigenvalues other than LM eigenvalues, an inverse-shift technique is applied. For example, with ARPACK, it is often more convenient to seek the LM eigenvalues of $\mathbf{A}^{-1}$ instead the SM eigenvalues of $\mathbf{A}$.

In our applications, the LM eigenvalues are our primary interests for the k-eigenvalue problem. Thus, Equation 5.1 is directly rearranged to the standard form of an eigenvalue problem as

$$k\phi = \mathbf{L}^{-1}\chi\mathbf{F}\phi \tag{5.28}$$

For the α-eigenvalue problem of a subcritical system, we are interested in the SM eigenvalues. Therefore, an inverse technique is applied. By ignoring the delayed neutrons, the standard form of the prompt α-eigenvalue problem can be obtained from Equation 5.2 as

$$\frac{1}{\alpha_p}\phi = \left\{ \left(\frac{1}{v}\right)^{-1} \left[(1-\beta)\,\chi_p \mathbf{F} - \mathbf{L} \right] \right\}^{-1} \phi. \tag{5.29}$$

For delayed α-modes, we choose to solve the flux ϕ and the precursor density function C jointly, i.e., Equation 5.2 is directly solved.

5.3 The fixed source problems and the inner iterative solvers

In IRAM, in order to build the orthogonal basis $\mathbf{V}_m$, a user subroutine has to be supplied to calculate the product of a matrix $\mathbf{A}$ and a given vector x_0. In other words, to obtain the k-eigenvalues, the prompt α-eigenvalues and the delayed α-eigenvalues, we need to solve three fixed source problems, respectively:

$$\mathbf{A}_k y = \mathbf{L} y = \chi \mathbf{F} x_0, \tag{5.30}$$

$$\mathbf{A}_{\alpha,p} y = \left[(1-\beta)\,\chi_p \mathbf{F} - \mathbf{L} \right] y = \frac{1}{v} x_0, \tag{5.31}$$

$$\mathbf{A}_{\alpha} y = \begin{bmatrix} \frac{1}{v} & 0 \\ 0 & 1 \end{bmatrix} x_0. \tag{5.32}$$

Discretizing the fixed source problems in space and energy domains leads to a linear equation:

$$\mathbf{A} x = b, \tag{5.33}$$

where $\mathbf{A}$ is a large sparse asymmetric matrix. Direct methods, e.g., LU decompositions, often easily destroy the sparsity of the matrix, and therefore, are not appropriate to solve large sparse linear systems. Iterative methods, which are usually referred to as inner iterations, are favored to solve such problems. Likewise, the iterations performed by IRAM are referred to as outer iterations in solving an eigenvalue problem. Because the inner-iteration subroutine is repetitively called by the outer iteration, a good inner-iterative solver can greatly accelerate the overall calculations.

5.3.1 Classic iterative methods

Traditionally, a straightforward way to solve Equation 5.33 iteratively is to split the matrix $\mathbf{A}$ as

$$\mathbf{A} = \mathbf{M} - \mathbf{N}. \tag{5.34}$$

Then, the linear equation is transformed into a new equation:

$$\mathbf{M}x = \mathbf{N}x + b. \tag{5.35}$$

Consequently, an iterative scheme can be constructed from the above equation as

$$\mathbf{M}x^{k+1} = \mathbf{N}x^k + b. \tag{5.36}$$

In order to solve Equation 5.36, $\mathbf{M}$ is chosen to be a matrix which is easy to invert. The performance of the method is highly dependent on the choice of the matrix $\mathbf{M}$. Table 5.1 lists the $\mathbf{M}$-matrix for each of the classic iterative methods, e.g., the Jacobi's method, the Gauss-Seidel method, the successive overrelaxation (SOR) method and the symmetric successive overrelaxation (SSOR) method. In the table, $\mathbf{A} = \mathbf{D} - \mathbf{L} - \mathbf{U}$, with $\mathbf{D}$, $\mathbf{L}$ and $\mathbf{U}$ representing the diagonal, the lower triangular part and the upper triangular part of $\mathbf{A}$, respectively. The variable ω is the relaxation parameter of the successive overrelaxation scheme.

In the past, the SOR method and its variants achieved great success in solving neutron balance equations. The algorithm is very simple and easy to be implemented

Table 5.1: **M**-matrices for the classic iterative methods.

Methods	Jacobi's	Gauss-Seidel	SOR	SSOR
$\mathbf{M}$ – matrix	$\mathbf{D}$	$\mathbf{D}-\mathbf{L}$	$\frac{1}{\omega}\mathbf{D}-\mathbf{L}$	$\frac{\omega}{2-\omega}\left[\frac{1}{\omega}\mathbf{D}-\mathbf{L}\right]\mathbf{D}^{-1}\left[\frac{1}{\omega}\mathbf{D}-\mathbf{U}\right]$

as shown in Appendix A.1. With an optimal relaxation parameter ω, the SOR method is very effective to solve diagonally-dominant linear systems. However, its convergence rate is sensitive to ω, where its optimal value is often unknown. The estimation of the optimal ω complicates the SOR algorithm itself, and demands more computational effort. In addition, the convergence of the SOR method is only guaranteed for diagonally dominant linear system, which may not be the case for the α-eigenvalue problem.

5.3.2 The conjugate gradient and LSQR methods

Another classic way of solving Equation 5.33 which does not require the estimation of an optimal parameter is the conjugate gradient (CG) method. It is an effective method to solve both non-diagonally and diagonally dominant linear systems. The method seeks an optimal solution $\hat{x}$ by minimizing the norm of the residual vector iteratively:

$$\hat{x} = \arg\min_{x} \|b - \mathbf{A}x\|. \tag{5.37}$$

It starts with an arbitrary initial guess x_0, and the first search direction p_0 along the residual direction r_0. Then at the k^{th} step of the iteration, the new guess x_{k+1} is updated by performing an exact line search in the search direction p_k,

$$x_{k+1} = x_k + \alpha p_k, \tag{5.38}$$

where α is obtained from the exact line search. The new search direction p_{k+1} is also updated to be a linear combination of the old search direction p_k and the new gradient direction r_{k+1} as

$$p_{k+1} = r_{k+1} + \beta p_k, \tag{5.39}$$

where β is determined by letting p_{k+1} conjugate to the previous search direction p_k. If $\mathbf{A}$ is symmetric, p_{k+1} is then automatically conjugate to all the previous search directions p_0, $\cdots$, p_k. However, if $\mathbf{A}$ is asymmetric, p_{k+1} is not guaranteed to be conjugate to all the previous search directions. Then, the CG method may not converge. Instead, if $\mathbf{A}$ is nonsingular, we can use the CG method to solve the normal equations:

$$\mathbf{A}^T\mathbf{A}x = \mathbf{A}^T b, \quad \text{or} \quad \mathbf{A}\mathbf{A}^T y = b \quad \text{with} \quad x = \mathbf{A}^T y. \tag{5.40}$$

The CG method is easy to implement since it also only requires a matrix-vector operation as shown in Appendix A.2. Its convergence rate is comparable to the SOR method with the optimal ω at the worst case [41]. However, its convergence rate is also sensitive to the conditioning of the linear system. For asymmetric linear systems, the condition number of the normal equations are the square of the condition number of $\mathbf{A}$. Usually, the CG method is not appropriate to solve the normal equations directly, due to the slow convergence rate and numerical instabilities.

The LSQR method is a CG-like method which is developed by Paige and Saunders [42]. It is a clever implementation of the Lanzcos process for the matrix $\mathbf{A}^T\mathbf{A}$, and is mathematically equivalent to applying the CG method on the normal equations. Like the CG method, its convergence rate is also sensitive to the conditioning of the linear system. Nonetheless, the method is also demonstrated to be numerically more stable than the method which applies the CG method directly to the normal equations. In this thesis, we also used the FORTRAN subroutine, which implements the LSQR algorithm and is developed by Saunders, to solve the fixed source problem.

5.3.3 The Krylov subspace method: GMRES(m)

In recent studies, the Krylov subspace method is one of the popular projection methods to solve nonsymmetric linear systems. The method also does not require any estimation of the relaxation parameter ω. As illustrated by Saad [43], its basic idea is to seek an approximate solution of the linear system in a specific subspace $\mathcal{K}_m$, which is normally referred to as the search space. The approximate solution is confined in $\mathcal{K}_m$ by the Petrov-Galerkin condition. Specifically, the solution is obtained by letting the residual vector be orthogonal to m independent vectors $\mathbf{V}_m = [v_1, \cdots, v_m]$,

$$r = b - \mathbf{A}x_m \perp \mathbf{V}_m. \tag{5.41}$$

The subspace spanned by $\mathbf{V}_m$ is referred to as the subspace of constraints or the left subspace $\mathcal{L}$. Different projection methods can be obtained with different $\mathcal{K}_m$s and $\mathcal{L}$s. For the Krylov subspace methods, the search subspace is the Krylov subspace $\mathcal{K}_m(\mathbf{A}, r_0)$ defined in Equation 5.16, where r_0 is the initial residual vector corresponding to the initial guess x_0. The constraint subspace $\mathcal{L}$ has a very important impact on the performance of the iterative methods. Currently, the GMRES and the BICGSTAB method are the two most popular subspace methods with left subspaces $\mathcal{L}$ equal to $\mathbf{A}\mathcal{K}_m(\mathbf{A}, r_0)$ and $\mathcal{K}_m(\mathbf{A}^T, r_0)$, respectively.

The GMRES algorithm is to seek the solution based on the Arnoldi process. It first performs m Arnoldi steps to build the orthogonal basis $\mathbf{V}_m$ with an initial guess $x_0 = 0$. Then at the m^{th} Arnoldi step, the method seeks the approximate solution x_m which is a linear combination of the basis vector V_m

$$x_m = \mathbf{V}_m y_m, \tag{5.42}$$

so that the the norm of the residual vector is minimized,

$$y_m = \arg\min_y \|b - \mathbf{A}\mathbf{V}_m y\|. \tag{5.43}$$

If we define $\beta = \|b\|$, with the Arnoldi process, the above minimization problem can then be reduced to a new minimization problem on a subspace with a much smaller dimension m:

$$\begin{aligned} y_m &= \arg\min_y \|b - \mathbf{V}_m \mathbf{H}_m y\| \\ &= \arg\min_y \|\mathbf{V}_m \left(\beta e_1 - \mathbf{H}_m y\right)\| \\ &= \arg\min_y \|\beta e_1 - \mathbf{H}_m y\|, \end{aligned} \tag{5.44}$$

which is easy to solve with the plane rotation technique. In addition, with more Arnoldi steps, the norm of the residue r_m is reduced. The GMRES method stops as the residual norm reaches its convergence criterion.

The GMRES method is guaranteed to converge in at most n steps, where n is the size of the system. However, similar to the Arnodi method, it is also important to restart the orthogonalization process after every m steps to maintain the orthogonality between the basis vectors and to save the computer storage. The restarted GMRES method is often named as GMRES(m), where m is the dimension of the Krylov subspace. Before restarting the Arnoldi process, the vector y_m is obtained by solving Equation 5.44, and the corresponding x_m is taken as the initial guess x_0 of the next m-step Arnoldi process. By restarting, the method may take more than n steps to converge. Furthermore, by restarting, the method may miss its fast convergence rate and the method may also stagnate if the subspace dimension is not large enough. The materials which discussed the GMRES method can be found in Saad's text book [43]. We include the GMRES(m) method in Appendix A.3.

5.3.4 The Krylov subspace method: BICGSTAB

The numerical difficulties in the CG method and the GMRES method in solving Equation 5.33 lies in the fact that the system matrix $\mathbf{A}$ is asymmetric. If $\mathbf{A}$ is symmetric, the Arnoldi process is equivalent to the well-known symmetric Lanczos process. Specifically, if $\mathbf{A}$ is symmetric, the upper Henssenberg matrix $\mathbf{H}_m$ obtained from the Arnoldi process is a triangular matrix. Therefore, Equation 5.17 is reduced to a three-term recurrence,

$$v_m = \mathbf{A}v_{m-1} - \langle \mathbf{A}v_{m-1}, v_{m-1} \rangle v_{m-1} - \langle \mathbf{A}v_{m-1}, v_{m-2} \rangle v_{m-2}, \tag{5.45}$$

and the computation effort of the orthogonalization process at the m^{th} step is greatly reduced.

For an asymmetric linear system, the Bi-CG method utilizes the two-side Lanczos process to build a pair of biorthogonal sequences $\mathbf{V}_m = [v_1 \cdots v_m]$ and $\mathbf{W}_m = [w_1 \cdots w_m]$ for the Krylov subspace $\mathcal{K}_m(\mathbf{A}, v_1)$ and $\mathcal{K}_m(\mathbf{A}^T, w_1)$ respectively. The process begins with an initial vector $w_1 = v_1$, and at the m^{th} step, we obtain v_{m+1} and w_{m+1} as

$$\begin{aligned} v_{m+1} &= \mathbf{A}v_m - \alpha_m v_m - \beta_m v_{m-1}, && (5.46) \\ w_{m+1} &= \mathbf{A}^T w_m - \alpha_m w_m - \delta_m w_{m-1}, && (5.47) \end{aligned}$$

where $\alpha_m = \langle \mathbf{A}v_m, w_m \rangle$, β_m and δ_m are only required to satisfy $\beta_m \delta_m = \langle v_m, w_m \rangle$. It can be verified that the basis vectors obtained from the above process are biorthogonal to each other:

$$\langle w_j, v_i \rangle = \delta_{ij}. \tag{5.48}$$

The big advantage of using the biorthogonal process rather than the Arnoldi process is that there is no need to numerically maintain orthogonality between a large set of vectors. One of the main disadvantages of the Bi-CG method is that it requires to perform both the forward and the adjoint matrix-vector operations. For some problems, the adjoint problem is not as easy as the forward problem. The CG-squared method uses another forward matrix-vector calculation to replace the adjoint calculation. However, this method becomes extremely sensitive to the computer round-off errors, and its convergence is irregular. The BICGSTAB method modifies the CG-squared method with a remedy of minimizing the 2-norm of the residual vector, so as to smooth the convergence irregularities and at the same time to maintain the fast convergence speed of the Bi-CG method. Given a detailed derivation of the BICGGSTAB method in text books [43, 44], we include its algorithm in Appendix A.4.

5.4 The preconditioning techniques

For most of the iterative methods, the convergence rate is dependent on the condition number of the system matrix **A**. In order to improve the performance of the inner-iteration solvers, linear systems are often transformed into new systems which have much better condition numbers. This technique is often called "preconditioning". As stated by Lanczos [45], the main goal of preconditioning is not to find the exact solution but to "reduce the initial skewness" of the system. In practice, for iterative methods, e.g., LSQR, GMRES and BICGSTAB, it is often important to find a preconditioner **M**, such that $\mathbf{M}^{-1}\mathbf{A}$ or $\mathbf{A}\mathbf{M}^{-1}$ has a better condition number than **A**. Thus, a new linear system is solved:

$$\mathbf{M}^{-1}\mathbf{A}x = \mathbf{M}^{-1}b, \tag{5.49}$$

or

$$\mathbf{A}\mathbf{M}^{-1}y = b, \tag{5.50}$$

with $x = \mathbf{M}^{-1}y$. Equation 5.49 with $\mathbf{M}$ on the left of $\mathbf{A}$ is usually referred to as the left preconditoning technique. Likewise, Equation 5.50 is referred to as the right precondtioning technique.

Good preconditioners are those with good approximations to the matrix $\mathbf{A}$, and are often easily obtained. In actual applications, usually $\mathbf{M}$ is not calculated explicitly. Instead a matrix-vector production of $\mathbf{M}$ is often more important. For instance, except the simple arithmetic calculations, GMRES only requires a matrix-vector operation to build the orthogonal basis such as

$$y = \mathbf{A}x_0, \tag{5.51}$$

with a given x_0. With the left preconditioning technique, the new system in Equation 5.49 is solved by the GMRES method. Therefore, to build a basis vector for the new system, we have to solve a new matrix vector operation defined as

$$y = \mathbf{M}^{-1}\mathbf{A}x_0, \quad \Rightarrow \quad \mathbf{M}y = \mathbf{A}x_0. \tag{5.52}$$

Thus, a good preconditioner $\mathbf{M}$ is a matrix which is also easy to invert numerically.

5.4.1 The SSOR preconditioner

The classic iterative methods, e.g., the Jacobi's method, the Gauss-Seidel method, the SOR method and the SSOR method, provide simple ways to invert matrix $\mathbf{M}$. For convenience, we rewrite their iterative scheme:

$$\mathbf{M}x^{k+1} = \mathbf{N}x^k + b. \tag{5.53}$$

If the iteration starts with an initial guess $x_0 = 0$, the first iterative step produces

$$\mathbf{M}x^1 = b. \tag{5.54}$$

Thus Equation 5.52 is solved explicitly if $b = \mathbf{A}x_0$ and $y = x^1$. All the **M** matrices corresponding to the classic iterative methods can serve as good preconditioners. The SSOR preconditioner is the most popular and effective one. To apply the SSOR preconditioner on the inner-iterative methods, it only requires one additional step of the forward SOR iteration followed by one step of the backward SOR iteration. In addition, regardless of how the relaxation parameter ω is chosen, the SSOR preconditioner usually improves the convergence rate of the inner iteration methods significantly.

5.4.2 The ILU preconditioners

Recently, the preconditioner technique has become one of the most popular methods to improve the performance of the iterative methods. There are many other advanced preconditoners based on incomplete factorizations, e.g., the incomplete LU decomposition (ILU) and the incomplete Cholesky (IC) factorization [46, 41]. Specifically, the basic idea of the ILU(p) preconditioners is very similar to the ILU with zero fill-ins (ILU(0)). We will only discuss the ILU(0) preconditioner in the thesis as an example of the incomplete factorization precoditioners.

For a square matrix **A**, if its leading principal submatrices are all non-singular, it can always be decomposed into a lower triangular matrix **L** and an upper triangular matrix **U**:

$$\mathbf{A} = \mathbf{L}\mathbf{U}. \tag{5.55}$$

Then, Equation 5.52 can be solved directly with a forward substitution followed by a backward substitution. For a large sparse **A**, because the LU decomposition easily destroys the sparsity of **A** and fills in the whole matrix, it is not suitable to solve such linear systems. However, if the LU decomposition is performed in an approximate but simple way, in other words, $\mathbf{A} \simeq \mathbf{M} = \mathbf{LU}$, $\mathbf{M}$ may be a good preconditioner.

A general effective way to derive the incomplete LU factorization is to perform the Gaussian elimination on the matrix $\mathbf{A}$, and then to drop elements in some predetermined positions. The simplest way is to drop all the fill-ins in the Gaussian elimination, and this technique is called ILU with zero fill-in, or denoted by ILU(0). Then, the decomposed $\mathbf{L}$ and $\mathbf{U}$ have the same sparse pattern as $\mathbf{A}$. In our work, we have limited our efforts on applying the SSOR and ILU(0) preconditoners because of their simplicity and effectiveness in solving our eigenvalue problems. In Appendix B, we include the detailed algorithms for both preconditioners.

5.5 2-D diffusion theory calculations

Overall, as shown in Figure 5.1, the ARPACK software combined with the inner-iteration solvers, such as SOR, LSQR, GMRES(m), or BICGSTAB, was implemented with standard Fortran 77 language to calculate both k- and α-modes. We adopted the UM2DB code, which is a substantially modified version of the 2DB code [47], to discretize the reactor geometries and read neutron cross section data. In addition, we used the SSOR preconditioner or the ILU(0) preconditioner to accelerate the inner iterations.

5.5.1 Accuracy of eigenvector calculations

In order to examine the accuracy of the fundamental k-mode calculated by IRAM, we performed a numerical 2-G, 2-D simulation of the Westinghouse AP600 design. The power iteration method, together with the successive line over relaxation method (SLOR) as the inner-iteration solver, was embedded in the original UM2DB code. Hence, we used this method to perform the first k-eigenvalue calculation, and obtained $k_{eff} = 0.99746$. The second k-eigenvalue calculation was performed with the

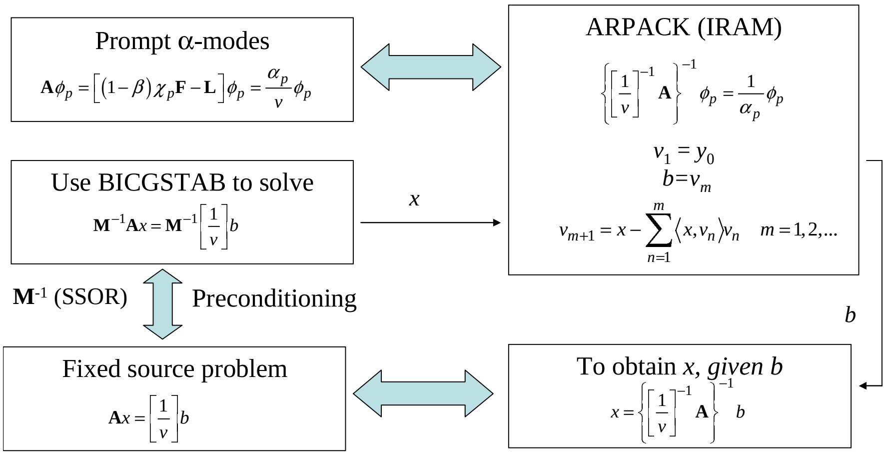

Figure 5.1: The scheme of the implementation of IRAM to solve the prompt α-eigenvalue problem.

IRAM implemented in ARPACK. The k_{eff} obtained from this method agrees with the power iteration result up to five significant digits. Furthermore, the fundamental k-modes calculated from the above two methods are close to each other at every point of the reactor, with a maximum difference of 0.06%. The power distributions based on the fundamental k-modes agree with the Westinghouse SSAR results [48] reasonably well, as shown in Figure 5.2.

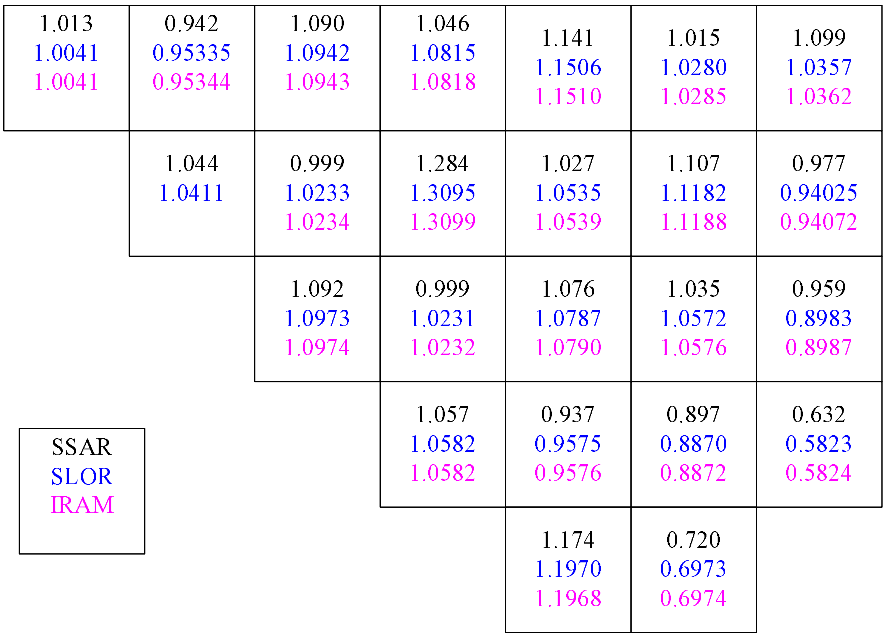

1.013 1.0041 1.0041	0.942 0.95335 0.95344	1.090 1.0942 1.0943	1.046 1.0815 1.0818	1.141 1.1506 1.1510	1.015 1.0280 1.0285	1.099 1.0357 1.0362
	1.044 1.0411	0.999 1.0233 1.0234	1.284 1.3095 1.3099	1.027 1.0535 1.0539	1.107 1.1182 1.1188	0.977 0.94025 0.94072
		1.092 1.0973 1.0974	0.999 1.0231 1.0232	1.076 1.0787 1.0790	1.035 1.0572 1.0576	0.959 0.8983 0.8987
SSAR SLOR IRAM			1.057 1.0582 1.0582	0.937 0.9575 0.9576	0.897 0.8870 0.8872	0.632 0.5823 0.5824
				1.174 1.1970 1.1968	0.720 0.6973 0.6974	

Figure 5.2: Normalized assembly power distribution for the AP600 core.

With delayed neutrons ignored, i.e., Equation 5.2 with $\beta = 0$, we used IRAM to calculate the fundamental α-eigenvalue of the AP600 core and obtained $\alpha = -6.98121\ \text{s}^{-1}$. Based on Equation 5.4, a k-eigenvalue calculation was also performed with the absorption term modified by the α/v term to yield $k_{eff} = 1.00000$, which verifies the accuracy of α calculated via IRAM. In addition, the flux obtained from the α-eigenvalue calculation shows an excellent agreement with the flux obtained from the k-eigenvalue calculation, with a maximum difference less than 0.0006%, which again proves the accuracy of the fundamental α-mode calculation with IRAM. The accuracy of the high-order α-modes calculated is also verified by performing a similar k-eigenvalue calculation with the modified absorption term α/v to obtain $k = 1.00000$ as one of the eigenvalues, although not the dominant one as expected.

Another more promising way of verifying that IRAM calculates α-modes accurately is to perform a quasi-static simulation of the pulsed neutron experiment, and then compare the α-mode synthetic fluxes with the quasi-static fluxes as shown in Figure 5.3.

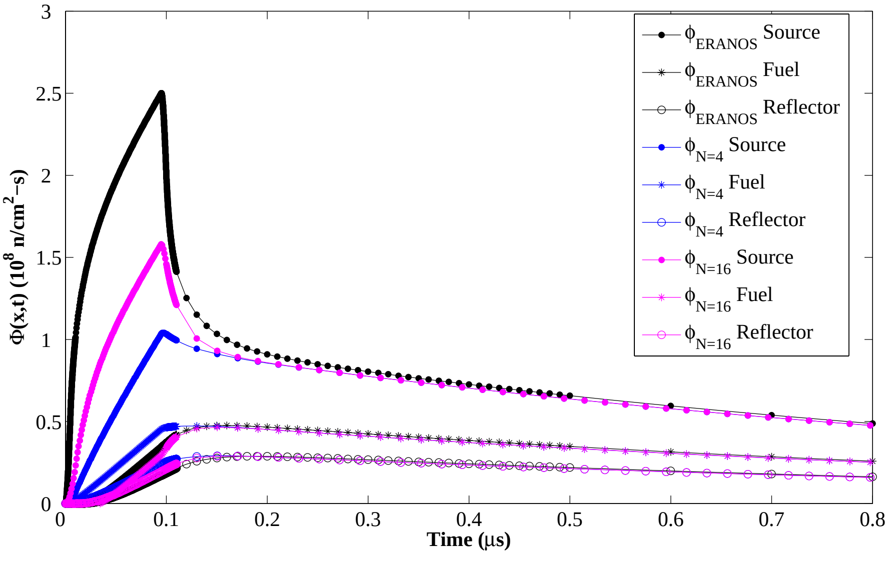

Figure 5.3: Comparison of α-mode expansion fluxes with quasi-static simulated fluxes.

The numerical simulations are performed in a 2-D x-y geometry core, with a 0.11 m × 0.11 m source region located at the center, a MOX type fuel with a thickness of 0.36 m surrounding the source region, and a sodium reflector with a thickness of 0.17 m outside the fuel region, as shown in Figure 5.4.

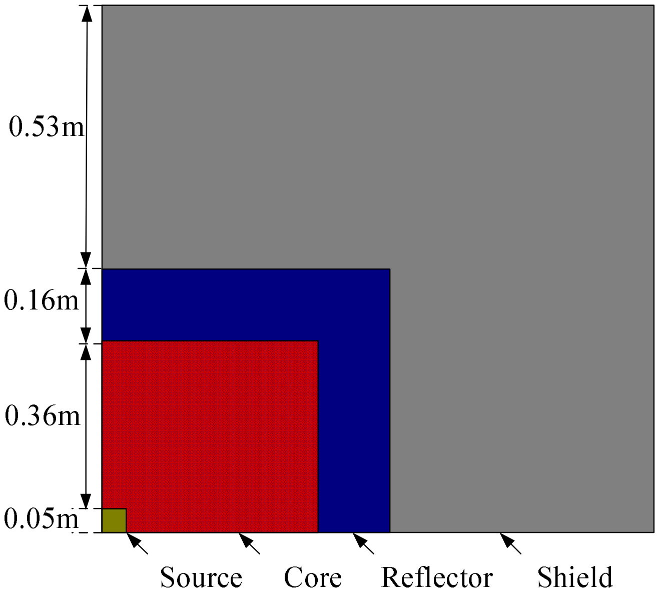

Figure 5.4: Quarter core map of the fast reactor.

The flux transient is initiated by injecting a neutron pulse in the source region. The time evolutions of the fluxes are simulated by the ERANOS code [31], with detectors put in the source, fuel and reflector regions respectively. The time-dependent fluxes at each detector position are shown in Figure 5.3, and we use the α-modes as the expansion functions. The α-modes $\phi_{n,p}$ are calculated via IRAM, and the expansion coefficients $A_n(t)$ are obtained with Equation 2.43. Then, the synthetic fluxes with expansion order N can be obtained as

$$\phi_N(\mathbf{r}, t) = \sum_{n=1}^{N} A_n(t)\phi_{n,p}(\mathbf{r}). \tag{5.56}$$

As shown in Figure 5.3, the synthetic fluxes with $N = 4$ or $N = 16$ are also illustrated at three different regions respectively. The modal expansion fluxes agree well with the ERANOS simulations after a short period of time, when the neutron pulse is turned off at $t = 0.1\ \mu s$. This excellent agreement confirms the accuracy of the fundamental α-mode calculation. Furthermore, Figure 5.3 also reveals that with a large number of modal expansion terms included, the synthetic fluxes agree better with the ERANOS quasi-static fluxes everywhere in the source, fuel and reflector regions. Hence, the accuracy of the high-order modes is again established.

In addition, a modal-local method, which combines a modal expansion with a specialized function representing the local variations in the neutron flux, can also help obtain a better approximation to the ERANOS simulation as also shown in Figure 5.3 [49]. The modal-local formulation expresses the space- and time-dependent flux as a combination of a local term f and a global term h determined by a modal synthesis method:

$$\phi_N(\mathbf{r},t) = f(\mathbf{r},t) + h(\mathbf{r},t) = f(\mathbf{r},t) + \sum_{n=1}^{N} A_n(t)\phi_{n,p}(\mathbf{r}). \tag{5.57}$$

The local component f is chosen such that it takes the substantial variations of the neutron flux when the pulsed-neutron source is injected into the reactor, and is assumed to be separable in the space and time domains:

$$f(\mathbf{r},t) = f_0(\mathbf{r})b(t), \tag{5.58}$$

where f_0 satisfies

$$\mathbf{L}(\mathbf{r})f_0(\mathbf{r}) = Q_0(\mathbf{r}), \tag{5.59}$$

and the time-dependent coefficient $b(t)$ satisfies

$$\left\langle f_0, \frac{1}{v} f_0 \right\rangle_{\mathbf{r}} \frac{db(t)}{dt} + \langle f_0, \mathbf{L}f_0 \rangle_{\mathbf{r}}\, b(t) = \langle f_0, Q_0 \rangle_{\mathbf{r}}\, \Delta Q_t. \tag{5.60}$$

Therefore, the time-dependent expansion coefficient $A_n(t)$ be obtained by

$$\begin{aligned}\frac{dA_n(t)}{dt} &= -\alpha_n A_n(t) + \frac{1}{\gamma_n}\left[\left\langle \phi^+_{n,p}, Q_0 \right\rangle_{\mathbf{r}} \Delta Q_t\right] \\ &- \frac{1}{\gamma_n}\left[\left\langle \phi^+_{n,p}, v^{-1} f_0 \right\rangle_{\mathbf{r}} \left(\frac{db(t)}{dt} + \alpha_n b(t)\right)\right]. \qquad (5.61)\end{aligned}$$

Overall, as shown in Figure 5.5(a), compared with the modal fluxes expansion in Figure 5.3, a better agreement between the modal-local fluxes and the ERANOS simulations can be achieved shortly after the neutron pulse is turned off, with expansion order $N = 16$, especially in the fuel and reflector regions. The modal-local method, with the k-eigenfunctions as the expansion functions [49] for the global term h, can also be used to approximate the time-dependent neutron fluxes well as shown in Figure 5.5(b). However, the α-modes are usually preferred due to its property of finality [36].

5.5.2 Efficiency of the IRAM method

As the power iteration method can be viewed as a special case of the Arnoldi method with the subspace dimension equal to 1. Its convergence rate is highly dependent on the dominance ratio λ_1/λ_0. IRAM (or ARPACK) adopted the implicit shift technique to dampen the undesired components. It is more efficient than the power iteration method for problems with dominance ratios close to 1. To demonstrate this point, we present a simple numerical test, which compares the number of inner iterations required by the two methods to converge as shown in Table 5.2.

Table 5.2: Comparison of the number iterations for the power iteration method and IRAM.

Methods	Power Iteration	IRAM	
		$m = 3$	$m = 10$
k-mode	791	106	51
α-mode	10	14	11

The calculations are performed in two cases: (1) the fundamental k-eigenvalue of the AP600 design, which has a dominance ratio of 0.975 and (2) the fundamental α-eigenvalue of the same AP600 design, which has a dominance ratio of 0.093. Both methods start from the same initial guess, and are augmented by the same inner iteration solver to achieve the same accuracy level. In addition, to apply IRAM, a small Krylov subspace with dimension $m = 3$ and a slightly larger subspace with $m = 10$ are tested. Table 5.2 indicates that IRAM outperforms the traditional power iteration method for the k-eigenvalue problem which has dominance ratios close to 1.0. IRAM also works equally well with the power iteration method for the α-eigenvalue problem which has a small dominance ratio. Additionally, Table 5.2 also indicates that IRAM converges faster by working with a larger subspace, hence, with a larger computer storage.

5.5.3 Efficiencies of the inner iterative solvers

In IRAM, the upper Hessenberg matrix usually has a much smaller size than the original matrix. Therefore, most of the computational work in the eigenvector calculations is dedicated to the inner iteration, and a good inner iteration solver can greatly improve the general efficiency. Table 5.3 summarizes the performance of the four inner-iteration solvers both for obtaining the fundamental k- and α-mode of the AP600 design. The LSQR method, the GMRES method and the BICGSTAB method are augmented by the SSOR right preconditioner with $\omega = 1.5$. In addition, the same ω is also chosen for the SOR method.

In the table, we compare the number of iterations required by each method to stop at the same convergence criterion. We also list the number of matrix-vector operations per iteration for all the methods, and the total CPU time required to solve the fixed source problem on the same computer.

Overall, the BICGSTAB method with the SSOR preconditioner outperforms other

Table 5.3: Comparison of the performance of the inner iteration solvers.

Methods		SOR ($\omega = 1.5$)	LSQR	GMRES ($m = 20$)	BICGSTAB
k-mode	$\mathbf{A}x$/iteration	2	21	2	2
	number of iterations	111	162	2	14
	CPU time (s)	0.220	1.272	0.190	0.110
α-mode	$\mathbf{A}x$/iteration	2	21	2	2
	number of iterations	10651	270	5	35
	CPU time (s)	23.2	1.83	0.681	0.240

methods for both the k- and the α-eigenvalue problems in terms of the computational storage and the computer time. The GMRES(m) method has a comparable convergence rate with the BICGSTAB method, but requires more computer storage. The SOR method performs poorly in calculating the α-modes, because the system matrix of the corresponding fixed source problem is not diagonally dominant. Although an estimation of the optimal relaxation parameter can accelerate the method considerably, the convergence rate would be still much slower than the Krylov subspace methods. The LSQR method only works modestly for both problems, and it converges much slower than both the GMRES method and that BICGSTAB method.

Additionally, we compare the number of iterations required by the BICGSTAB method to converge with different preconditioners. As shown in Table 5.4, the SSOR preconditoner can accelerate the inner iteration solver greatly, even with a less optimal relaxation parameter. The ILU(0) preconditioner works no better than the SSOR method in both our k- and α-eigenvalue problems.

Table 5.4: Comparison of the number of iterations required by BICGSTAB with or without the preconditioners.

Preconditioners	None	SSOR $\omega = 1.0$	SSOR $\omega = 1.5$	ILU(0)
k-mode	74	25	14	48
α-mode	220	50	35	128

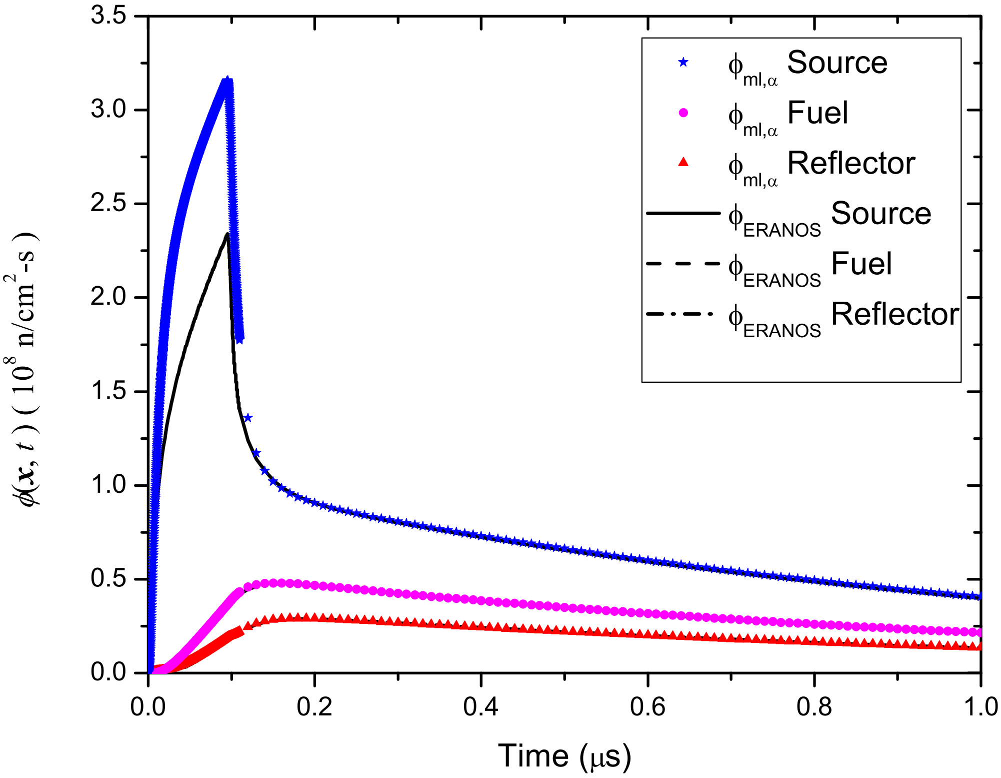

(a) With α-modes

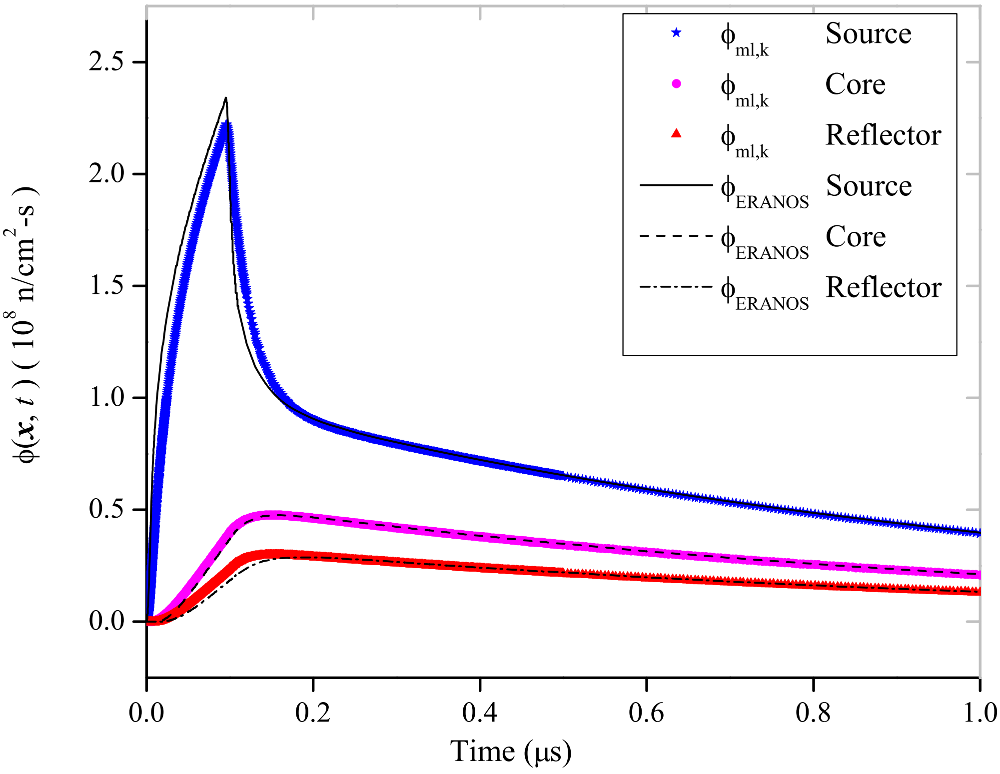

(b) With k-modes

Figure 5.5: Comparison of the quasi-static ERANOS simulated neutron fluxes with the modal-local fluxes (a) with α-modes as the expansion functions, (b) with k-modes the expansion functions.

CHAPTER VI

FX2-TH Numerical Tests

In this chapter, we first analyze the spatial effects in pulsed neutron experiments with numerical simulations. Specifically, we perform time-dependent numerical simulations of a pulsed-neutron experiment for a simple idealized reactor with the FX2-TH code. Our analysis of the spatial effects are then based on the detector responses simulated by the FX2-TH code. We consider a R-Z cylindrical reactor which has an external source region at the center with a radius of 0.02 m and a height of 0.19 m, as shown in Figure 6.1. A fuel region with a radius of 0.3 m and a core height of 0.57 m surrounds the source region, and a reflector region is the outermost region with a thickness of 0.5 m. The fuel region is composed of 8.5 wt% UO_2 fuel pins and a homogenized baffle region with 90% of stainless steel and 10% water. The four-group macroscopic cross sections and the ^{235}U detector efficiencies $\Sigma_{d,g}$ are calculated by the CASMO-3 code, with all the cross sections listed in Appendix C. The four-group diffusion calculation by the FX2-TH code gives $k_{eff} = 0.94797$. The β_{eff} is calculated to be 0.0072. The reference reactivity of the model is then -7.62 \$ [17].

To simulate a pulsed-neutron experiment, external pulsed neutrons are injected into the source region uniformly at the highest energy group with a 10 Hz frequency (or period $T = 0.1$ s). The pulse width is $\Delta T = 0.1$ μs. The detector responses are

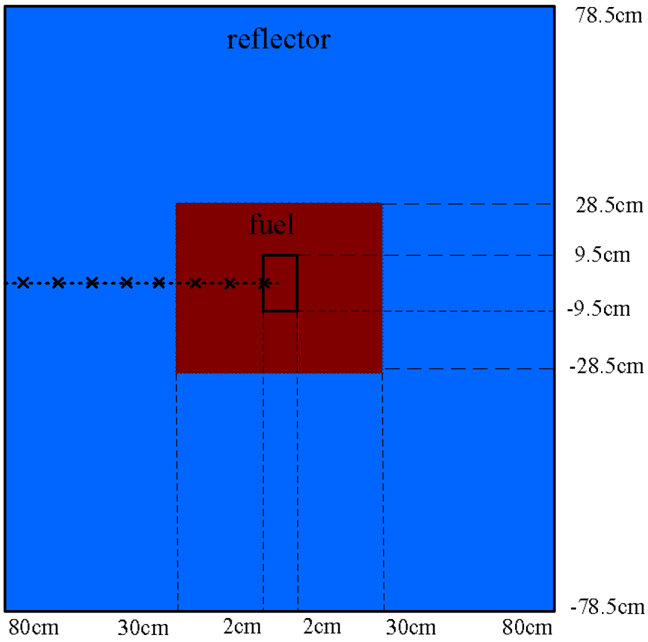

Figure 6.1: The geometry configuration of the thermal reactor.

assumed to be recorded at the midplane along the radius as shown in Figure 6.1.

6.1 Area-ratio method

6.1.1 FX2-TH code simulations

Due to the “stiffness” of the reactor system, it is not an easy task to directly simulate the time-dependent neutron flux subjected to the injection of external neutron pulses in a subcritical reactor. In addition, for the area-ratio method, the detector responses are recorded after thousands of repetitive neutron pulses are injected into the subcritical reactor to reach an equilibrium state. Therefore, the direct numerical simulations of thousands of neutrons pulses become even more difficult.

To obtain an accurate simulation of the detector responses, instead of simulating thousands of neutron pulses directly, we propose to calculate the delayed-neutron equilibrium conditions and to perform the simulation only for a single pulse starting with the calculated delayed-neutron equilibrium conditions. The delayed-neutron equilibrium conditions are the initial conditions of the time-dependent diffusion equations when the delayed-neutron background reaches an asymptotic level, as shown in Chapter IV. Mathematically, we can rewrite them down as

$$\phi_t(\mathbf{r}, E, 0^-) = \phi_d(\mathbf{r}, E, T^-), \quad C(\mathbf{r}, 0^-) = C(\mathbf{r}, T^-), \tag{6.1}$$

where the delayed neutron flux ϕ_d and and the precursor density function C are unknowns at $t = T^-$. Because the neutron pulse period T is rather small compared with the shortest half-life of the delayed-neutron precursors, ϕ_d and C can then be assumed as constants within the pulse period T and be well approximated by

$$\begin{aligned} \phi_t(\mathbf{r}, E, 0^-) &= \phi_d(\mathbf{r}, E, T^-) \simeq \frac{1}{T}\int_0^T \phi_d(\mathbf{r}, E, t)dt = \frac{1}{T}\left(\hat{\phi}_t - \hat{\phi}_p\right), & (6.2) \\ C(\mathbf{r}, 0^-) &\simeq \frac{1}{T}\int_0^T C(\mathbf{r}, t)dt = \frac{\beta}{T\lambda}\mathbf{F}\hat{\phi}_t, & (6.3) \end{aligned}$$

where $\hat{\phi}_t$ and $\hat{\phi}_p$ are time-integrated fluxes and can be obtained by solving Equations 4.7 and 4.8, respectively.

Thus, in our numerical simulations for the area-ratio method, we first solve the two steady-state fixed-source diffusion problems corresponding to Equations 4.7 and 4.8. The fixed external source has the same spatial and energetic distributions as the time-dependent pulsed-neutron source but are integrated over the pulse period T. The delayed neutrons are ignored by setting $\beta_{eff} = 0.0$ while solving for the time-integrated prompt flux $\hat{\phi}_p$. The delayed-neutron equilibrium state is then calculated from Equations 6.2 and 6.3. With the calculated delayed-neutron equilibrium conditions as the initial conditions, the time-dependent diffusion equations 2.12 and 2.13 are solved by the FX2-TH code for a single pulse. The detector responses are obtained from the time-dependent numerical simulations.

6.1.2 Validation of Bell's static spatial correction method

With the simulated detector responses, the area-ratio method yields the reactivities of the R-Z reactor at each detector position as shown in Figure 6.2 with the scale on the LHS ordinate. Compared with the reference reactivity, the area-ratio method overestimates the value of the reactivity by a maximum of 50% in the source region. As detectors move away from the external source region, the reactivities obtained from the area-ratio method gradually agree with the reference reactivity, but with a 7.5% underestimation of the subcriticality everywhere in the reflector.

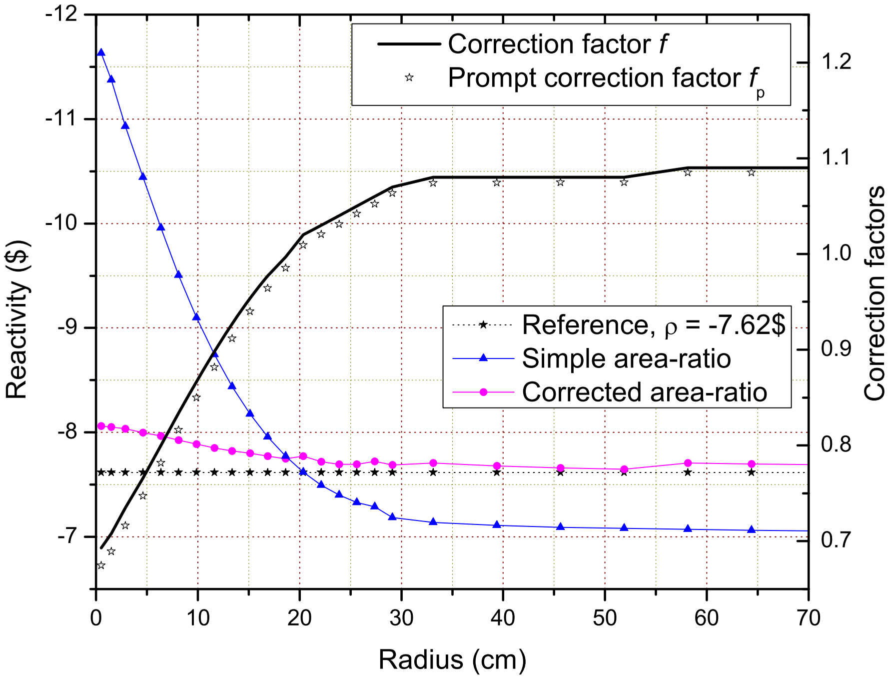

Figure 6.2: The reactivity and the spatial corrections of the area-ratio method for the thermal reactor with ^{235}U detectors at the middle plane in the R-direction.

Bell's spatial correction factor f can also be calculated, with the time-integrated fluxes $\hat{\phi}_t$ and $\hat{\phi}_p$ calculated by the FX2-TH code. Figure 6.2 shows the calculated f at each detector position with the scale on the RHS ordinate. The reactivities obtained from the area-ratio method are then corrected at each detector position with the spatial correction factor f. As shown in the figure, the reactivities after the spatial corrections are much less spatially dependent than those obtained from the area-ratio method alone, with a maximum deviation from the reference calculation is $< 6\%$ in the source region. The corrected reactivities obtained for the detectors in the reflector region are spatially independent and agree with the reference calculation within 1%. The relative large difference in regions close to the external is due to the numerical errors in the FX2-TH simulations. Specifically, in the pulsed-neutron experiment, the neutron pulse width is small and is localized in a small region. Thus, the detector responses rise very quickly for detectors close to the source region, and are difficult to simulate accurately with finite time steps.

In addition, the prompt spatial correction factor f_p can also be obtained based on Equation 4.37. As shown in Figure 6.2, f_p agrees with f everywhere in the reactor. It also indicates that the spatial effects in the area-ratio method are mainly induced by the prompt-neutron harmonics, and f_d is close to 1.0.

To understand why the area-ratio method overestimates the subcriticality of the reactor significantly in regions close to the external source, we compare the detector responses corresponding to $\hat{\phi}_p$ and $\phi_{0,k}$, respectively. In a subcritical reactor, the time-integrated prompt-neutron flux $\hat{\phi}_p$, which is the solution of Equation 4.7, usually peaks in regions close to the external source and falls off exponentially or like an exponential function in the spatial domain. However, the spatial distribution of the fundamental k-mode $\phi_{0,k}$ is flatter and like a cosine function. Therefore, as shown in Figure 6.3, $\hat{\phi}_p$ will be larger than $\phi_{0,k}$, and f_p will always be smaller than 1.0 in regions close to the external source, which explains why the area-ratio method always overestimates the subcriticality of the reactor in those regions.

Moreover, the neutron detectors are fission chambers with energy response functions similar to that of the fission operator $\mathbf{F}$ in Equation 4.38. Besides, $\mathbf{F}$ is zero outside the fuel region. Therefore, the equality in Equation 4.38 is only imposed on the fuel region. To satisfy this equality, there must exist a region in the fuel where $\hat{\phi}_p$ will be smaller than $\phi_{0,k}$. Consequently, the spatial correction factor f_p will be

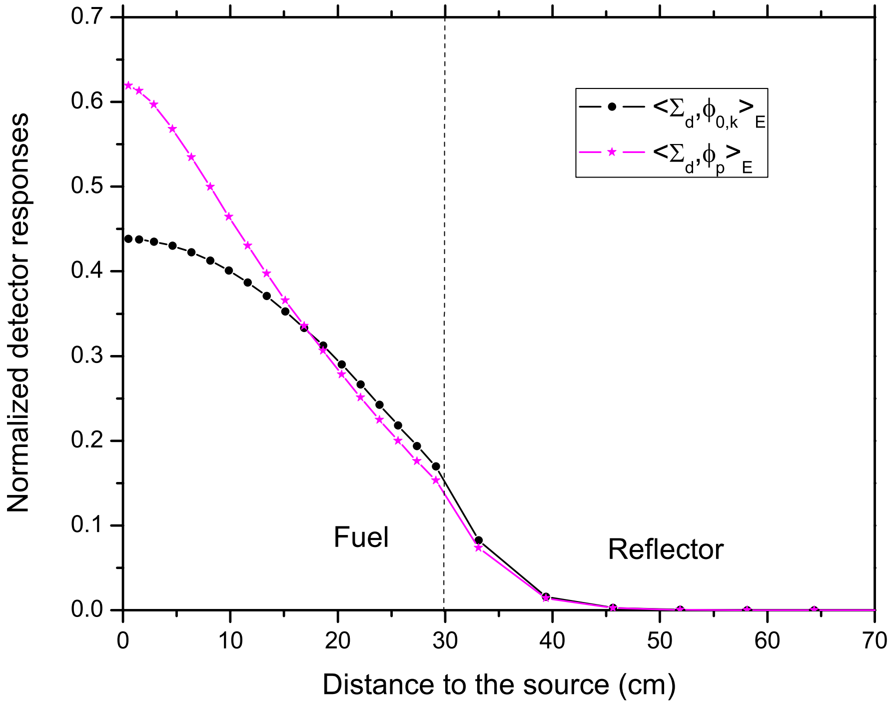

Figure 6.3: The comparison of the detector responses corresponding to the time-integrated prompt-neutron flux and the fundamental k-mode in the thermal reactor.

larger than 1.0, and the area-ratio method underestimates the subcriticality in this region, as indicated in Figure 6.2.

Overall, this numerical test verifies that the spatial effects of the simple area-ratio method are well compensated for by Bell's spatial correction factor f if accurate kinetics parameters β and ρ are used. This numerical test also shows that our prompt spatial correction factor f_p provides physically intuitive explanations of the spatial effects in the area-ratio method. Due to the different spatial distribution between $\hat{\phi}_p$ and $\phi_{0,k}$, f_p also predicts that the area-ratio method will always overestimate the subcriticality at positions close to the external source in the fuel region, and underestimate the subcriticality at position away from the source but in the fuel region. In a real pulsed-neutron experiment, the real reactivity of the subcritical reactor can then be bracketed by the measurements performed at these two positions.

6.1.3 Spatial effects in the extrapolated area-ratio method

The reactivity of a subcritical reactor can also be obtained from the simulated detector responses with the extrapolated area-ratio method as shown in Figure 6.4. For this numerical model, the extrapolated area-ratio method yields reactivities much less spatially dependent compared with the area-ratio method, with a maximum overestimation of the subcriticality by about 2% at the source region, and about 1.5% at the core-reflector interface.

To obtain the spatial correction factor $f_{p,e}$ and $f_{d,e}$, the fundamental prompt α-mode is calculated via IRAM. The correction factors are then obtained according to Equations 4.46 and 4.47 as shown in Figure 6.4 with the scale on the RHS ordinate. In this figure, the prompt correction factor $f_{p,e}$ is almost spatially flat both in the core and in the reflector region, except at the core-reflector interface, where the spatial correction is larger than 1%. This compensates for the underestimation of the subcriticality by the extrapolated area-ratio method at the core-reflector interface very well. The spatial correction factor $f_{d,e}$ corresponding to the delayed-neutron harmonics has the largest value in the source region with a maximum spatial correction of 3%. Overall, the reactivity obtained from the extrapolated area-ratio method after the spatial corrections agrees with the reference reactivity of -7.62 \$ within 0.5% everywhere along the radius.

The spatial dependence of the extrapolated area-ratio method is mainly related to the “kinetics distortions” factor, unlike the spatial dependence in the area-ratio method. In this particular numerical model, the extrapolated area-ratio method is much less spatially-dependent than the simple area-ratio method due to the weak “kinetics distortions”. Namely, as shown in Appendix C, the neutron removal cross sections in the reflector region are not significantly different from those in the fuel

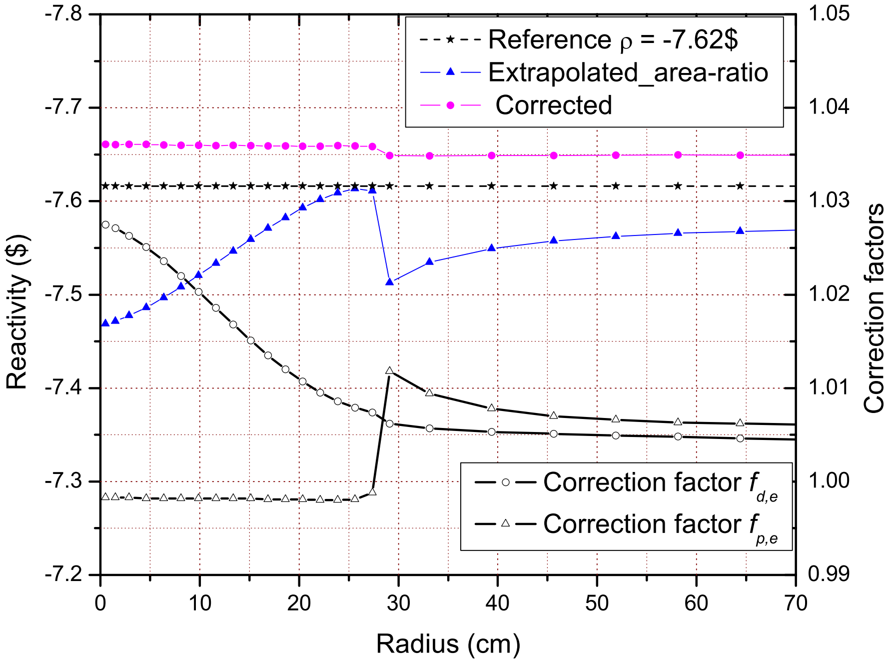

Figure 6.4: The spatial corrections of the extrapolated area-ratio method in the thermal reactor with ^{235}U detectors at the middle plane in the R-direction.

region. Thus, neutrons, especially thermal neutrons, will not accumulate in either of the regions. In addition, with this numerical model, the spatial correction factor $f_{p,e}$ and $f_{d,e}$ are demonstrated to be capable of compensating for the spatial effects in the extrapolated area-ratio method induced by both the prompt-neutron harmonics and delayed-neutron harmonics.

6.1.4 Modal analysis of the area-ratio method

In this numerical model, the area-ratio method shows large spatial effects. However, the "kinetics distortion" factor, which is the fundamental modal term of f, is almost spatially independent as shown in the extrapolate area-ratio method. Thus, in order to investigate the role of the high-order prompt-neutron harmonics in the area-ratio method, we calculate the spatial correction factor f_p with different numbers of prompt-harmonics modes included.

First, the prompt α-modes $\phi_{m,p}$ are obtained via IRAM for this R-Z thermal reactor. The detector responses corresponding to the prompt α-modes are shown in Figure 6.5, where only the fundamental and first harmonics in R-direction are included. The direct and adjoint k-modes are also calculated via IRAM. The prompt spatial correction factor f_p with M prompt α-modes included can then be obtained based on Equation 4.33:

$$f_{p,M} \quad = \quad \left[\frac{\displaystyle\sum_{m=0}^{m=M} \frac{A_m(0)}{\alpha_m} \frac{\left\langle \phi_{0,k}^{+}, \chi_d \beta \mathbf{F} \phi_{m,p} \right\rangle_{\mathbf{r},E}}{\left\langle \phi_{0,k}^{+}, \chi_d \beta \mathbf{F} \phi_{0,k} \right\rangle_{\mathbf{r},E}}}{\displaystyle\sum_{m=0}^{m=M} \frac{A_m(0)}{\alpha_m} \frac{\left\langle \Sigma_d, \phi_{m,p} \right\rangle_E}{\left\langle \Sigma_d, \phi_{0,k} \right\rangle_E}} \right]. \tag{6.4}$$

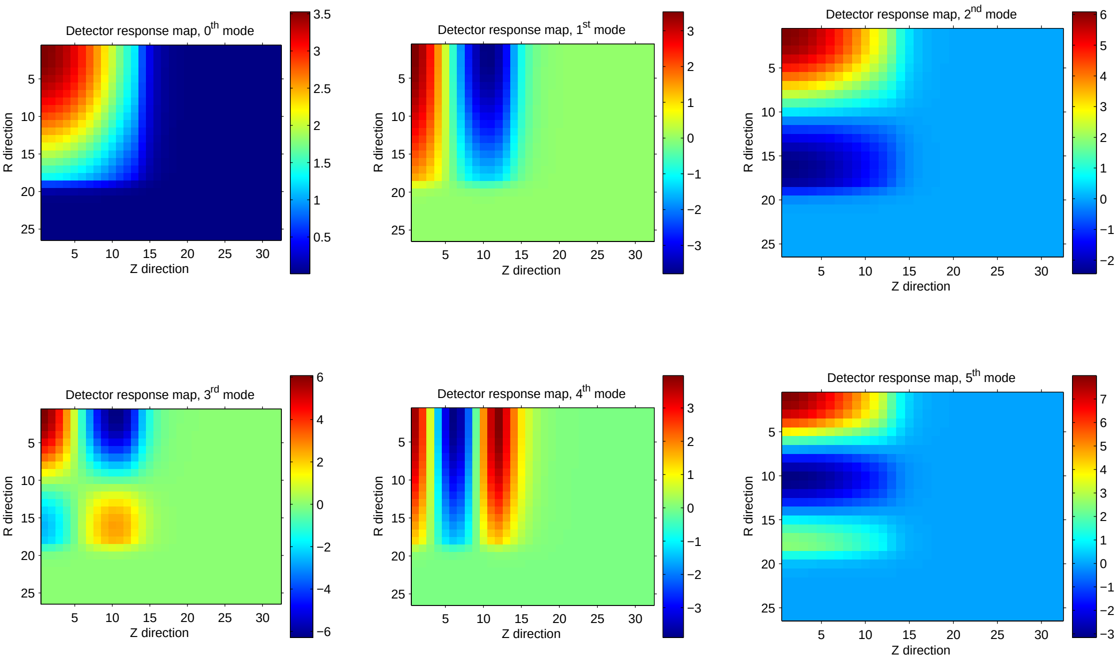

Figure 6.5: The first six ^{235}U detector response maps $\langle \Sigma_d, \phi_m^{\alpha} \rangle_E$ in the thermal reactor.

In addition, we also calculate the prompt spatial correction factors $f_{p,e}$ and f_p based on Equations 4.46 and 4.37, respectively. Figure 6.6 compares the spatial correction factors $f_{p,M}$ with f_p, where M is the modal expansion order. If only the fundamental prompt α-mode is included ($M = 0$), the spatial correction factor $f_{p,0}$ is almost flat and very similar to $f_{p,e}$, which indicates that the spatial variations in the area-ratio method due to the "kinetics distortion" are small. If the first harmonics in the R-direction is included ($M = 2$), due to the significant difference between the first prompt α-mode and the fundamental k-mode in the R-directions, $f_{p,2}$ becomes strongly spatially dependence as shown in the figure. With more modes included ($M = 5$), the spatial correction factor $f_{p,5}$ agrees with f_p better than $f_{p,2}$. However, a very large number of expansion modes would be required for $f_{p,M}$ to closely agree with f_p.

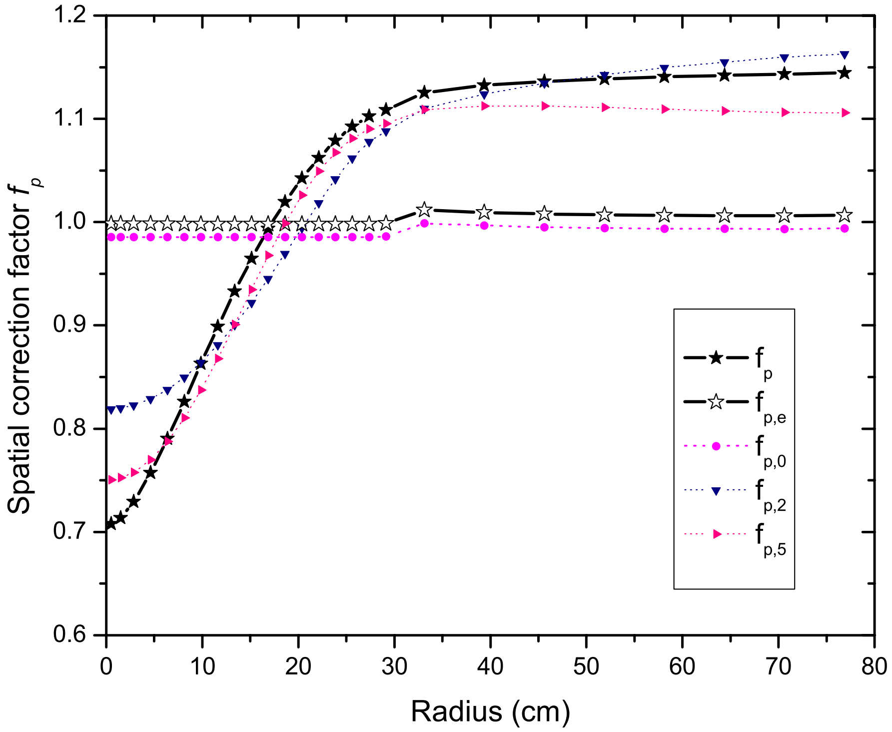

Figure 6.6: The prompt spatial correction factors for the ^{235}U detector in the thermal reactor.

Thus, this numerical tests showed that the high-order prompt α-modes have great impacts on the spatial effects in the area-ratio method, and it cannot be neglected when calculating the prompt spatial correction factor f_p [23].

6.2 α-method

6.2.1 FX2-TH code simulations

Compared with the area-ratio method, the numerical simulations of the pulsed-neutron experiment for the α-method are much easier because the detector responses are recorded after a single neutron pulse injected into the system. The time-dependent diffusion equations are solved directly by the FX2-TH code for the same R-Z reactor as shown in Figure 6.1. The ^{235}U detectors are placed at the same radial positions as in the area-ratio method.

To obtain the reactivity, the detector responses are fitted by an exponential function in the prompt decay region from $t = 1$ ms to $t = 2.5$ ms. As an example, Figure 6.7 shows the exponential fitting at $r = 18$ cm in the fuel region. The decay constants obtained from the detector responses are all about $\alpha = -3348$ s^{-1}. If the kinetics parameters Λ and β_{eff} are provided, the reactivity of the thermal reactor can then be estimated based on Equation 3.16.

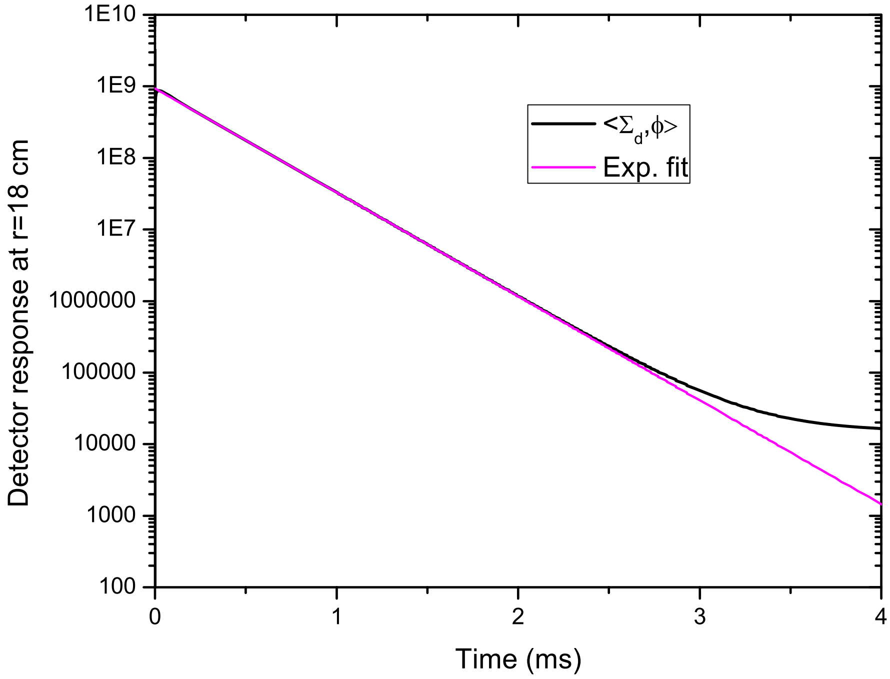

Figure 6.7: The exponential fitting of the detector response at $r = 18$ cm in the thermal reactor.

For the traditional α-method, Λ and β_{eff} are usually measured in a close-to-critical reference configuration, which is very similar to the subcritical reactor in material compositions and geometry configurations. In this numerical simulation, we choose to vary the height of the fuel region of the R-Z reactor to 104.5 cm to achieve $k_{eff} = 0.9966$. With this close-to-critical reference model, we obtain $\beta_{ref} = 0.00721$, and $\Lambda_{ref} = 17.6\ \mu$s. Another way to achieve criticality is to adjust the fission cross sections. With the same k_{eff}, we obtain $\Lambda_{ref} = 17.5\ \mu$s, which is very close to the value by varying the core height. Thus, the reactivity of the R-Z reactor can be calculated with the decay constant α_0 obtained at each detector position through Equation 3.16, as shown in Figure 6.8.

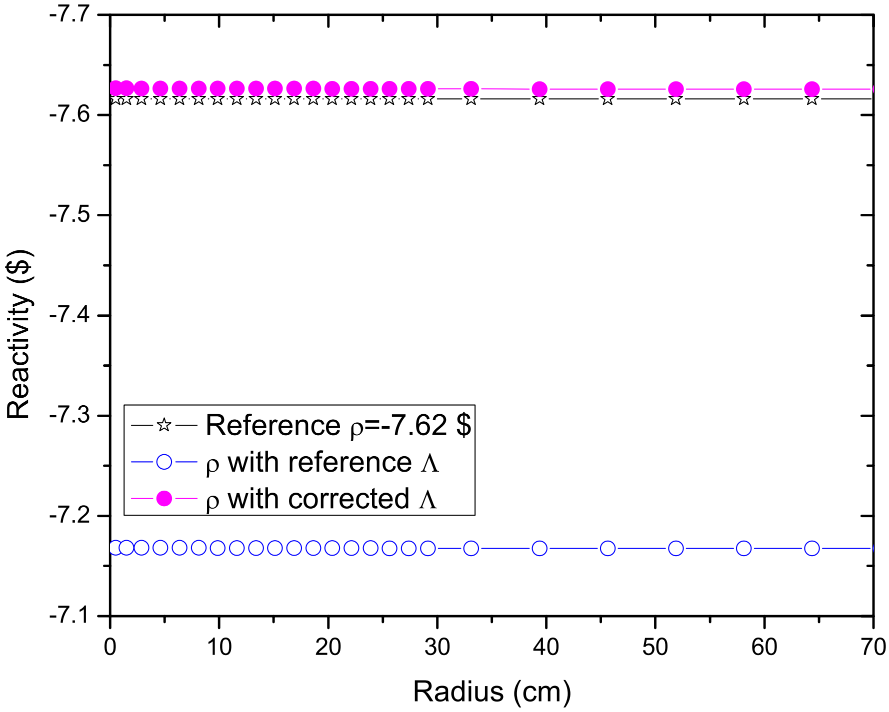

Figure 6.8: The reactivity and the space-time corrections of the simple α-method for the thermal reactor with ^{235}U detectors at the middle plane in the R-direction.

Unlike the area-ratio method, the reactivities estimated from the α-method are spatially independent for this numerical model, because the decay constants obtained from the detector responses are uniform. However, compared with the reference reactivity $\rho = -7.62$ \$, the α-method underestimates the subcriticalitiy of the R-Z reactor about by 6% everywhere in the reactor. This is mainly due to the approximations in the kinetics parameters, especially the mean generation time Λ. In the next section, we will study the variation of the mean generation time in a subcritical reactor at different subcriticalities.

6.2.2 Space-time effects in the α-method

The mean generation time varies for reactors at different subcritical levels. In our numerical model, by varying the height of the reactor fuels, the reactor k_{eff} changes from 0.92 to 0.997, and Λ continuously decreases about 8%, as shown in Figure 6.9.

Usually, in a pulsed-neutron experiment, the reactor is made to be subcritical from the reference configuration by adjusting cross sections, e.g., inserting control rods, or removing fuel plates out of the reactor. As defined in Equation 4.55, the mean generation time Λ is inversely proportional to the number of fission neutrons generated from the fission, i.e., the $\chi\mathbf{F}\phi_{0,p}$ term in 4.55. For a nuclear reactor, if k_{eff} of the reactor decreases, the total number of fission neutrons generated by fission usually decreases correspondingly. Therefore, Λ increases proportionally as shown in Figure 6.9.

The property that Λ increases as k_{eff} decreases for a subcritical reactor, especially for a small reactor with a large reflector, was also investigated by Perdu [50]. In his Monte Carlo simulations, he captured the reactor at a moment t after the neutron pulse is turned off. Then he counted the number of neutrons from different generations in the reactors with $k_{eff} = 0.9$ and $k_{eff} = 1.0$ respectively, and observed that the fraction of the neutrons born in early generations is larger in the subcritical reactor than in the critical reactor. This is due to the fact that in the subcritical reactor, fewer neutrons are born in the recent generations because of the smaller mul-

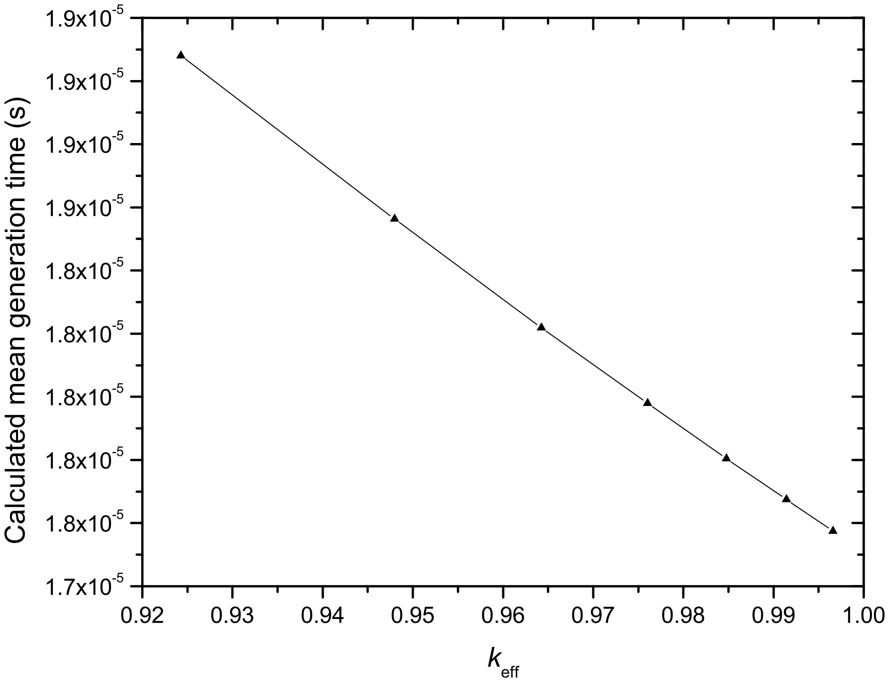

Figure 6.9: The mean generation time Λ of the thermal reactor at different configurations.

tiplication factor. Neutrons from the old generations are long-lived. Because Λ is an average value of the neutron life-time in a reactor, Λ then is larger in a subcritical reactor than in the reference close-to-critical reactor.

In our numerical model, in order to obtain an accurate estimation of the mean generation time Λ for a subcritical reactor, we first calculate the mean generation correction factor from the numerical simulations. IRAM is utilized to calculate both the fundamental k-mode $\phi_{0,k}^{+}$ and the prompt α-mode $\phi_{0,p}$ of the reactor at the reference configuration and at the subcritical configuration. The calculated fundamental prompt α-eigenvalue for the subcritical configuration is -3345 s^{-1} which agrees with the fitted value of $\alpha_0 = -3348$ s^{-1} very well. According to Equation 4.66, the correction factor f_{Λ}^{cal} is calculated to be 1.056. The reactivities of the R-Z reactor with the corrected Λ are then obtained as shown as in Figure 6.8, which indicates a very good agreement between the corrected reactivities and the reference reactivity.

6.2.3 Modal analysis of the α-method

In addition to the difficulty of accurately determining Λ in actual applications of the α-method, we note in general that it may also be difficult to obtain spatially-independent decay constants in a pulsed-neutron experiment. In this numerical model, the decay constants obtained from the simulated detector responses at different positions are coherent, because the high-order modal terms decrease quickly.

Specifically, Figure 6.10 shows the modal expansions of the detector responses at $r = 8$ cm and $r = 18$ cm, respectively. The modal expansion fluxes are calculated according to Equation 5.56 with the fundamental term only, i.e. $N = 1$, or with the first 16 modal terms, i.e., $N = 16$. As shown in the figure, the modal expansion flux with 16 modes included decays away quickly during the first 100 μs, leaving a tail which agrees with the fundamental term and decays away in a purely exponential manner at both positions. In addition, after about 100 μs the detector responses obtained from the direct FX2-TH simulations closely agree with the one-term expansion. Therefore, the decay constants obtained from different positions after $t = 100$ μs are spatially independent, and are equal to the fundamental prompt α-eigenvalue α_0.

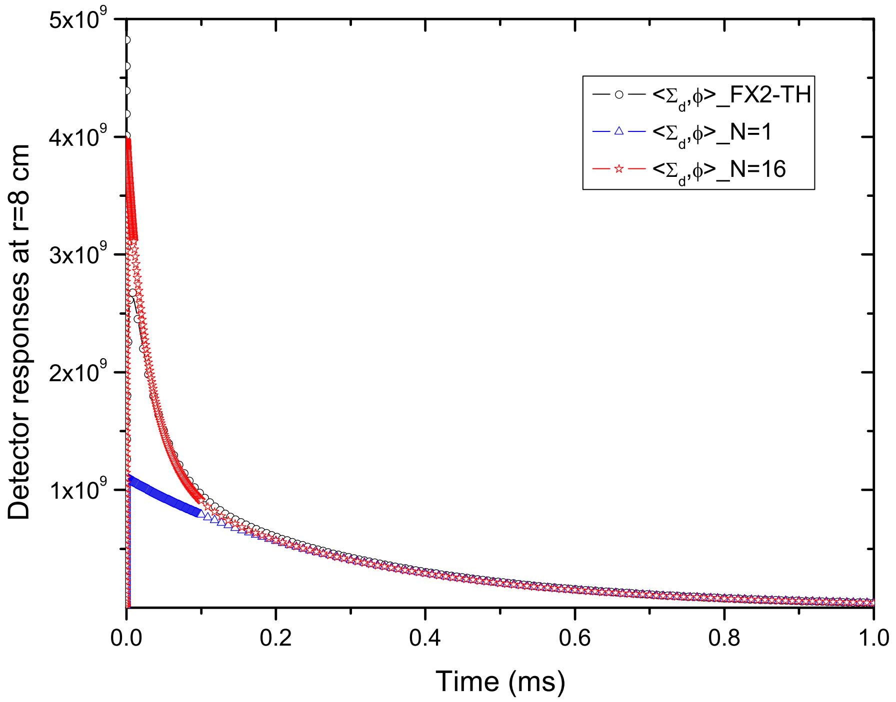

(a) at $r = 8$ cm

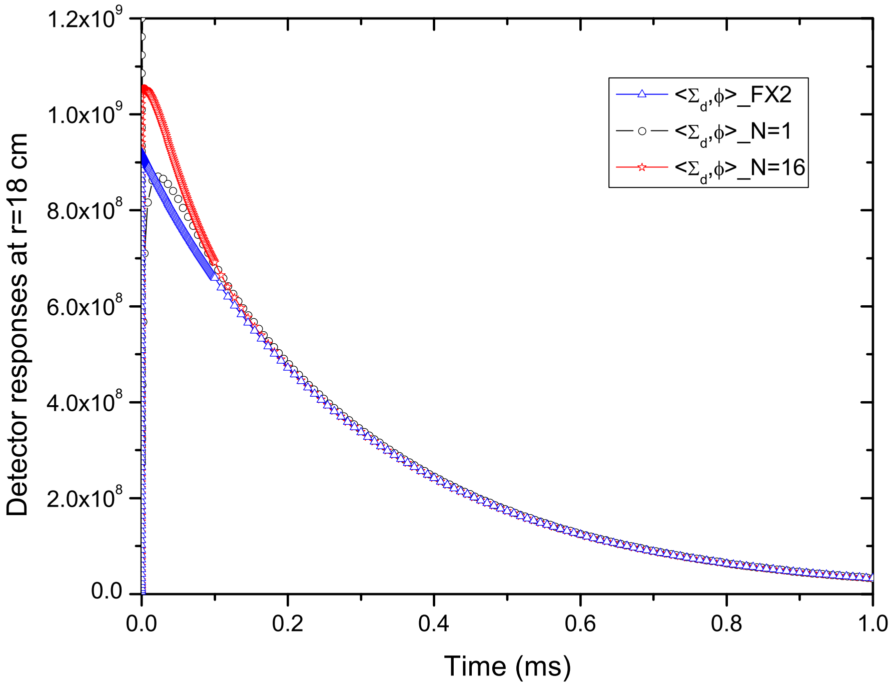

(b) at $r = 18$ cm

Figure 6.10: The modal expansions of the detector responses with expansion order $N = 1$ and $N = 16$ at (a) at $r = 8$ cm and (b) at $r = 18$ cm .

CHAPTER VII

The Space-Time Corrections in the MUSE-4 Subcritical Reactor

7.1 Numerical models of the MUSE-4 experiment for the area-ratio method

To analyze the spatial effects in the MUSE-4 pulsed-neutron experiments, we first set up a 33-group XYZ-geometry model for the MUSE-4 SC0 reactor. Figure 7.1 shows the core layout of the simulation model for the MUSE-SC0 subcritical reactor with one shim rod (or control rod) SR1 inserted into the reactor. The pilot rod (PR) can also be inserted into the reactor to adjust the reactivity. Because it is a small perturbation to the system, we do not simulate the PR in our numerical model. The locations of the fission chamber detectors are marked by their names in the core layout.

The materials in each region as shown in the core layout are homogenized and their macroscopic cross sections are calculated by the ECCO module of the ERANOS code package [29]. The JEF2.2 library is applied in the ECCO code. The VARIANT nodal diffusion calculation gives $k_{eff} = 0.9641$ for the subcritical case with SR1 in the reactor and $k_{eff} = 1.0017$ for the close-to-critical case with no SR rod inserted into the reactor. The time-dependent diffusion simulations for the pulsed neutron experiments are performed with the KIN3D module for the subcritical con-

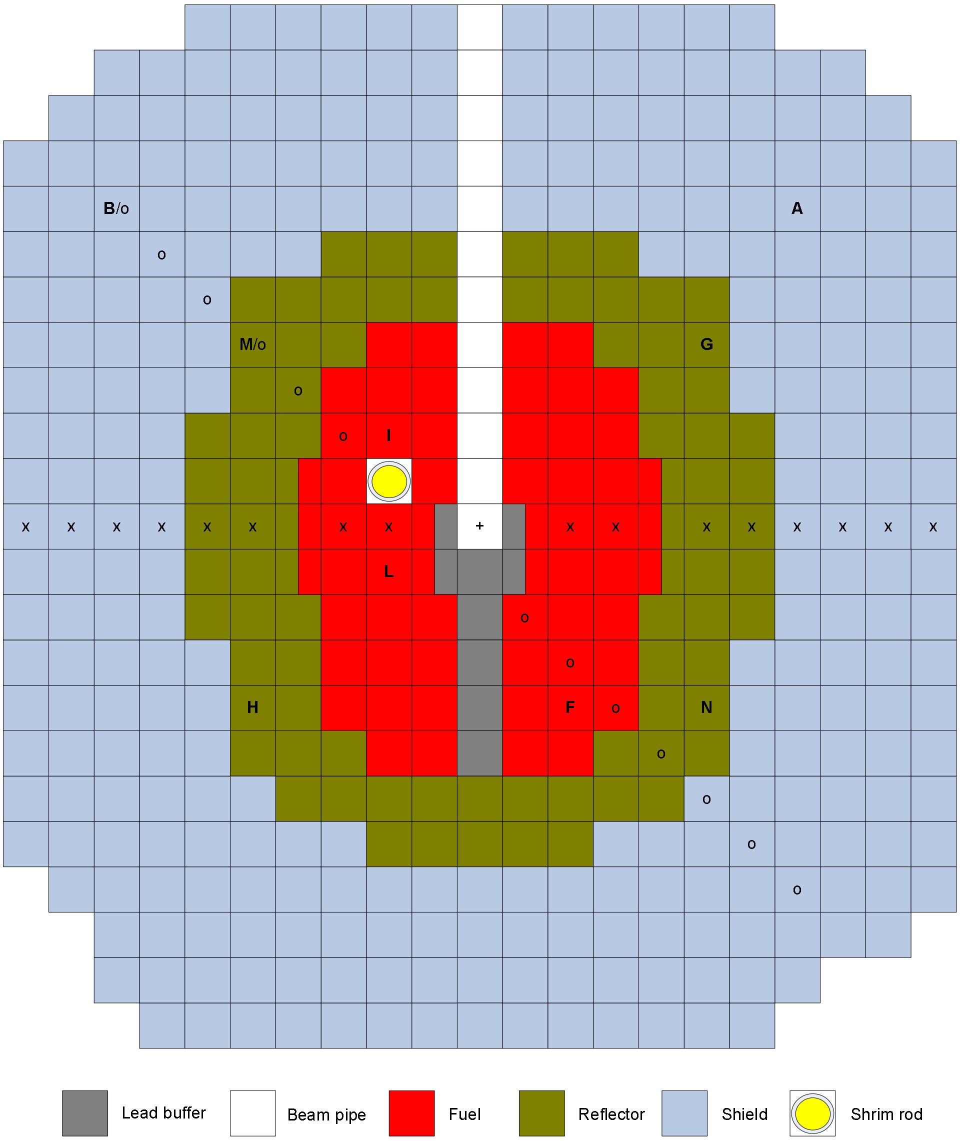

Figure 7.1: The core layout of the MCNP model for the MUSE-4 SC0 reactor and the location map of the ^{235}U detectors in the reactor.

figuration. We also set up a MCNP model to tally 33-group response functions for the ^{235}U detectors using the ENDF/B-VI library. The Monte Carlo KCODE calculation gives $k_{eff} = 1.007 \pm 0.00014$ for the close-to-critical configuration and $k_{eff} = 0.9638 \pm 0.0003$ for the subcritical configuration. The k-eigenvalues obtained from the numerical simulations are compared with the experimental data in Table 7.1, where we note that the ERANOS deterministic calculations agree reasonably

Table 7.1: The calculated k_{eff} and the experimental data for the MUSE-4 SC0 close-to-critical and subcritical configurations.

Configurations	Experiment	MCNP5	ERANOS
Close-to-critical	0.99920 ± 0.0001	1.007 ± 0.00014	1.0017
Subcritical	$\cdots$	0.9638 ± 0.0003	0.9641

well with the Monte Carlo simulations.

7.2 The area-ratio method of the MUSE-4 experiment

In the MUSE-4 project, pulsed-neutron experiments were performed in the subcritical reactor with several different configurations as discussed in Section 1.3. The SC0 without control rods, and the SC2 and the SC3 configurations are all X-Y symmetric. Figure 7.1 illustrates an asymmetric configuration of SC0 because the SR1 is inserted into the top-left quadrant of the reactor. The area-ratio method was applied carefully on the experimental data to obtain reactivities for each reactor configurations in Villamarin's PhD thesis [15]. Here we summarize his results in Table 7.2.

Table 7.2: Reactivities ($) obtained from the area-ratio method with the ^{235}U detectors for different configurations in the MUSE-4 project.

Detector	SC0	SC0	SC2	SC3
	4SR ↑ PR ↓	3SR↑ SR$_1$↓ PR ↓	4SR ↑ PR ↓	4SR ↑ PR ↓
F	-1.98 ± 0.01	−11.82 ± 0.02	-9.05 ± 0.02	-13.53 ± 0.02
I	-2.00 ± 0.01	−14.07 ± 0.02	-9.25 ± 0.02	-14.76 ± 0.02
L	-2.00 ± 0.01	-12.83 ± 0.02	-9.41 ± 0.02	-14.65 ± 0.02
G	-2.02 ± 0.01	-12.82 ± 0.02	-9.54 ± 0.02	-14.81 ± 0.02
H	-2.00 ± 0.01	-12.96 ± 0.02	-9.38 ± 0.02	-14.18 ± 0.02
M/C	-2.00 ± 0.01	-12.68 ± 0.02	-9.12 ± 0.02	-14.31 ± 0.02
N/D	-1.99 ± 0.01	-12.06 ± 0.02	-9.34 ± 0.02	-13.88 ± 0.02
A	-2.01 ± 0.01	-12.57 ± 0.02	-9.41 ± 0.02	-14.40 ± 0.02
B	-2.01 ± 0.01	-12.71 ± 0.02	-9.37 ± 0.02	-14.42 ± 0.02
Average	-2.001 ± 0.004	-12.55 ± 0.06	-9.32 ± 0.05	-14.33 ± 0.05

As shown in the second column of the table, the spatial dependence is very small for the SC0 close-to-critical configuration. However, as shown in the third column of the table, the difference between the reactivities obtained from detector F and detector I is > 2 \$ in the SC0 subcritical configuration. The spatial dependence is also significant in the SC3 configuration where the reactor is more subcritical. Moreover, from the table, a spatial pattern can also be found from the measured reactivities. Specifically, for all the configurations, the reactivity obtained from detector F is always smaller than the averaged value of the reactivities, while the reactivity obtained from core detector I or L is always larger than the average. Because there are large spatial variations in the SC0 subcritical configuration, our spatial analysis focuses on analyzing the spatial effects in this configuration. Spatial correction factors will be calculated from the numerical simulations with the ERANOS determinstic model or the MCNP model.

7.2.1 Diffusion simulations of the MUSE-4 experiment for the area-ratio method

In order to calculate spatial correction factors from the numerical simulations, we start with the 3-D ERANOS diffusion model. The time-integrated flux $\hat{\phi}_p$ and $\hat{\phi}_t$ are calculated with the VARIANT module of the ERANOS code package. The spatial correction factors for ^{235}U detectors are obtained via Equation 4.15, and are listed as f^{DIF} in Table 7.3. The reactivities after spatial corrections are also listed as ρ^{DIF} in the table. The experimental data ρ^{exp} is the same as the third column in Table 7.2. Apparently, the spatial variations of ρ^{exp} can not be compensated for by the correction factor f^{DIF}. Especially, ρ^{DIF} obtained from detector F and detector I still differ from each other by about 2\$.

7.2.2 Transport simulations of the MUSE-4 experiment for the area-ratio method

The diffusion theory approximation is not very accurate to describe the flux variations in the reactor, especially for regions around control rods. A transport theory

Table 7.3: Spatial correction factors and the reactivities of the area-ratio method for ^{235}U detectors in the MUSE-4 SC0 configuration with SR1 down phase.

Detector	ρ^{exp}($)	f^{DIF}	ρ^{DIF}($)	f_p^{MCNP}	$\sigma(\%)$	ρ^{MCNP}($)	ρ^{BISTRO}($)
F	-11.82 ± 0.02	0.923	-10.91	1.044	0.380	-12.34	-11.8
I	-14.07 ± 0.02	0.913	-12.84	0.917	0.412	-12.90	-13.1
L	-12.83 ± 0.02	0.868	-11.14	0.932	0.342	-11.96	-13.0
G	-12.82 ± 0.02	0.941	-12.06	0.947	0.870	-12.15	-12.4
H	-12.96 ± 0.02	0.915	-11.85	1.003	0.772	-13.00	-12.1
M	-12.68 ± 0.02	0.926	-11.74	0.926	1.004	-11.74	-12.8
N	-12.06 ± 0.02	0.923	-11.14	1.018	0.743	-12.28	-11.8
A	-12.52 ± 0.02	0.941	-11.78	0.994	4.081	-12.43	-12.4
B	-12.71 ± 0.02	0.925	-11.76	0.935	5.318	-11.88	-13.0
Average ($)	-12.72 ± 0.006	⋯	-11.69	⋯	⋯	-12.30	-12.47

calculation using the BISTRO module in the ERANOS code package [51] was performed by Carta, et al. [16]. In his transport calculations, the 33-group homogenized cross sections are also obtained via the ECCO code with the JEF2.2 library. The prompt-neutron area and the delayed-neutron area are obtained by solving the two fixed-source transport problems in Equations 4.9 and 4.10. Reactivities are then calculated as the negative ratio of prompt-neutron area and the delayed-neutron area, and are listed as ρ^{BISTRO} in Table 7.3. Overall, the BISTRO transport calculation generates reactivities close to the measurements at most of the detector positions except at detector I, where the largest spatial variation occurs.

In order to obtain a set of spatial correction factors which can reduce the spatial effects in the experimental data, a more accurate transport model other than the 2-D BISTRO model is required. The Monte Carlo method is a perfect tool to solve a steady-state 3-D transport problem, despite the demand of a long computational time to achieve a reasonably small statistical error. The MCNP5 code is a powerful Monte Carlo software to represent neutron transport in a nuclear reactor [52], and can be easily used to calculate detector responses, yielding, e.g., $\left\langle \Sigma_d, \hat{\phi}_p \right\rangle$ and

$\left\langle \Sigma_d, \hat{\phi}_t \right\rangle$. However, in order to calculate Bell's spatial correction factor f, the effective delayed neutron fraction β has to be calculated first. This additional calculation requires more complicated tallies. As we have demonstrated in our numerical test in Figure 6.2, most of the spatial variations in the area-ratio method are induced by the prompt-neutron harmonics. Therefore, we will calculate the prompt correction factor f_p, which only tallies the prompt neutrons, and is easier to obtain with the MCNP5 code.

For notational convenience, we rewrite Equation 4.37 for the prompt spatial correction factor f_p as

$$f_p(\mathbf{r}_D) \quad = \quad \left[\frac{\left\langle \phi_{0,k}^{+}, \chi_d \beta \mathbf{F} \hat{\phi}_p \right\rangle_{\mathbf{r},E}}{\left\langle \phi_{0,k}^{+}, \chi_d \beta \mathbf{F} \phi_{0,k} \right\rangle_{\mathbf{r},E}} \cdot \frac{\left\langle \Sigma_d, \phi_{0,k} \right\rangle_E}{\left\langle \Sigma_d, \hat{\phi}_p \right\rangle_E} \right]. \tag{7.1}$$

With the MCNP5 code, the adjoint fundamental mode can only be calculated by a multi-group scheme, and the available multi-group data library is collapsed from the ENDF/B-V library. However, the ENDF/B-VI library is the primary library for all the nuclides in direct Monte Carlo simulations, and the delayed fission neutron data are included in the ENDF6DN library for all the fissionable nuclides. Thus, there is inevitable modeling error due to the multi-group calculations of the adjoint flux using different neutron data libraries. On the other hand, the calculated f_p will not be too sensitive to the modeling error due to the fact that the adjoint flux is included both in the denominator and numerator of Equation 7.1 to calculate f_p. Thus, in our calculation, the multi-group adjoint flux is obtained from the 33-group diffusion calculation. Then, the inner product $\left\langle \phi_0^{+}, \chi_d \beta \mathbf{F} \hat{\phi}_p \right\rangle_{\mathbf{r},E}$ in Equation 7.1 can be calculated as

$$\left\langle \phi_0^{+}, \chi_d \beta \mathbf{F} \hat{\phi}_p \right\rangle_{\mathbf{r},E} = \left\langle \sum_g \chi_{d,g} \beta \phi_{0,k,g}^{+}, \sum_{g'} \nu \Sigma_{f,g'} \hat{\phi}_{g',p} \right\rangle_{\mathbf{r}}, \tag{7.2}$$

where the $\chi_{d,g}\beta\phi^{+}_{0,k,g}$ term is obtained from the 33-group ERANOS diffusion calculation. Likewise, the inner product $\left\langle \phi_0^{+}, \chi_d \beta \mathbf{F} \phi_{0,k} \right\rangle_{\mathbf{r},E}$ can also be obtained. A uniform weight function instead of the fundamental adjoint flux was also applied to test the sensitivity of f_p to the modeling error. It was found that f_p calculated with uniform weight function only differs by $< 5\%$ from that with the adjoint fundamental flux as the weight function. Thus, the calculated spatial correction factor is indeed not very sensitive to the modeling error of the adjoint flux.

The calculated spatial correction factor f_p from the MCNP simulations is listed as f_p^{MCNP} in Table 7.3, and the corresponding standard deviation in percentage is listed as σ in the same table. The reactivity in dollars after the spatial correction is also included in Table 7.3 as ρ^{MCNP}. With Monte Carlo simulations, the large spatial variation between detector I and detector F is well compensated for by f_p^{MCNP}. The reactivities after the spatial corrections are coherent, with a maximum difference of 6% at detector H from the averaged value. Because in our Monte Carlo model, all the special tubes, vertical channels are ignored for simplicity, a more detailed model, which represents more accurate geometry, is expected to help reduce the remaining spatial variation in the corrected experimental data, especially at detector position H.

7.2.3 Analysis of the spatial pattern in the MUSE-4 experiments

As demonstrated in the above section, the spatial effects in the MUSE-4 area-ratio data can be well compensated for by the prompt correction factor f_p. Thus, the spatial effects in the MUSE-4 area-ratio experimental data can be studied by examining the spatial dependence of f_p. Figure 7.2 shows the spatial correction factors f_p calculated for a ^{235}U detector placed in regions horizontally or diagonally across the MUSE-4 SC0 reactor. The horizontal regions are marked with “×” in

Figure 7.1, and the diagonal regions are marked with "○" in the same figure.

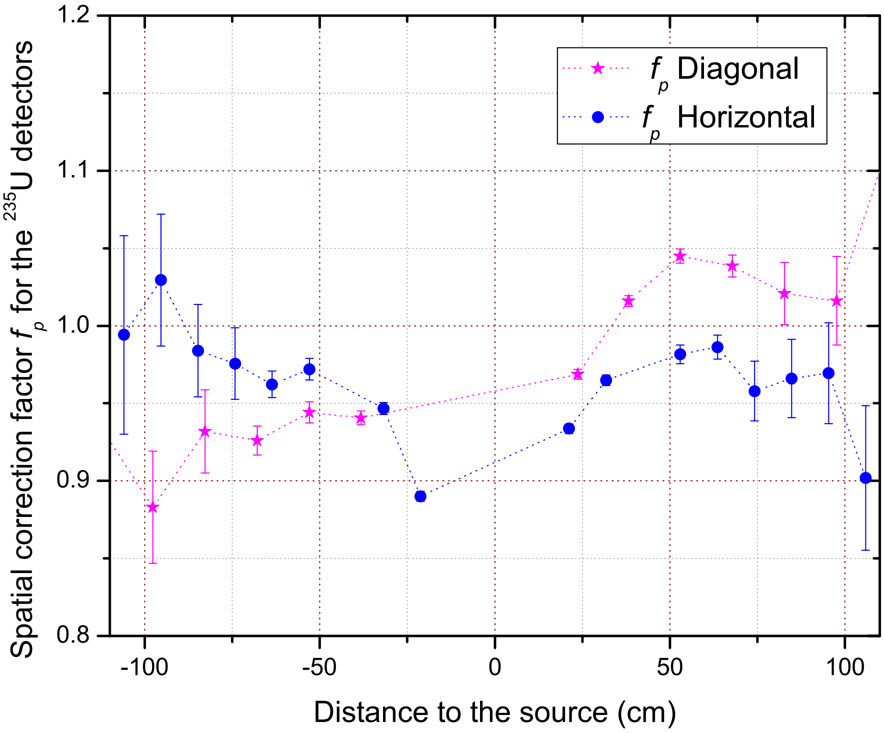

Figure 7.2: The spatial correction factors for ^{235}U detectors horizontally or diagonally crossing the MUSE-4 SC0 reactor.

As shown in Figure 7.2, when the detectors are close to the external source region, f_p deviates from 1.0 and less than 1.0, which indicates that the simple area-ratio method overestimates the value of the reactivity at regions close to the external source. The spatial correction factor curve gradually becomes flat away from the external source region. In addition, f_p is also sensitive to local variations, e.g., the presence of a control rod. In the MUSE-SC0 subcritical configuration, the control rod SR1 is placed in the top-left quadrant in Figure 7.1, and the diagonal regions are across the reactor from the top-left quadrant to the bottom-right quadrant. From Figure 7.2, we can find that the correction factor f_p is always smaller than 1.0 in the top-left quadrant and larger than 1.0 in the bottom-right quadrant. These parametric results are consistent with the experimental results. Namely, for the

MUSE-4 SC0 configuration, as shown in Table 7.2, detectors F, and N in the bottom-right quadrant give smaller values of the reactivity than detectors I, M and B in the top-left quadrant.

According to Equation 7.1, the spatial dependence of f_p is dependent on the relative difference between the normalized detector responses $\left\langle \Sigma_d, \hat{\phi}_p \right\rangle_E$ and $\langle \Sigma_d, \phi_{0,k} \rangle_E$. Thus, the spatial distribution of f_p is not only determined by the difference between the time-integrated prompt flux $\hat{\phi}_p$ and the fundamental k-mode $\phi_{0,k}$ at each detector position, but also on the detector's energy response function. However, if detectors are located at the same region in the subcritical reactor, e.g., detectors F and I both in the fuel region, their neutron spectra are similar. Figure 7.3 shows the energy distributions of the detector responses $\langle \Sigma_d, \phi_{0,k} \rangle_E$ tallied with 33 energy groups by the MCNP5 simulation for detector F in the fuel, detector N in the reflector and detector A in the shield region, respectively. For detectors in the fuel region, although the ^{235}U detector has large reaction cross sections at the low energy range, most of the neutrons detected in the fuel region are still high-energy neutrons. For instance, the detector response at detector F peaks at the very high energy range from 0.01 MeV to 10 MeV. The peak of the ^{235}U detector response is broadened and shifted to the low energy end for detectors moved out in the reflector and in shield region.

Thus, for detectors in the fuel region, the spatial distribution of f_p is determined by the relative difference between the neutron fluxes $\hat{\phi}_p$ and $\phi_{0,k}$ at the high energy region. To evaluate f_p obtained for detector F and I, we compare $\hat{\phi}_p$ with $\phi_{0,k}$ at these two positions within each energy group, as shown in Figure 7.4. Indeed, for both detectors, detector responses peak at the high energy range [0.01, 10] MeV, with $\hat{\phi}_p$ relatively higher than $\phi_{0,k}$ at position F, but lower at position I. As a result, f_p is larger than 1.0 at detector position F and smaller than 1.0 at detector position

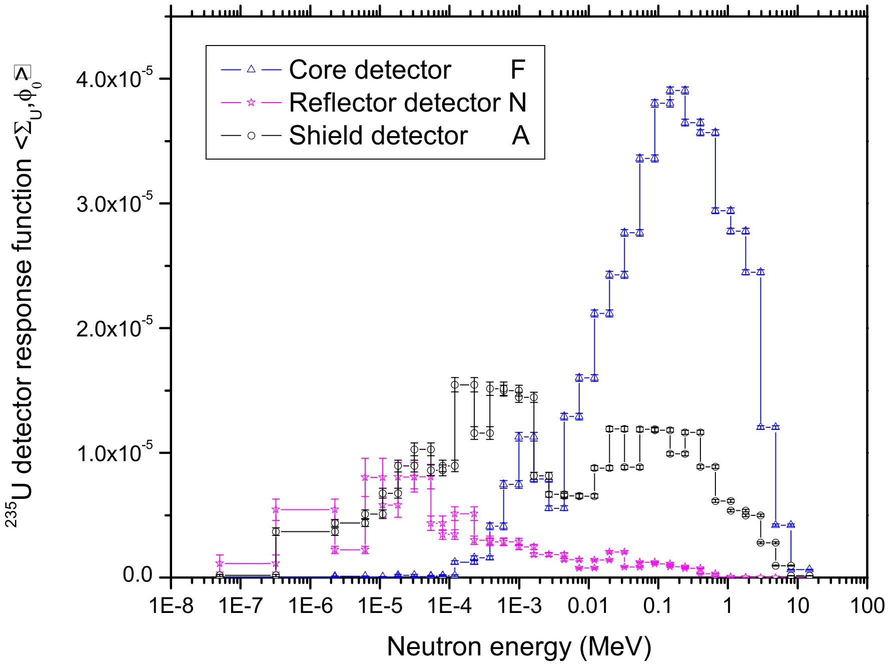

Figure 7.3: ^{235}U detector responses at different positions in the MUSE-4 SC0 subcritical configuration.

I. In addition, as shown in Figure 7.4, thermal neutrons have little contributions to the detector responses at those two positions. Therefore, although large standard deviations are obtained in the thermal energy groups, they are not important in the overall spatial correction factor calculations.

Furthermore, due to the equality in Equation 4.38 which imposes on the fuel region only, the relative value of $\hat{\phi}_p$ to $\phi_{0,k}$ is determined by their difference in the fuel region only. Because the neutron flux $\hat{\phi}_p$ is larger than $\phi_{0,k}$ at positions close to the external source, e.g., detector I, to satisfy the equality in Equation 4.38, there must exist a region, e.g., detector F, away from the external source, where $\hat{\phi}_p$ is relatively smaller than $\phi_{0,k}$ to yield $f_p > 1.0$, as shown in Figure 7.4(b). Therefore, with the prompt spatial correction factor f_p, we also physically explained why the area-ratio method will always overestimate the subcriticality at detector I, and underestimate the subcriticality at detector F in the MUSE-4 pulsed neutron experiments. The real

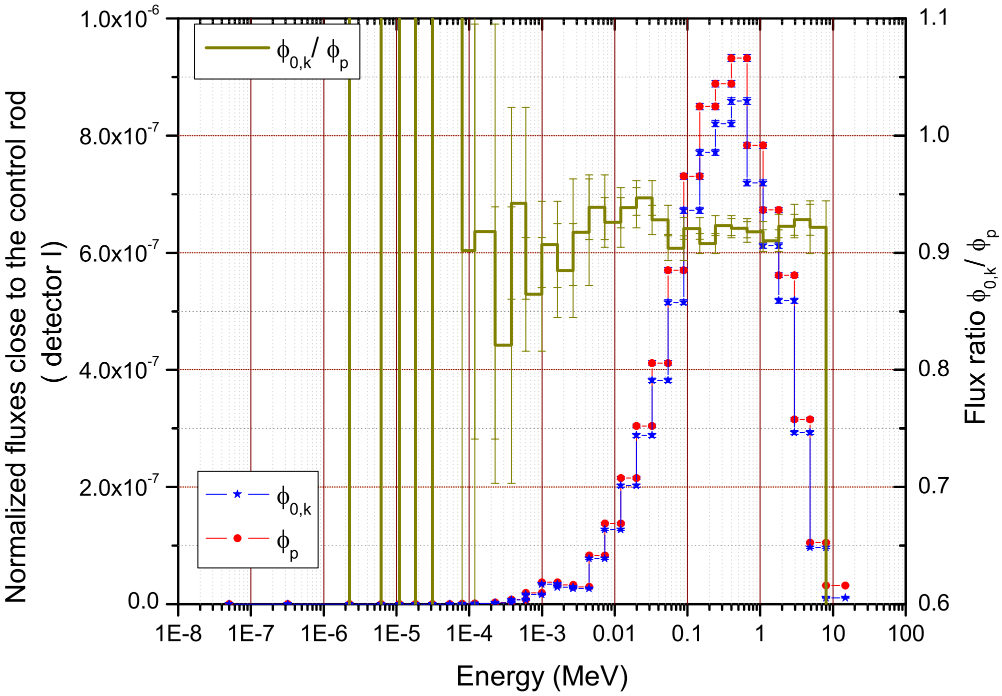

(a) Detector I

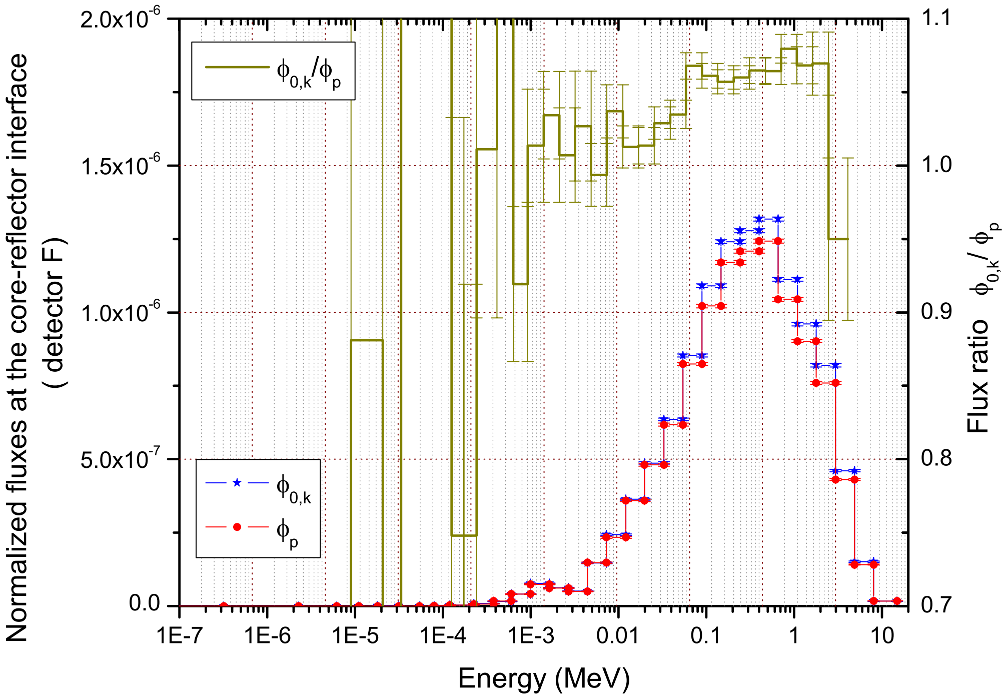

(b) Detector F

Figure 7.4: Comparison of the time-integrated prompt flux with the fundamental k-mode of the MUSE-4 SC0 subcritical configuration at (a) detector I and (b) detector F.

reactivity of the subcritical reactor is then bracketed by the measurements performed at these two positions.

When external or fission neutrons propagate into the reflector and shield regions, they slow down by interacting with nuclei there. As a result, the neutron spectrum becomes softer, and the peak of the ^{235}U detector response function is broadened and shifted to the low energy end as shown in Figure 7.3. Thus f_p is mostly determined by the difference between $\hat{\phi}_p$ and $\phi_{0,k}$ in the thermal energy range. Similar to the analysis for detectors F and I, we also compare $\hat{\phi}_p$ and $\phi_{0,k}$ at detector N in Figure 7.5. Here, $\hat{\phi}_p$ is still larger than $\phi_{0,k}$ at the high-energy groups with neutron energy larger than 0.1 MeV for detector N. However, the agreement between $\hat{\phi}_p$ and $\phi_{0,k}$ gradually becomes better in the epithermal energy groups with neutron energy around 1 keV. Due to the wide energy range of the detector response at position N as shown in Figure 7.3, the large differences in the high-energy groups become less important to the integration of the detector response over the entire energy domain. Therefore, f_p at detector position N is closer to 1.0 than f_p at detector F. The reactivities obtained from detectors in the shield and reflector regions are better estimations of the real reactivity than from the core detectors.

As the spatial correction factor f_p is also dependent on the detector's energy response function, with different types of neutron detector, the spatial dependence of the reactivity obtained from the area-ratio method may be different. This effect is often referred to as the "spectral effect". Specifically, we also calculate f_p for the MUSE-4 SC0 from our Monte Carlo simulations by replacing the ^{235}U detectors with the ^{237}Np detectors. Figure 7.6 compares f_p obtained for the ^{237}Np and ^{235}U detectors located diagonally across the reactor. It predicts that replacing the ^{235}U detector with the ^{237}Np detector would not necessarily reduce the spatial effects in

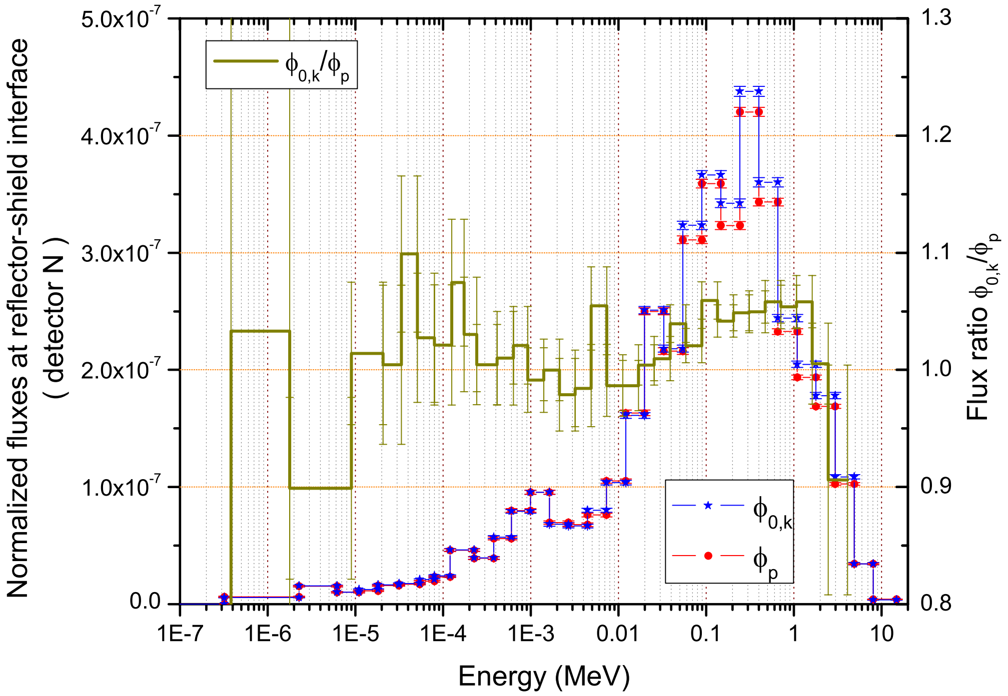

Figure 7.5: Comparison of the time-integrated prompt flux with the fundamental k-mode at detector N for the MUSE-4 SC0 subcritical configuration.

area-ratio method for the MUSE-4 pulsed-neutron experiment. In fact, the spatial corrections might be even larger at some positions, e.g., at detector positions F and N, with ^{237}Np detectors.

In summary, from our analysis of the spatial effects in the MUSE-4 area-ratio experimental data, we can conclude that the area-ratio method always overestimates the subcriticality of the reactor in fuel regions close to the external source, and underestimates it in fuel regions away from the external source. The real reactivity of the subcritical reactor can be bracketed by the reactivities measured at such two positions. The reactivity obtained at detectors in the reflector or shield regions away from the external source are less spatially dependent and are often better estimations of the real reactivity than in the fuel region. In addition, our analysis also shows that the ^{237}Np detector might not help reduce the spatial effects in the area-ratio method.

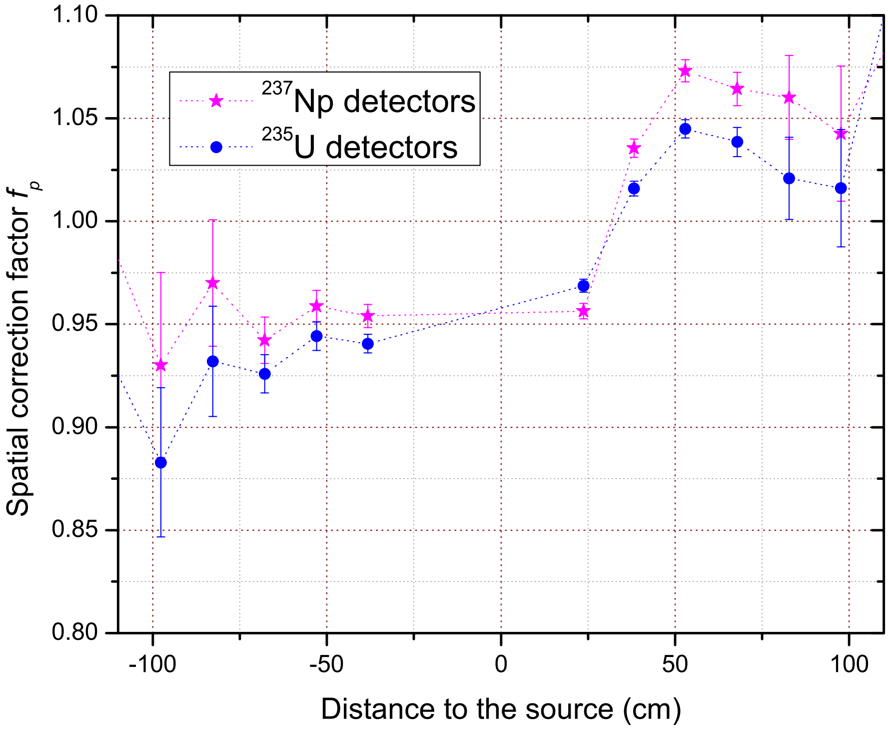

Figure 7.6: The comparison of spatial correction factors for ^{237}Np detectors and ^{235}U detectors diagonally crossing the MUSE-4 SC0 reactor.

7.3 The α-method of the MUSE-4 experiment

For the MUSE-4 pulsed-neutron experiments, the α-method was also applied to the experimental data. Figure 7.7(a) shows the detector responses recorded by detectors F, N and A in the core, reflector and shield regions for the MUSE-4 SC0 subcritical configuration, respectively. The delayed neutron background has already been subtracted from the detector responses. The decay constant α is obtained by applying an exponential fitting technique via a rolling window with a 20 μs interval. Figure 7.7(b) shows that the decay constant α varies continuously. From $t = 60$ μs to $t = 200$ μs, it decreases about 20% for detector F, and is almost halved for detectors N and A. In addition, the fitted α for the core detector F differs significantly from the fitted values for detectors N and A, with the values for detectors N and A only about half of that for detector F.

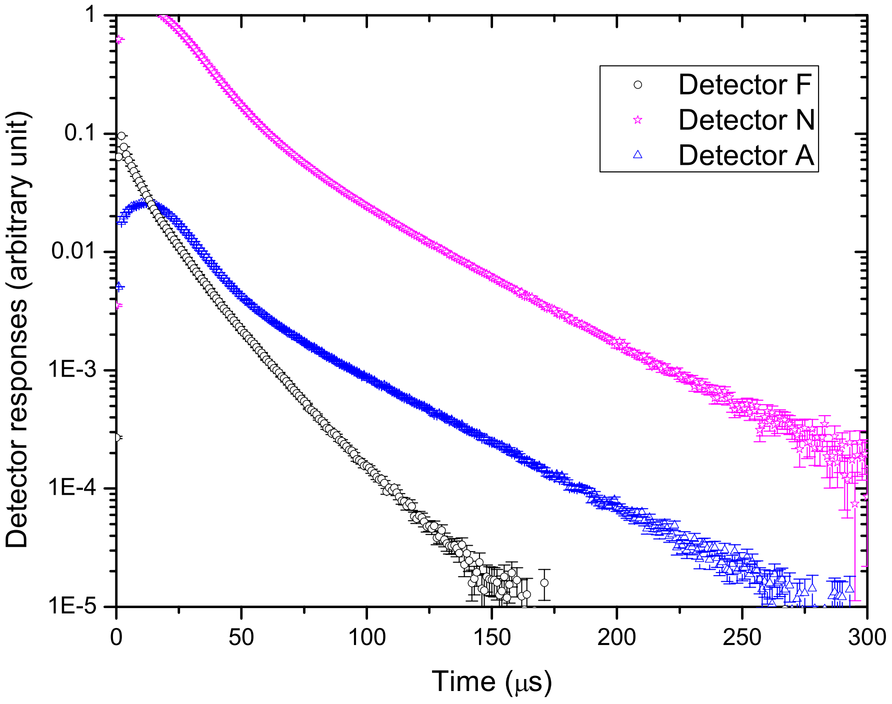

(a) Detector responses.

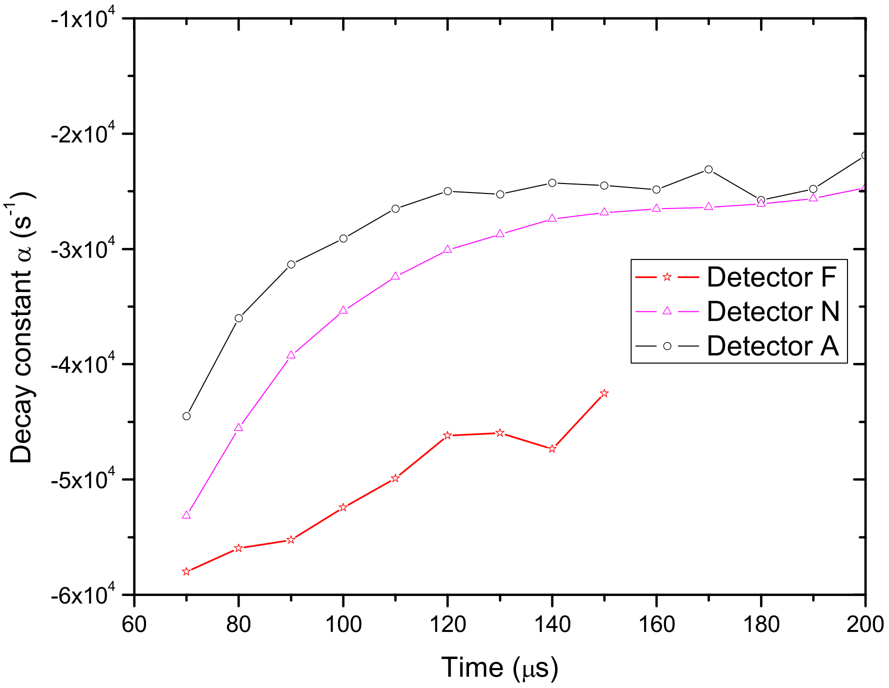

(b) Decay constants.

Figure 7.7: The experimental data for detector F, N and A in the pulsed-neutron experiments of the MUSE-4 SC0 subcritical reactor with delayed neutron background subtracted: (a) detector responses, (b) decay constants.

7.3.1 Numerical simulations of the MUSE-4 experiment for the α method

To analyze the spatial effects in the α-method, we rely primarily on dynamic simulations of the MUSE-4 pulsed-neutron experiment. For the MUSE-4 SC0 subcritical reactor, we use the MCNP model and the ERANOS 3-D diffusion model to simulate the detector responses at detector positions F, N and A, respectively. The ^{235}U fission chambers are simulated in the Monte Carlo model. Figure 7.8 shows that both the MCNP5 model and the deterministic ERANOS 3-D model can simulate the decay of the detector responses, e.g., detector F, for the first 200μs in the fuel region very well. However, for detectors N and A located at the reflector and shield regions, both the MCNP5 simulations and the ERANOS simulations start to deviate from the experimental data at about 100 μs after the neutron pulse is turned off.

Similar disagreements between the numerical simulations and the experimental data were also reported in other numerical simulations performed by Villamarin [15] and Carta [16]. In their Monte Carlo simulations, they decomposed the detector responses into six energy groups and found that at about 100 μs after the neutron pulse is turned off , neutrons detected in the reflector and shield regions are mainly thermal neutrons with neutron energy < 1 eV. However, due to the large absorption cross section of the MOX fuel (^{239}Pu), the thermal neutron population is low in the fuel region, and most of neutrons detected in the fuel region are fast neutrons. Therefore, the disagreements between the numerical simulations and the experiments mainly originate from the error in numerical simulations of thermal neutrons, and there are many possible sources of error. Because the reflector and shield regions consist mostly of iron, a sensitivity analysis involving a decrease of the ^{56}Fe capture cross sections was performed to identity the source of error, but the discussion related to this topic is out of the scope of this thesis. Nonetheless, as shown in Figure

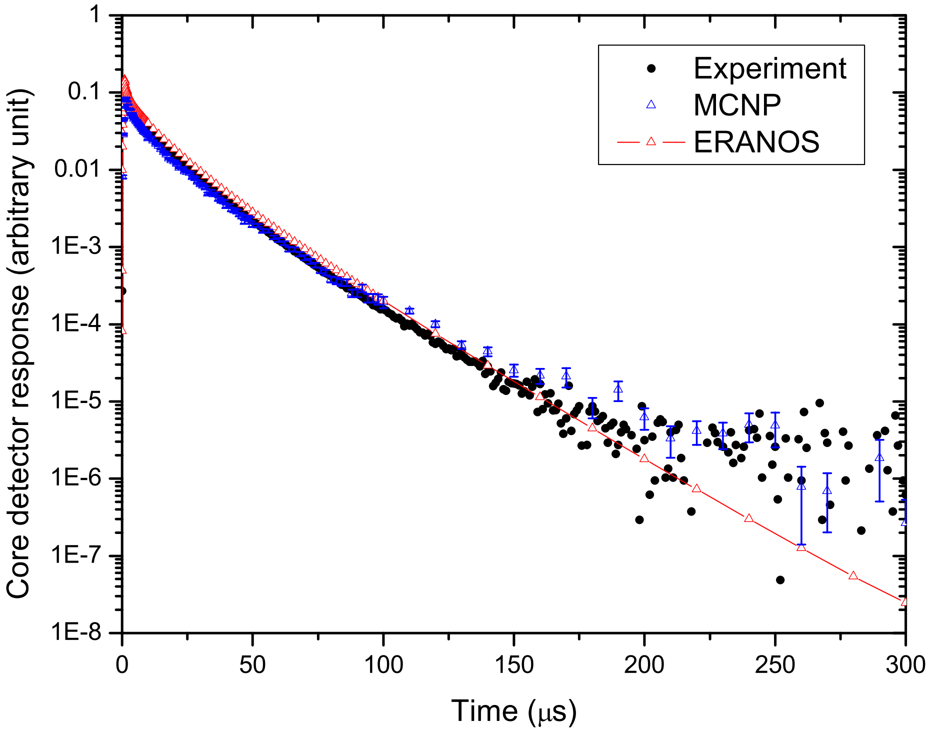

(a) Core detector F.

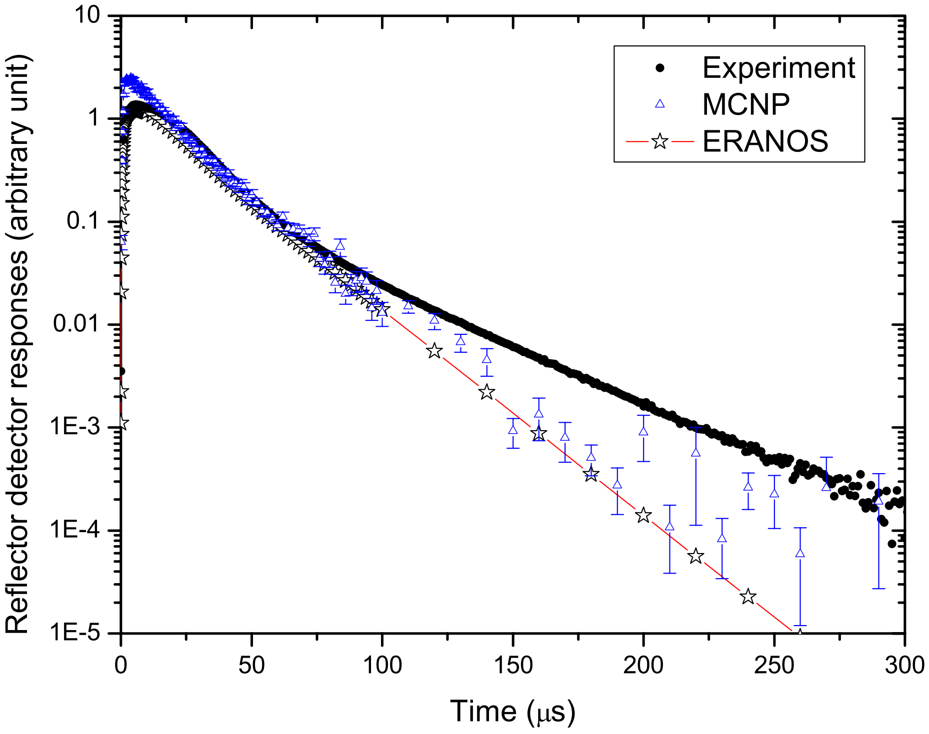

(b) Reflector detector N.

Figure 7.8: The simulated detector responses in the MUSE-4 SC0 reactor with delayed neutrons ignored: (a) core detector F, (b) reflector detector N.

7.8, the ERANOS deterministic simulation agrees with the Monte Carlo simulation reasonably well at all three positions. Thus, we will use the ERANOS deterministic model in the rest of our analysis.

7.3.2 The modified α-method

Unlike the thermal reactor we analyzed in Chapter VI, where the fitted α from the simulated detector responses are spatially coherent, the spatial effects in the MUSE-4 experiment are much more complicated for the α-method. Namely, the fitted α continuously varies over the spatial and time domains as shown in Figure 7.7(b). Consequently, the fundamental decay constant α can not be properly retrieved from the experimental data. For this type of problem, as we discussed in Section 4.2.2, the modified α-method provides a good way of obtaining a spatially-independent reactivity of the system. Thus, we first use the modified α-method to estimate the reactivity for the MUSE-4 SC0 subcritical reactor.

The time-dependent shape function is obtained from the ERANOS 3-D numerical simulation. The kinetics parameter $\Lambda(t)$ and $\beta(t)$ can also be obtained from the numerical simulations. As shown in Figure 7.9, $\beta(t)$ is almost a constant during the source transient. However, the mean generation time $\Lambda(t)$ varies significantly over the transient. With the experimental data measured at each detector position, the amplitude function can then be obtained based on Equation 4.62. By integrating over the interval $[20\ ,60]$ μs, the reactivity of the MUSE-4 SC0 subcritical reactor is then obtained through the modified α-method and is almost spatially coherent as shown in Table 7.4, where $\beta = 0.00334$ is the measured value in the MUSE-4 reference reactor. Compared with the average value of the reactivity obtained from the area-ratio method after the spatial corrections, the modified α-method underestimates the overall subcriticality about 2 \$ everywhere in the reactor. This is due to the

Table 7.4: The calculated ρ_0 of the MUSE-4 SC0 subcritical reactor from the modified α-method.

Detector	F	I	L	H	M
ρ (\$)	-10.5	-10.5	-10.6	-9.75	-10.4
Detector	N	G	A	B	Area-ratio
ρ (\$)	-10.1	-10.1	-10.6	-10.7	-12.3

modeling error of the ERANOS numerical model. Particularly, the 3-D ERANOS diffusion calculation gives $k_{eff} = 0.964$ and $\rho = -11.1\$$, which underestimates the subcriticality of the reactor by about 1.2\$. As we discussed in Section 4.2.2, the systematic error in the numerical model then directly affects the accuracy of the reactivity obtained from the modified α-method, as we have shown in Table 7.4.

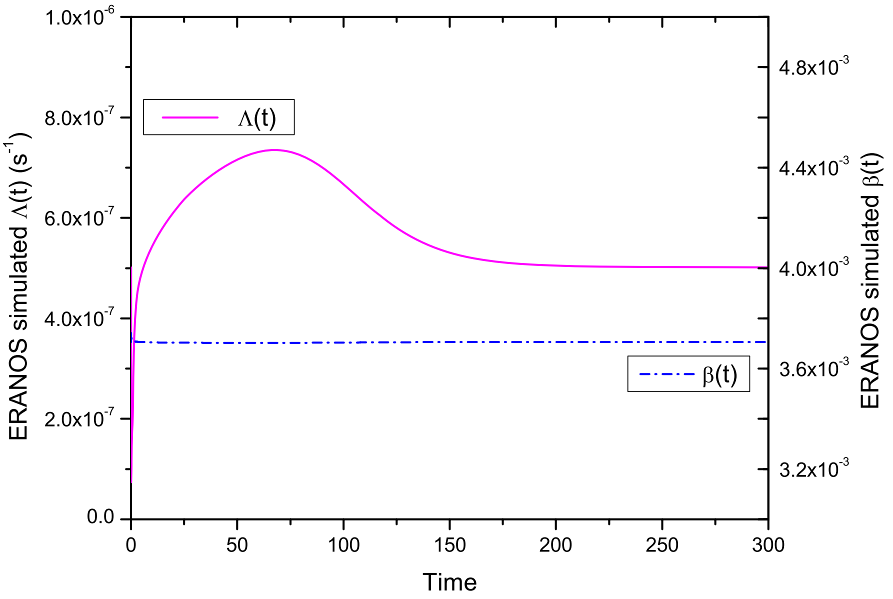

Figure 7.9: The 3-D ERANOS simulations of the mean generation time $\Lambda(t)$ and the effective delayed-neutron fraction $\beta(t)$ in the the MUSE-4 SC0 reactor with delayed neutrons included.

7.3.3 Modal analysis of the α-method

For the α-method, if a spatially independent decay constant can be obtained from the experimental data, the traditional α-method can then be used directly to obtain the reactivities of the system, with the mean generation time calibrated by the numerical simulations. In addition, as also discussed in Section 4.2, if the high-order prompt-neutron harmonics all decay away within a short period of time, the fitted α would be a spatially-independent constant, which equals the fundamental prompt α-eigenvalue α_0. Thus, in this section, we will try to obtain α_0 for the MUSE-4 SC0 reactor numerically.

To simplify the problem, we set up a 2-D deterministic model instead of the 3-D full scale model of the MUSE-4 reactor. The 2-D numerical model only represents the X-Y midplane of the 3-D model as shown in Figure 7.1. By adjusting the geometric buckling in the z-direction, the multiplication factor is tuned to be 0.9643, which is very close to $k_{eff} = 0.9641$ of the 3-D ERANOS model. The detector responses corresponding to the core detector F, reflector detector N and shield detector A are also simulated by the ERANOS code package. As shown in Figure 7.10, the 2-D simulations agree reasonably well with the 3-D simulations up to the first 200 μs after the neutron pulse is turned off.

With a rolling window and a fixed fitting width, the decay constants can also be obtained from the 2-D ERANOS simulations at detector position F, N and A, as shown in Figure 7.11. For detector F, the fitted α for this 2-D numerical model varies similarly to the fitted α obtained from the experimental data over the space and time domains as illustrated in Figure 7.7(b). The fitted values are, however, different for detectors N and A because of the differences between the numerical simulations and the experimental data as illustrated in Figure 7.8(b). Nonetheless, the fitted α for this 2-D numerical model also varies continuously over the space and time domain. Therefore, we will calculate the fundamental prompt α-eigenvalue for this 2-D numerical model.

According to Equation 4.57, the decay constant can be expressed as a modal

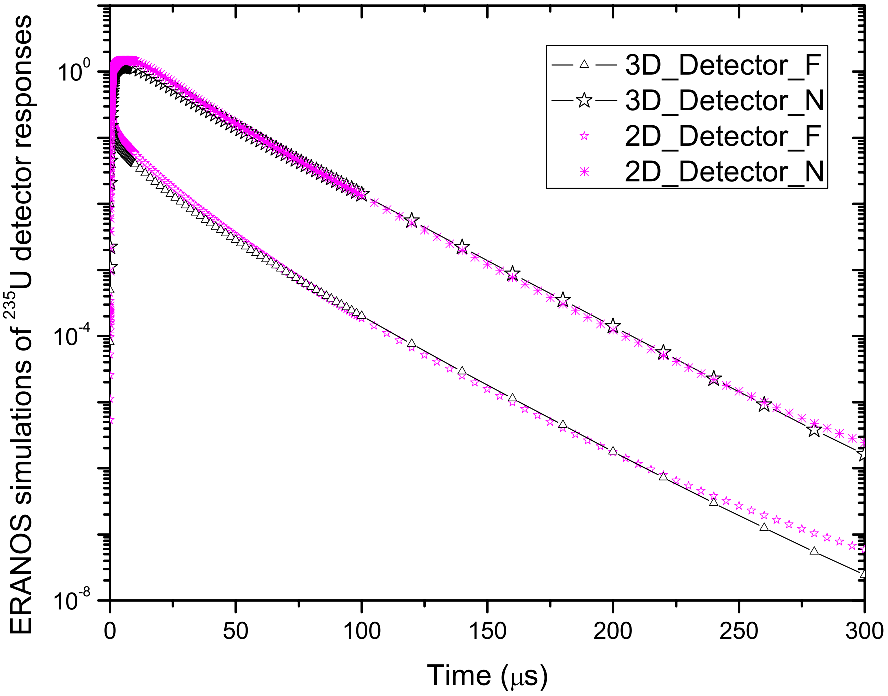

Figure 7.10: The 2-D ERANOS simulations of detector responses for core detector F and reflector detector N in the MUSE-4 SC0 reactor with delayed neutrons ignored.

expansion

$$\alpha(\mathbf{r}_D, t) = \frac{\partial \ln R(\mathbf{r}_D, t)}{\partial t} = \frac{\partial}{\partial t} \ln \left[\sum_m^M A_m(\Delta T) \left\langle \Sigma_d, \phi_{m,p} \right\rangle_E e^{\alpha_m (t - \Delta T)} \right], \tag{7.3}$$

where $\alpha(\mathbf{r_D}, t)$ is a space- and time-dependent function if the high-order modal terms are not negligible, and α_0 is then the asymptotic value of $\alpha(\mathbf{r}_D, t)$ at any position which could be measured from pulsed-neutron experiments. In addition, α_0 also corresponds to the decay rate of the slowest decay component in the detector response R, and is the fundamental prompt α-eigenvalue of the subcritical reactor. The fundamental mode $\phi_{0,p}$ describes the distribution of the slowest decaying component in the detector responses.

Thus, for our 2-D numerical model, as shown in Figure 7.11, the fitted α does not reach the asymptotic value of α_0 after the detector responses have decreased by more than six orders of magnitude, which indicates that the high-order modal terms still

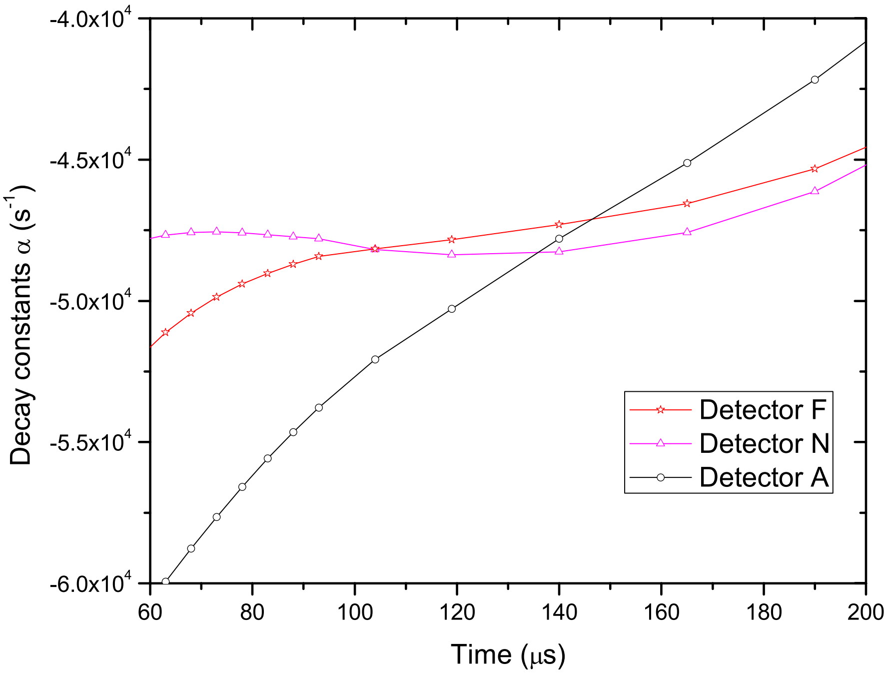

Figure 7.11: The fitted decay constants α of the simulated ^{235}U detector responses for detector F, N and A in the ERANOS 2-D numerical model of the MUSE-4 subcritical SC0 reactor.

make important contributions to the detector responses. With the prompt α-modes calculated via IRAM, we compare the modal expansion of the detector response R with the ERANOS simulation. The modal expansions are calculated through Equation 4.51, with the fundamental modal term only, i.e., $M = 0$, or with the first 16 modal terms, i.e., $M = 15$. The disagreement between the modal-expansion fluxes and the ERANOS simulation is very similar at other detector positions. Figure 7.12 only shows the comparison at detector F. Specifically, the detector response corresponding to the fundamental mode is much smaller than the ERANOS simulation within the first 300 μs, which indicates that the fundamental modal term has little contributions to the detector responses in the prompt-neutron decay region. The majority of the prompt neutrons in the reactor decay away with a decay rate faster than α_0.

Theoretically, the fundamental prompt α-mode describes the distribution of the

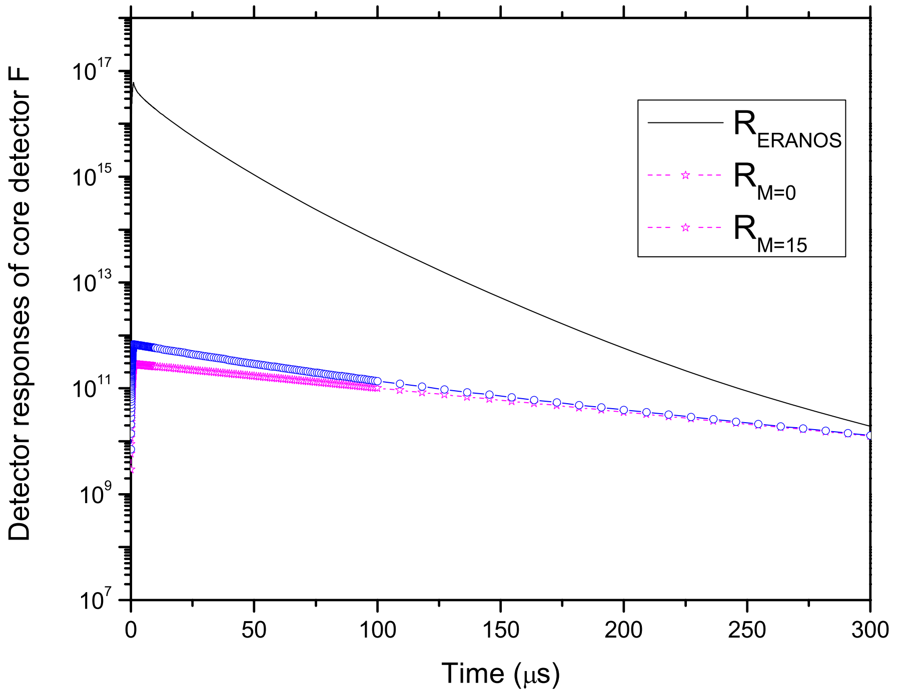

Figure 7.12: Comparison of the ERANOS simulated ^{235}U with the modal expansions ($M = 0$) and ($M = 15$) of the detector responses at detector F in the 2-D numerical model of the MUSE-4 SC0 subcritical reactor.

slowest decaying component in detector responses. As shown in Figure 7.13, for our 2-D numerical model, the slowest decaying component in the detector response peaks in the lead buffer and the beam pipe regions, and has very small values in other regions. In addition, we also calculate the first few high-order prompt α-eigenvalues, e.g., $\alpha_1 = -11052$ s^{-1} and $\alpha_2 = -12788$ s^{-1}. The detector response maps for the high-order modes are very similar to the fundamental-mode response shown in Figure 7.13. Particularly, the detector responses also peak in the lead buffer and beam pipe regions with relatively small values in other regions. For clear illustrations, we only plot the detector responses $\langle \Sigma_d, \phi_{m,p} \rangle_E$ for the first three prompt-modes at $y = 0$ and at $x = 0$, respectively, in Figure 7.14. We note that the high-order modes only represent the detailed spatial variations of the detector responses in the lead buffer and beam pipe regions.

In fact, the fundamental eigenvalue α_0 obtained from IRAM calculation for this

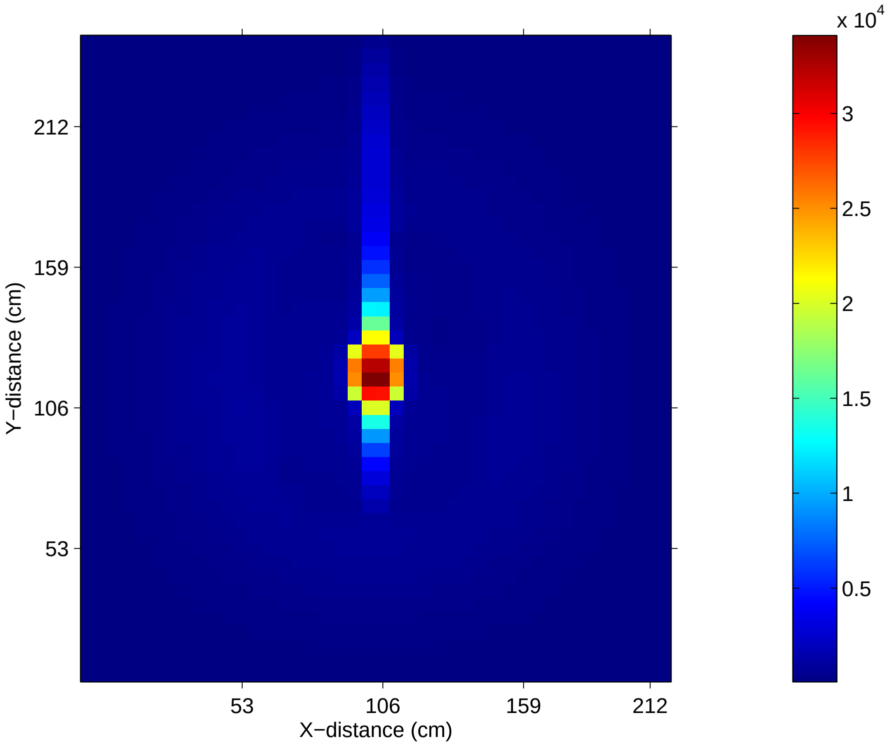

Figure 7.13: The calculated detector response $\langle\Sigma_d, \phi_{0,p}\rangle_E$ corresponding to the prompt α-mode for the 2-D numerical model of the MUSE-4 SC0 subcritical reactor.

2-D numerical model is about -10436 s^{-1}, which is much smaller in magnitude than the largest decay constant in Figure 7.11. In addition, the expansion coefficient $A_m(0)$ corresponding to each modal term at the beginning of the pulse can also be calculated based on Equation 4.21 as

$$A_m(0) = \frac{\left\langle \phi_{0,p}^{+}, Q_0 \right\rangle_{\mathbf{r},E}}{\left\langle \phi_{0,p}^{+}, 1/v\phi_{0,p} \right\rangle_{\mathbf{r},E}} = \frac{\left\langle \phi_{0,p}^{+}, Q_0 \right\rangle_{\mathbf{r},E}}{\sum_g \left\langle \phi_{0,p}^{+}, 1/v\phi_{0,p} \right\rangle_{\mathbf{r},g}}. \qquad (7.4)$$

In the pulsed-neutron experiment, the external neutron source is always injected from the high-energy groups. Thus, we calculate the numerator of $A_0(0)$ corresponding to each energy group normalized by its denominator. As shown in the second to fourth column of Table 7.5, the denominator of $A_m(0)$ is mainly determined by its thermal component. Besides, we also calculate the first three modal terms at the beginning of the pulse as listed in Table 7.6. Compared with the fundamental modal term, the high-order modal terms are not small, and make significant contributions

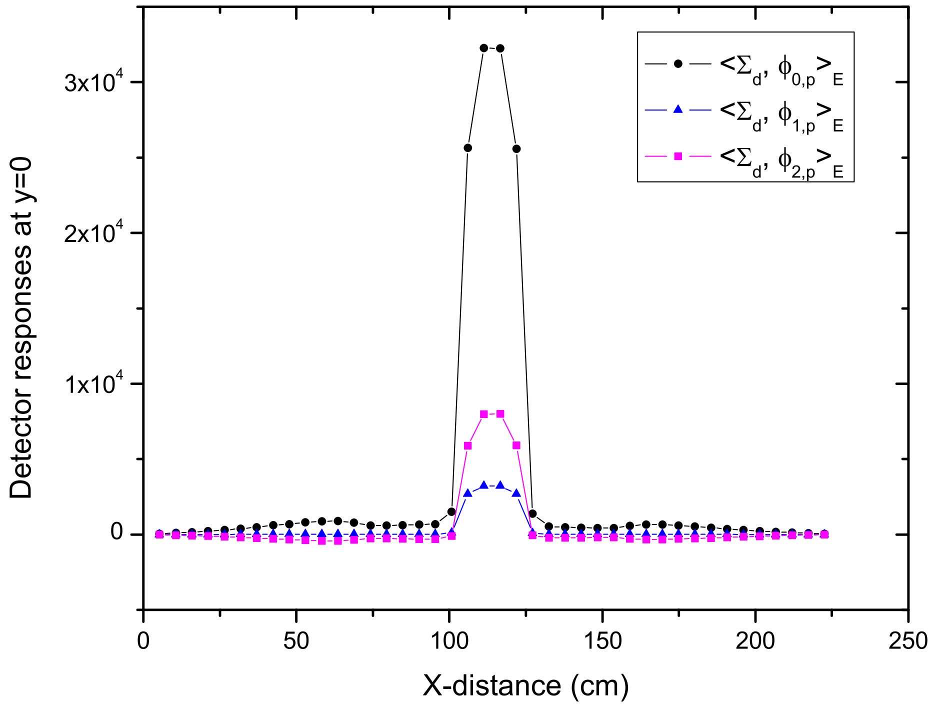

(a) At $y = 0$.

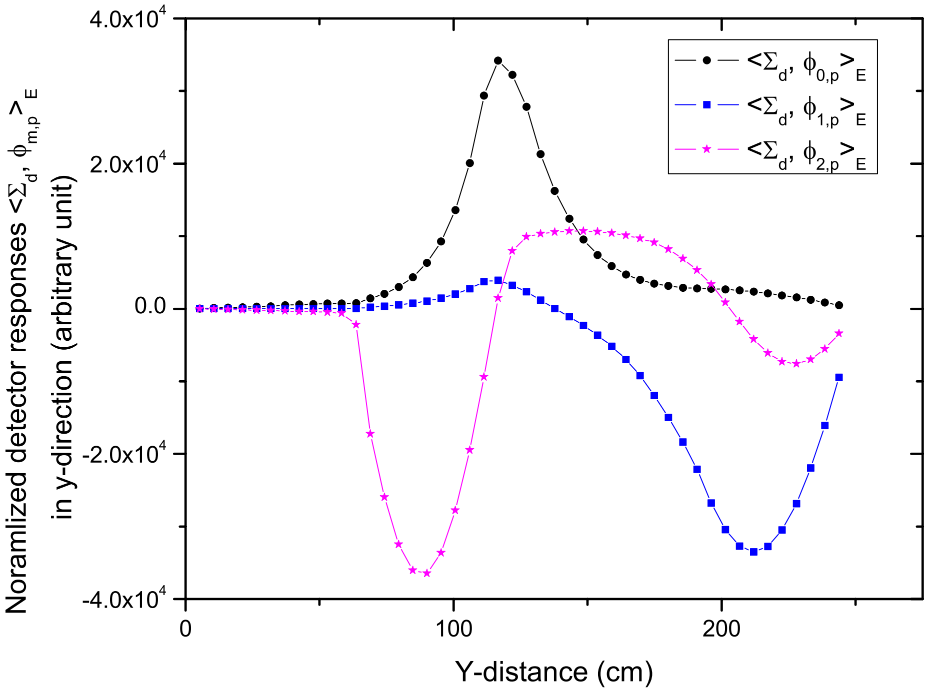

(b) At $x = 0$

Figure 7.14: The calculated detector response corresponding to the prompt α-modes for the 2-D numerical model of the MUSE-4 SC0 subcritical reactor: (a) along x-direction at $y = 0$, (b) along y-direction at $x = 0$.

Table 7.5: The denominator of the modal expansion coefficient $A_m(0)$ at each energy group for the 2-D numerical model of the MUSE-4 SC0 subcritical reactor.

Upper energy bound	Without Cadmium			With Cadmium		
	$m = 1$	$m = 2$	$m = 3$	$m = 1$	$m = 2$	$m = 3$
14 MeV	1.0E-05	-3.95E-05	5.08E-06	7.44E-06	-5.41E-06	2.08E-06
1 keV	5.02E-05	1.00E-06	2.46E-05	3.92E-05	-5.47E-04	1.54E-04
1 eV	2.17E+00	2.45E-01	3.00E+00	2.42E-05	-5.39E-03	1.67E-03
Sum	2.17E+00	2.45E-01	3.00E+00	7.08E-05	-5.94E-03	1.82E-03

Table 7.6: The modal expansion coefficient $A_m(0)\left\langle \Sigma_d, \phi_{m,p} \right\rangle_g$ at detector position F for the 2-D numerical model of the MUSE-4 SC0 subcritical reactor.

Upper energy bound	Without Cadmium			With Cadmium		
	$m = 1$	$m = 2$	$m = 3$	$m = 1$	$m = 2$	$m = 3$
14 MeV	2.07E+11	-3.60E+10	9.49E+10	5.12E+15	-3.31E+11	2.18E+13
1 keV	2.60E+10	-3.38E+09	9.10E+09	6.47E+14	1.04E+10	2.98E+12
1 eV	6.21E+08	-1.20E+09	7.45E+09	1.46E+13	4.32E+09	1.82E+12
Sum	2.29E+11	-4.06E+10	1.11E+11	5.78E+15	-3.17E+11	2.66E+13

to the overall detector responses. Thus, a very large number of modal terms would be required to accurately approximate the time-dependent detector responses in the first few hundred μs after the neutron pulse is turned off.

Physically, this can also be explained by the fact that the materials in the lead buffer and in the beam pipe regions have very small neutron absorption cross sections for thermal neutrons, i.e., 10 times smaller than those in the shield region. Therefore, thermal neutrons that propagate into the lead buffer and beam pipe regions stay alive relatively longer than in other regions. These long-lived neutrons in the lead buffer and beam pipe regions can return to the subcritical fuel regions, and lead to an extremely slow neutron decay in the detector responses. Because the MUSE-4 SC0 subcritical reactor is a fast reactor, and the lead buffer and the beam pipe are also small regions in the reactor. Therefore, the number of these long-lived thermal neutrons is very small, and their contributions to the detector responses are then small in the first 300 μs as demonstrated in Figure 7.12.

Overall, the fundamental decay constant α_0 of a subcritical reactor is determined by the slowest neutron propagation process in the reactor. Usually, it takes much a longer time for thermal neutrons to stabilize than for fast neutrons after the external source is turned off. For the MUSE-4 subcritical reactor, the long-lived thermal neutrons in the beam pipe and lead buffer regions control the final decay rate of detector responses. Before reaching the asymptotic decay rate, the neutron flux distribution varies continuously over time and space, and so does the decay constant. The asymptotic decay constant is not observable in the MUSE-4 pulsed-neutron experiments because the neutron detectors have limited efficiency and the detector responses decay out before the neutron flux distribution reaches its asymptotic shape. The asymptotic decay constant α_0 cannot represent the majority of the prompt-neutrons decay in this 2-D numerical model.

To search a decay constant α, which is the decay rate of the majority of the prompt-neutrons in the reactor, one straightforward way is to terminate the long-lived thermal neutrons in the lead buffer and beam pipe regions, because the fraction of them is small in the MUSE-4 subcritical reactor. To eliminate the contamination of the slow decaying components in the detector responses, in an alternate 2-D numerical model, we assume that the accelerator beam pipe and the lead buffer are wrapped around by a 1 mm-thick cadmium layer. Therefore, thermal neutrons are absorbed by the cadmium layer while traveling from the fuel to the buffer and the beam pipe regions or from those regions back to the fuel region [53].

With the thin cadmium layer present in our 2-D numerical model, we obtain $k_{eff} = 0.961$, which is only about 0.3% less than that for the original 2-D model. However, the cadmium layer has a significant impact on the dynamic behavior of the subcritical reactor. The magnitude of the fundamental prompt α-eigenvalue increases significantly, i.e., $\alpha_0 = -49121$ s^{-1}, which is about four times larger than its original value. The neutron flux distribution is then expected to achieve an asymptotic shape much faster than that in the original 2-D model. To validate this conclusion, we also use the ERANOS code package to perform the numerical simulations of a neutron pulse injected into the 2-D subcritical reactor with the cadmium layer. The decay constants are then obtained by applying an exponential fitting on the simulated detector responses at detector positions F, N and A, respectively. As shown in Figure 7.15, the fitted α is similar to the fitted α of the original 2-D model in the first 100 μs. In Figure 7.11, the fitted α varies continuously over the next 200 μs. However, for the 2-D model with the cadmium layer, the fitted α converges to α_0, which is calculated via IRAM, as shown in Figure 7.15.

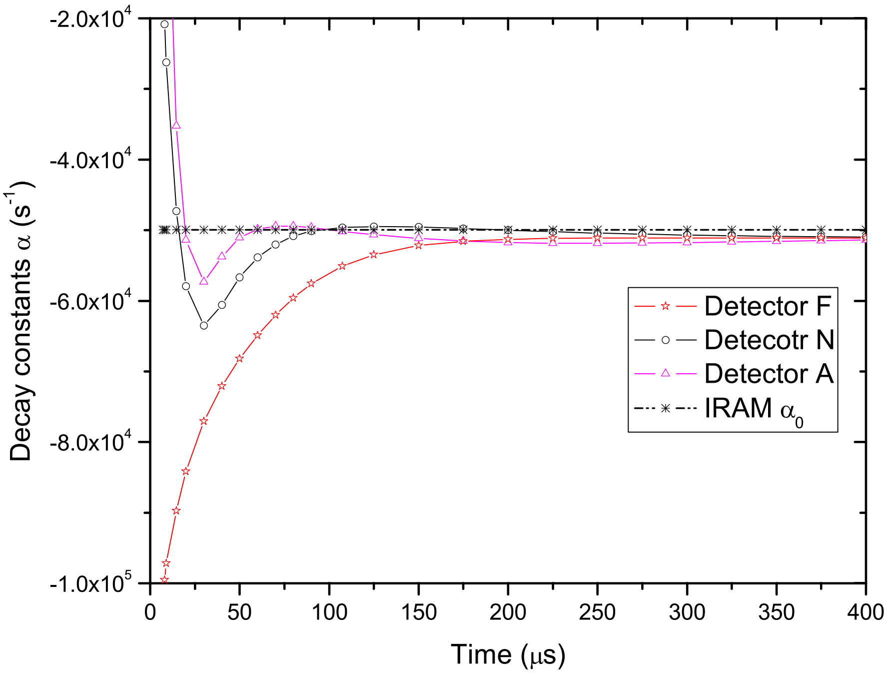

Figure 7.15: The fitted decay constants α of the simulated ^{235}U detector responses for detectors F, N and A in the ERANOS 2-D numerical model of the MUSE-4 SC0 subcritical reactor with a 1mm-thick cadmium layer.

For this 2-D model with the cadmium layer, the fast convergence of the neutron flux distribution to the fundamental prompt α-mode can also be demonstrated by comparing the ERANOS simulation with the modal expansions as shown in Figure 7.16. The ERANOS 2-D time-dependent simulations agree reasonably well with its fundamental modal term after about 100 μs, and decay nearly exponentially till 400 μs.

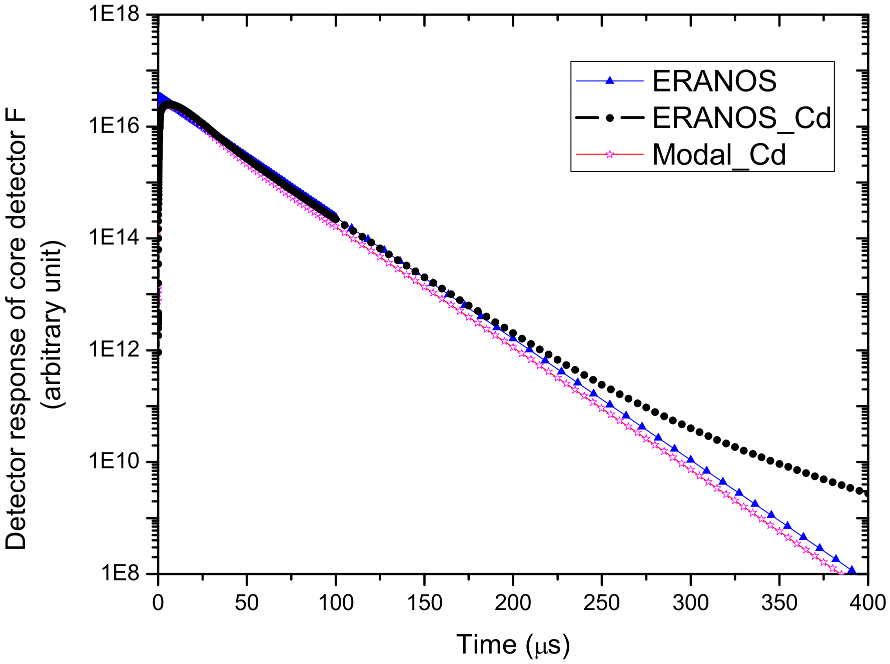

Figure 7.16: Comparison of the ERANOS simulated ^{235}U detector response with its fundamental modal expansion ($M = 0$) at detector F in the 2-D numerical model of the MUSE-4 SC0 subcritical reactor with the cadmium layer.

In addition, compared with Figure 7.12, Figure 7.16 also shows that with a cadmium layer included, the fundamental modal term has a very large contribution to the total detector response in the prompt neutron decay region. As shown in Table 7.5, the corresponding fundamental modal expansion coefficient is also much larger than the coefficient for the 2-D model without the cadmium layer, indicating that the fundamental prompt α-eigenvalue characterizes the exponential decay rate of the majority of the prompt neutrons in the subcritical reactor. In addition, as shown in Table 7.6, with the cadmium layer included, the high-order modal terms are relatively much smaller compared with the fundamental modal term. Thus, the fundamental modal term dominates the neutron flux quickly in this 2-D numerical model. Moreover, as shown in Figure 7.16, the cadmium layer has little impact on the detector responses in the first 200 μs. Therefore, the calculated α_0 from this 2-D numerical model with the cadmium layer included also describes the decay rate of most of the prompt neutrons in the 2-D numerical model without the cadmium layer. Furthermore, at detector F, because the 2-D ERANOS simulation agrees with the experimental data well in the first 200 μs as shown in Figures 7.10 and 7.8(a), the calculated α_0 will also describe the exponential decay of most of the prompt neutrons in the actual MUSE-4 SC0 reactor. The corresponding fundamental prompt α-mode then describes the distribution of the corresponding component in the detector responses as shown in Figure 7.17. Compared with Figure 7.13, the detector responses peaks in the reflector region. In other words, the decay constant is then determined by the thermal neutrons decay in the reflector region. This result is also consistent with Villamarin's Monte Carlo simulations [15].

7.3.4 Mean generation time variations

Finally, in order to obtain the reactivity from the α-method, we also want to examine the variation of the mean generation time Λ when the MUSE-4 reactor is made to be subcritical from the reference configuration. In the 2-D numerical model with the cadmium layer, for the close-to-critical configuration with no control rod inserted into the reactor, we obtain $k_{eff} = 0.9994$ and $\Lambda = 0.454$ μs. While at the subcritical configuration with $k_{eff} = 0.961$, we obtain $\Lambda = 0.711$ μs, which is about 50% larger than Λ calculated at the close-to-critical configuration. Thus, with the calculated α_0 from the 2-D numerical model, and the measured $\Lambda^m_{ref} = 0.586$ μs and

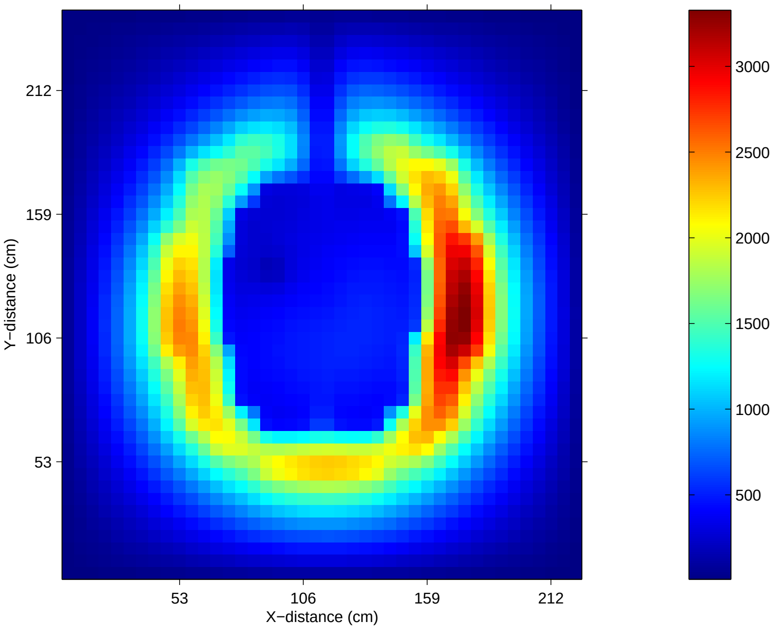

Figure 7.17: The calculated detector response $\langle \Sigma_d, \phi_{0,p} \rangle_E$ corresponding to the prompt α-mode of the ERANOS 2-D numerical model of the MUSE-4 SC0 subcritical reactor with the cadmium layer.

$\beta = 0.00334$, the reactivity of the subcritical reactor can be calculated as

$$\begin{aligned} \rho &= \alpha_0 \Lambda^m_{ref} f_\Lambda + \beta \\ &= -49121 \times 0.586 \times 10^{-6} * \left(\frac{0.711}{0.454} \right) + 0.00334 \\ &= -0.04182 = -12.5\,\$, \end{aligned} \tag{7.5}$$

which agrees well with the reactivity obtained from the area-ratio method.

In addition, as indicated in Figure 7.9, the quasi-static mean generation time $\Lambda(t)$ varies significantly in a pulsed-neutron experiment. Similar to the detector responses R, $\Lambda(t)$ can also be expressed in terms of the modal expansions. In the prompt neutron decay region, by ignoring the delayed neutrons, the total neutron flux is then expanded with the prompt α-modes, and $\Lambda(t)$ can then be written as

$$\begin{aligned} \Lambda(t) &= \frac{\left\langle \phi^+_{0,k}, v^{-1}\psi \right\rangle_{\mathbf{r},E}}{\left\langle \phi^+_{0,k}, \chi \mathbf{F} \psi \right\rangle_{\mathbf{r},E}} = \frac{\left\langle \phi^+_{0,k}, v^{-1} \left[T(t)\psi \right] \right\rangle_{\mathbf{r},E}}{\left\langle \phi^+_{0,k}, \chi \mathbf{F} \left[T(t)\psi \right] \right\rangle_{\mathbf{r},E}} \\ &= \frac{\left\langle \phi^+_{0,k}, v^{-1}\phi_p \right\rangle_{\mathbf{r},E}}{\left\langle \phi^+_{0,k}, \chi \mathbf{F} \phi_p \right\rangle_{\mathbf{r},E}} = \frac{\sum_m A_m(t) \left\langle \phi^+_{0,k}, v^{-1}\phi_{m,p} \right\rangle_{\mathbf{r},E}}{\sum_m A_m(t) \left\langle \phi^+_{0,k}, \chi \mathbf{F} \phi_{m,p} \right\rangle_{\mathbf{r},E}}, \end{aligned} \tag{7.6}$$

which shows that $\Lambda(t)$ varies in the time domain due to the presence of the high-order harmonics. With the prompt α-modes calculated via IRAM, we also obtain $\Lambda_M(t)$ with the first few prompt α-modes included:

$$\Lambda_M(t) = \frac{\displaystyle\sum_{m=0}^{m=M} A_m(t) \left\langle \phi_{0,k}^{+}, v^{-1}\phi_{m,p} \right\rangle_{\mathbf{r},E}}{\displaystyle\sum_{m=0}^{m=M} A_m(t) \left\langle \phi_{0,k}^{+}, \chi\mathbf{F}\phi_{m,p} \right\rangle_{\mathbf{r},E}}, \tag{7.7}$$

where M is the modal expansion order in Equation 4.48. Thus, according to Equation 7.7, Λ_0 is a constant, and is the static mean generation time $\bar{\Lambda}_0$ we defined previously in Equation 4.55. For our 2-D model with the thin cadmium layer, Figure 7.18 shows that the calculated Λ_M varies with time and reach the asymptotic value $\bar{\Lambda}_0$ when all the high-order harmonics decay away. However, we notice that the magnitude variations of Λ_M is very small in the first 100 μs compared with the quasi-static $\Lambda(t)$ illustrated in Figure 7.9. This is because a large number of high-order modes make significant contributions to Λ_M right after the neutron pulse is turned off. As shown in Figure 7.18, with more modes included, Λ_M should be better approximations to $\Lambda(t)$.

7.4 Comparison of the k-mode with the α-mode in a fast subcritical system

The prompt α-modes and k-modes are extensively utilized in our analysis of the spatial effects in the pulsed neutron experiments. The delayed α-modes are approximated by the corresponding k-modes in our modal analysis. With a little amount of additional work, we will compare the calculated fundamental k-mode and the fundamental α-modes in the MUSE-4 SC0 subcritical reactor. Specifically, we use the 2-D numerical model with the cadmium layer. The fundamental k-mode and the α-modes are calculated via IRAM, with the BICGSTAB method as the inner

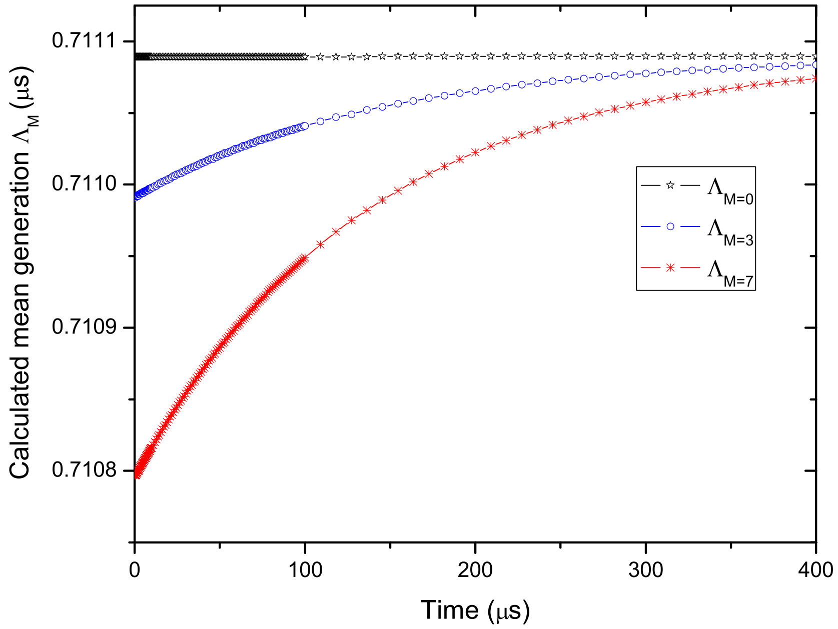

Figure 7.18: The calculated mean generation time Λ_N with modal expansion order $M = 0, 3, 7$ respectively for the 2-D numerical model of the MUSE-4 SC0 subcritical reactor with the cadmium layer.

iteration solver and the relaxation parameter $\omega = 1.4$ for the SSOR preconditioner.

The flux distributions are compared in Figure 7.19 at three different detector positions F, N and A in the fuel, reflector and shield regions, respectively. For the sake of clearly illustrating the flux distributions, the normalized fluxes in the shield and in the fuel regions are reduced by factors of 100 and 1000, respectively. Figure 7.19(a) indicates that the prompt α-mode possesses a much softer neutron spectrum than the k-mode at all three positions. In contrast to the large differences between the prompt α-mode and the k-mode, the fundamental k-mode closely agrees with the delayed α-mode everywhere in the subcritical reactor, as shown in Figure 7.19(b). Therefore, it also verifies that the fundamental k-mode is indeed a good approximation for the delayed α-mode.

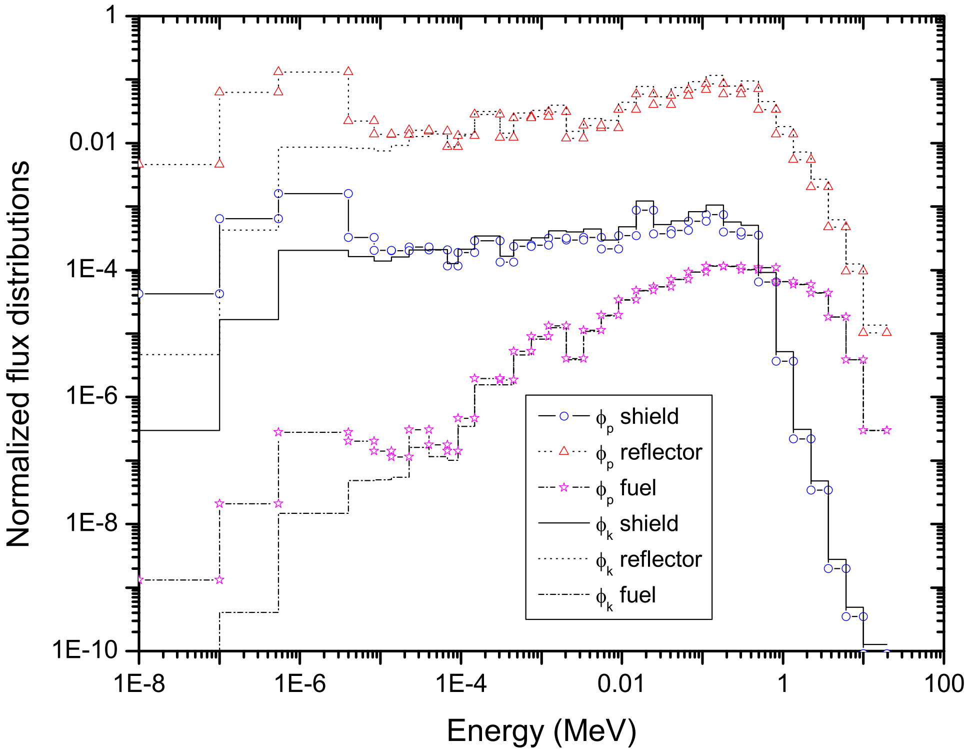

(a)

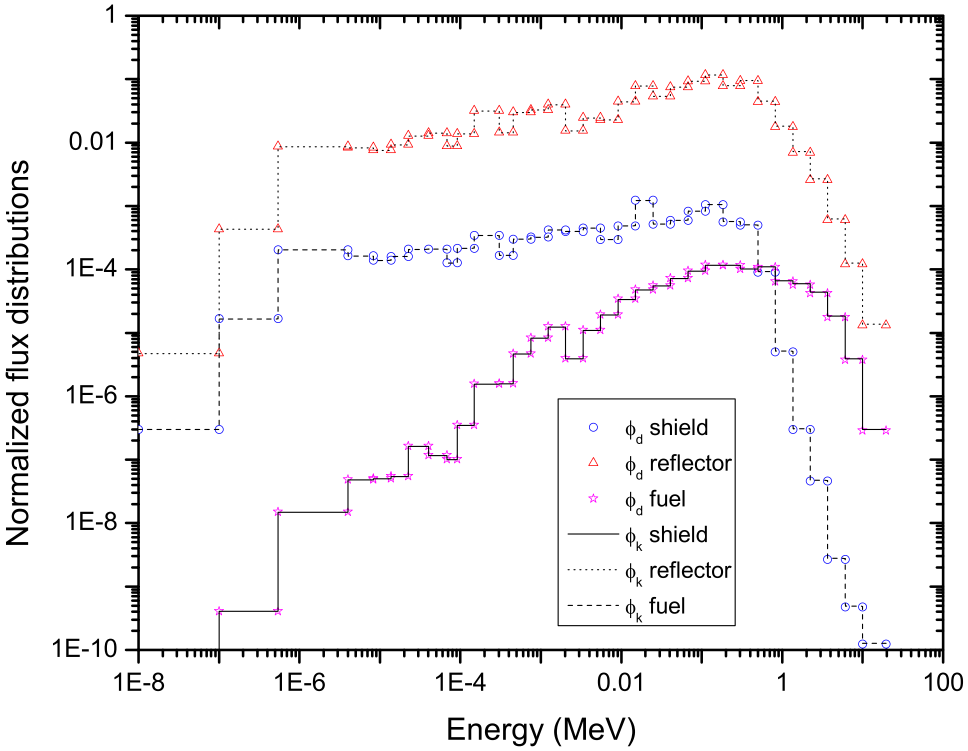

(b)

Figure 7.19: Comparison of flux distributions at fuel, reflector and shield regions in the MUSE-4 subcritical system with the cadmium layer: (a) fundamental k-mode compared with prompt α-mode (b) fundamental k-mode compared with delayed α-mode. Fuel and shield fluxes are reduced by factors of 100 and 1000, respectively.

CHAPTER VIII

Summary and Conclusions

8.1 Summary of the thesis

In this thesis, we have studied the spatial effects in pulsed-neutron experiments. Both the area-ratio method and the α-method are traditional methods to measure the reactivity of a subcritical reactor with pulsed-neutron experimental data, and their spatial effects are examined carefully in this thesis.

The area-ratio method is originally derived based on a true "point" reactor. It states that the reactivity in dollars of a subcritical reactor is equal to the negative ratio of the prompt neutron area A_p and the delayed neutron area A_d. For a close-to-critical reactor, which can often be treated as a point reactor, the method can be derived directly from the point kinetics equations. For a subcritical reactor away from its critical status, the reactivity obtained from the area-ratio method varies at different neutron detector locations. Traditional kinetics distortion factor was used to correct the spatial effects in the area-ratio method. However, it can only compensate for the spatial effects induced by the fundamental prompt mode. The modified area-ratio method, which requires direct numerical simulations of the time-dependent neutron fluxes subjected to thousands of neutron pulses, is difficult to apply in actual experiments.

The static approach suggested by Bell offers a direct way to obtain a spatial correction factor f. In this thesis, we derived f explicitly and named it as Bell's spatial correction factor. In addition, we have also demonstrated that f is very efficient in compensating for the spatial effects in the area-ratio method with FX2-TH simulations. However, the application of Bell's spatial correction factor f is limited because it cannot be used to explain the spatial dependence in the area-ratio method.

To obtain physical explanations of the spatial dependence in the area-ratio method, we have performed a complete modal analysis to identify the spatial effects induced by the prompt-neutron harmonics and the delayed-neutron harmonics, separately. Two spatial correction factors f_p and f_d are derived through our modal analysis. With FX2-TH simulations, we have demonstrated that a significant part of f_p comes from the difference between the high-order prompt α-modes and the fundamental k-mode, and the spatial effects induced by the high-order delayed-neutron harmonics are small.

As a good approximation to f, the correction factor f_p is simply obtained as the ratio of the fundamental k-mode flux $\phi_{0,k}$ and the time-integrated prompt flux $\hat{\phi}_p$, with the proper normalization applied. With this spatial correction factor, we can then provide physically intuitive explanations of the spatial dependence in the area-ratio method. Specifically, due to the different spatial distributions of $\hat{\phi}_p$ and $\phi_{0,k}$ in a subcritical reactor, the area-ratio method always overestimates the subcriticality at detector positions close to the external source, and underestimates the subcriticality at detector positions away from the source but in the fuel region. The true reactivity of the subcritical reactor can be bracketed by these two measured values. In addition, for the MUSE-4 experiments, we have performed Monte Carlo simulations to calculate f_p for the MUSE-4 SC0 subcritical reactor, and verified that f_p compensates well for the spatial effects in the experimental data.

Additionally, in this thesis, a full modal analysis is also performed for the extrapolated area-ratio method, where we also introduce two spatial correction factors $f_{p,e}$ and $f_{d,e}$ to account the spatial effects induced by prompt-neutron harmonics and delayed-neutron harmonics, respectively. The spatial effects in the extrapolated area-ratio method are mainly subject to the traditional kinetics distortion, i.e., the difference between the fundamental prompt α-mode and the fundamental k-mode. Therefore, the spatial correction for the extrapolated area-ratio method is large in regions where the kinetics distortions are significant, i.e., in the reflector or shield regions where materials have small neutron absorption cross sections, and is small in the fuel region where usually neutrons are easily absorbed.

The α-method is another way of obtaining the reactivity from pulsed-neutron experiments. The reactivity can be calculated directly with the fundamental neutron decay constant α_0 and the prior knowledge of the kinetics parameters, i.e., the mean generation time Λ and the effective delayed-neutron fraction β_{eff} of the subcritical reactor. Usually, α_0 is obtained by an exponential fitting of the experimental data for prompt neutrons after all high-order prompt-neutron harmonics decay away. However, for some subcritical systems, the fundamental mode is not well separated from the high-order harmonics in the experimental data, e.g., the MUSE-4 experiment. The decay constant obtained from the experimental data is then space- and time-dependent. In this situation, the modified α-method can be used to eliminate the spatial effects in the experimental data. For the MUSE-4 experiment, the modified α-method gives an almost uniform reactivity everywhere in the reactor. However, it also underestimates the subcriticality by about 2 \$ due to errors in the numerical model.

In a subcritical reactor, α_0 is determined by the decay rate of the slowest decay component in the detector responses, and the fundamental prompt α-mode describes its distribution in the space and energy domains. For the MUSE-4 experiment, we calculated the fundamental prompt α-mode for a 2-D model of the MUSE-4 SC0 subcritical reactor, and found that the slowest decay component in the detector responses peaks in the lead buffer and the accelerator beam pipe regions, due to the small thermal-neutron absorption cross sections in those regions. This slowest decay component is small, and most of prompt-neutrons in the reactor decays away with a rate much faster than α_0. To obtain the decay constant for most of the prompt-neutron in the reactor, we modeled a thin cadmium layer to wrap the buffer and the beam pipe in our numerical experiments. For this numerical model with the cadmium layer, the fundamental decay constant α_0 then represents the decay rate of the majority of the prompt neutrons after the neutron pulse is turned off.

Another difficulty of applying the α-method is to measure or calculate the kinetic parameters Λ and β_{eff}. In actual pulsed-neutron experiments, they are usually measured in a reference reactor which is close-to-critical. Our FX2-TH simulation shows that the mean generation time Λ increases significantly as the subcriticality increases. In order to obtain an accurate estimation of the reactivity, we proposed to calibrate the measured Λ with a correction factor f_Λ obtained from numerical calculations. For the 2-D numerical model with the cadmium layer, we showed that Λ of the MUSE-4 SC0 subcritical reactor differs from Λ of the close-to-critical reactor by more than 50%. With the decay constant α_0 obtained for most of the prompt neutrons in the reactor, and the calibrated Λ, the α-method yields reactivity of the MUSE-4 SC0 subcritical reactor -12.5 \$, which agrees well with the avearage value obtained from the area-ratio method after the spatial corrections.

The prompt α-modes and k-modes have been used extensively in our analysis of the spatial effects. Traditionally, the power iteration method is usually applied to calculate the fundamental and high-order k-modes. However, it is not efficient for high-order modes calculations. In this thesis, we have developed a code, which is combined with the ARPACK software, to successfully calculate the fundamental and high-order k- and α-modes of a 2-D diffusion problem with X-Y geometry. We have also implemented the BICGSTAB method together with the SSOR preconditioner in the code to solve the corresponding fixed-source equations for both the k- and the α-eignevalue problems. With the code we developed, we also demonstrated that in the MUSE-4 SC0 subcritical reactor, the fundamental prompt α-mode differs from the fundamental k-mode significantly at the low energy groups and in the shield and reflector regions, but the delayed α-mode agrees with the fundamental k-mode very well everywhere and at all energy groups.

Overall, in this thesis, we placed an emphasis on both accurate numerical analysis and developing physical insights into spatial effects in the pulsed-neutron techniques for reactivity measurements. We performed a complete modal analysis for the area-ratio method and the α-method. The spatial effects induced by the prompt-neutron harmonics and delayed-neutron harmonics are identified separately, and are first evaluated in this thesis with the fundamental and high-order prompt-neutron harmonics calculated by the Krylov subspace method. Meanwhile, with the capability of calculating the prompt-neutron harmonics, we also calibrated the measured mean generation time for a subcritical reactor in the α-method. Most importantly, we proposed a new spatial correction factor f_p for the area-ratio experiment, which is easy to calculate and can give physically intuitive explanations of the spatial dependence in the area-ratio method. The spatial effects in the MUSE-4 area-ratio experimental data are well compensated for by this spatial correction factor f_p.

8.2 Future work

In our study, IRAM is implemented with the 2-D diffusion code. However, there is no limitation to calculate the eigenvalues for a more complicated problem. The implementation for a full scale 3-D transport problem no doubt will help describe the subcritical reactor more accurately and requires more computational skills. In addition, as demonstrated in Chapter V, the inner iterative solvers with the preconditioner techniques which have been proposed in recent years, e.g., GMRES(m) and BICGSTAB, are superior to the traditional SOR method for many cases. Further investigations of those numerical methods in the nuclear engineering field will be another interesting topic.

In practical applications, pulsed-neutron experiments are only one of the methods to measure the reactivity of a subcritical reactor. The validity of other methods, e.g., the source-jerk method, the Rossi-α method and the Feynman-α method, for a subcritical system with $k \simeq 0.95$ or less also need to be evaluated more carefully.

APPENDICES

APPENDIX A

Iterative algorithms

A.1 The Successive Overrelaxation Method

The SOR method [41] searches for an estimation of x_k , such that $\|\mathbf{A}x_k - b\| < \epsilon\|b\|$, where $\mathbf{A} = \{a_{ij}\}$, $i = 1, \cdots I$, and $j = 1, \cdots J$:

1. With initial guess x_0, obtain $r_0 = b - \mathbf{A}x_0$;

2. Do while $\|r_k\| > \epsilon\|b\|$:

   For $i = 1, \cdots, I$:

   $$\begin{aligned} \hat{x} &= \frac{1}{a_{ii}}\left[b(i) - \sum_{j=1}^{i-1} a_{ij}x_k(j) - \sum_{j=i+1}^{J} a_{ij}x_{k-1}(j)\right] \\ \delta &= \hat{x} - x_{k-1}(i) \\ x_k(i) &= x_{k-1}(i) + \omega\delta \end{aligned}$$

   End For

   $r_k = b - \mathbf{A}x_k$.

3. End do, return x_k and r_k.

A.2 The Conjugate Gradient Method

The CG method [41] seeks an estimation of x_k, such that $\|\mathbf{A}x_k - b\| < \epsilon\|b\|$, where $\mathbf{A} = \{a_{ij}\}$, $i = 1, \cdots I$, and $j = 1, \cdots J$:

1. With initial guess x_0, obtain $r = b - \mathbf{A}x_0$, $p = r$
2. Do while $\|r\| > \epsilon\|b\|$:

$$\begin{aligned} \nu &= r^T r \\ \alpha &= \frac{\nu}{\langle p, Ap \rangle} \\ x &= x + \alpha * p \\ r &= r - \alpha * p \\ \beta &= \frac{r^T r}{\nu} \\ p &= r + \beta p \end{aligned}$$

3. End do, return r and x.

A.3 The Generalized Minimum RESidual Method

The GMRES(m) method [43] seeks an estimation of x_k, such that $\|\mathbf{A}x_k - b\| < \epsilon\|b\|$, where $\mathbf{A} = \{a_{ij}\}$, $i = 1, \cdots I$, and $j = 1, \cdots J$:

1. With initial guess x_0, obtain $r = b - \mathbf{A}x_0$, $\beta = \|r\|$, and $v_1 = r/\beta$.
2. Do while $\|r\| > \epsilon\|b\|$:

   For $i = 1, \cdots, m$

$$\begin{aligned} \omega_i &= \mathbf{A}v_i \\ h_{ij} &= \langle \mathbf{A}v_i, v_j \rangle \\ \omega_i &= \omega_i - h_{ij}v_j \quad j = 1, \cdots, i \\ h_{i+1,i} &= \|\omega_i\| \\ v_{j+1} &= \omega_i / h_{i+1,i} \end{aligned}$$

   End For

3. Solve the minimal problem $\|\beta e_1 - \bar{\mathbf{H}}_m y_m\|_2$ for y_m with the plane rotation method, and $x_m = x_0 + V_m y_m$.
4. $x_0 = x_m$, $r = b - \mathbf{A}x_0$, Go to 2.
5. End do, return x_m

A.4 The BiConjugate-Gradient STABilized Method

The BiCGSTAB method [43] seeks an estimation of x_k , such that $\|\mathbf{A}x_k - b\| < \epsilon\|b\|$, where $\mathbf{A} = \{a_{ij}\}$, $i = 1, \cdots I$, and $j = 1, \cdots J$:

1. With initial guess x_0, obtain $r_0 = b - \mathbf{A}x_0$, $r^* = r_0$, $p_0 = r_0$
2. Do while $\|r_k\| > \epsilon\|b\|$:

$$\begin{aligned}
\alpha_k &= \frac{\langle r_k, r^* \rangle}{\langle \mathbf{A}p_k, r^* \rangle} \\
s_k &= r_k - \alpha_k * \mathbf{A}p_k \\
\omega_k &= \frac{\langle \mathbf{A}s_k, s_k \rangle}{\langle \mathbf{A}s_k, \mathbf{A}s_k \rangle} \\
x_{k+1} &= x_k + \alpha_k p_k + \omega_k s_k \\
r_{k+1} &= s_k - \omega_k \mathbf{A}s_k \\
\beta_k &= \left[\frac{\langle r_{k+1}, r^* \rangle}{\langle r_k, r^* \rangle}\right]\left[\frac{\alpha_k}{\omega_k}\right] \\
p_{k+1} &= r_{k+1} + \beta_k * (p_k - \omega_k \mathbf{A}p_k)
\end{aligned}$$

3. End do, return x_k and r_k

APPENDIX B

The Preconditioning Technique

B.1 The Symmetric Successive Overrelaxation Preconditioner

The SSOR preconditioner [41] tries to solve the equation $y = \mathbf{M}^{-1}x$, in which $\mathbf{M}$ is the SSOR M matrix of $\mathbf{A} = \{a_{ij}\}$, given x :

1. With initial guess $y_0 = 0$,
2. For $i = 1, \cdots, I$:

$$
\begin{aligned}
\hat{y} &= \frac{1}{a_{ii}}\left[x(i) - \sum_{j=1}^{i-1} a_{ij}y_(j)\right] \\
y_(i) &= \omega\hat{y}
\end{aligned}
$$

   END For

3. For $i = I, \cdots, 1$:

$$
\begin{aligned}
\hat{y} &= \frac{1}{a_{ii}}\left[y(i) - \sum_{j\neq i}^{I} a_{ij}y_(j)\right] \\
\delta &= \hat{y} - y(i) \\
y_(i) &= y(i) + \omega\delta
\end{aligned}
$$

   END For

4. return y.

B.2 The Incomplete LU preconditioner

The incomplete LU-factorization preconditioner at zero fill-ins [41] is realized to solve the equation $y = \mathbf{M}^{-1}x$, in which $\mathbf{M}$ is the ILU(0) M matrix of $\mathbf{A} = a_{ij}$, given x.

To realize the preconditioner, the LU decompositions of $\mathbf{A}$ is first performed only at positions $a_{ij} \neq 0$, and the $\mathbf{M}$ is stored in matrix $\mathbf{A}$, and then y is obtained by the forward and backward substitution.

```
1. For $i = 2, \cdots, I$
     For $k = 1, \cdots, i-1$
     If $a_{ik} \neq 0$ Then
       $a_{i,k} = a_{i,k}/a_{k,k}$
       For $j = k+1, \cdots, J$
       If $a_{ij} \neq 0$ Then
         $a_{i,j} = a_{i,j} - a_{i,k} * a_{k,j}$
       End If
       End For
     End If
     End For
   End For
2. Forward substitution
   For $i = 1, \cdots, I$
```

$$y(i) = x(i) - \sum_{j=1}^{i-1} a_{ij} y(j)$$

End For

3. Backward substitution For $i = I, \cdots, 1$

$$y(i) = \frac{1}{a_{ii}} \left[x(i) - \sum_{j=i+1}^{J} a_{ij} y(j) \right]$$

End For

4. return y.

APPENDIX C

The numerical model of the RZ reactor in the FX2-TH simulation

Table C.1: Four-group macroscopic cross sections of the core material for the RZ reactor.

Energy Group	1	2	3	4
Σ_{tr} (cm^{-1})	1.4993E-01	2.9008E-01	4.8085E-01	1.2633E+00
Σ_{rm} (cm^{-1})	7.1226E-02	7.4597E-02	8.6783E-02	1.1085E-01
Σ_{f} (cm^{-1})	2.2711E-03	6.3646E-04	7.8058E-03	6.0643E-02
$\Sigma_{\nu f}$ (cm^{-1})	6.3334E-03	1.5563E-03	1.8881E-02	1.4668E-01
$\Sigma_{s,i\rightarrow i+1}$ (cm^{-1})	6.8312E-02	7.2630E-02	6.3705E-02	$\cdots$
χ_p	7.5560E-01	2.4382E-01	1.8078E-04	0.0000E-04
χ_d	7.5560E-01	2.4382E-01	1.8078E-04	0.0000E-04
$v(cm/s)$	1.9600E+09	4.6400E+08	6.2300E+06	4.2600E+05
Σ_{d} (cm^{-1})	0.0045	0.0069	0.00961	0.8925

Table C.2: Four-group macroscopic cross sections of the reflector material for the RZ reactor.

Energy Group	1	2	3	4
Σ_{tr} (cm^{-1})	3.0269E-01	6.5237E-01	1.2142E+00	2.1988E+00
Σ_{rm} (cm^{-1})	1.1803E-01	1.1650E-01	1.2663E-01	1.4449E-01
$\Sigma_{s,i\rightarrow i+1}$ (cm^{-1})	1.1664E-01	1.1564E-01	1.1187E-01	$\cdots$

Table C.3: Delayed neutron parameters for the RZ reactor.

Group	1	2	3	4	5	6
β	2.575E-04	1.4853E-03	1.3378E-03	2.9204E-03	9.8550E-04	2.1926E-04
λ	.0127	.0318	.1178	.3152	1.4015	3.9056

REFERENCES

REFERENCES

[1] International Atomic Energy Agency (IAEA), "Latest news related to PRIS and the status of nuclear power plants" (2008). [Online]. Available: http://www.iaea.org/programmes/a2/index.html.

[2] J. J. DuDerstadt and L. J. Hamilton, *Nuclear reactor analysis*, John Willey & Sons (1976).

[3] World Nuclear Association (WNA), "The nuclear fuel cycle" (2008). [Online]. Available: http://www.world-nuclear.org/info/inf03.html.

[4] National Nuclear Data Center (NNDC), "Chart of nuclides." [Online]. Available: http://www.nndc.bnl.gov/chart/.

[5] H. Nifenecker, O. Meplan, and S. David, *Accelerator driven subcritical reactors*, Institute of Physics Publishing (2003).

[6] British Geological Survey (BGS), "Mineral profile: Uranium," Nature Environment Research Council (2007).

[7] R. C. Ewing and A. Macfarlane, "NUCLEAR WASTE: Yucca mountain," *Science*, **296**, 659 (2002).

[8] R. C. Ewing, "Nuclear waste forms for actinides," *Proceedings of the National Academy of Sciences*, **96**, 3432 (1999).

[9] A. Hedin, "SKB technical report 97-13," Swedish Nuclear Fuel and Waste Management Co., Stockholm (1997).

[10] M. Salvatores, I. Slessarev, and M. Uematsu, "A global physics approach to transmutation of radioactive nuclei," *Nuclear Science and Engineering*, **116**, 1 (1994).

[11] D. Hill, G. V. Tuyle, D. Beller, B. Bishop, T. Cotton, P. Finck, B. Halsey, J. Herczeg, J. S. Herring, D. Lancaster, J. March-Leuba, H. Ludewig, T. Sanders, B. Savage, E. Schweitzer, C. Smith, L. Stewart, M. Todosow, and C. Walter, "A Roadmap for developing ATW technology: systems scenarios & integration: report of the ATW roadmap systems scenarios & integration technical working group," ANL-99/16 (1999).

[12] A. F. Henry, *Nuclear reactor analysis*, The MIT Press (1975).

[13] M. Salvatores and et al., "MUSE-1: A first experiment at MASURCA to validate the physics of sub-critical multiplying systems relevant to ADS." *Second International Conference on Accelerator-Driven Transmutaion Technologies and Applications* (1996).

[14] C. Destouches, M. Fruneau, J. Belmont, J. Do Pinhal, S. Albrand, J. Carreta, P. Chaussonnet, J. De Conto, A. Fontenille, P. Fougeras, A. Garrigue, M. Guisset, J. Laurens, J. Loiseaux, D. Marchand, R. Micoud, F. Mellier, E. Perbet, M. Planet, J. Ravel, and J. Richaud, "The GENEPI accelerator operation feedback at the MASURCA reactor facility," *Nuclear Instruments and Methods in Physics Research Section A: Accelerators, Spectrometers, Detectors and Associated Equipment Proceedings of the 7th International Conference on Accelerator Applications - AccApp05*, **562**, 601 (2006).

[15] D. Villamarn, "Anlisis dinmico del reactor experimental de fisinnuclear MUSE-4," Ph.D. dissertation, Universidad Complutense de Madrid (2004).

[16] M. Carta, A. D'Angelo, V. Peluso, G. Aliberti, G. Imel, V. Kulik, G. Palmiotti, J. Lebrat, Y. Rugama, C. Destouches, E. Gonzalez-Romero, D. Villamarin, S. Dulla, F. Gabrielli, P. Ravetto, and M. Salvatores, "Reactivity assessment and spatial time-effects from the MUSE kinetics experiments," *Proceedings of the PHYSOR 2004: The Physics of Fuel Cycles and Advanced Nuclear Systems - Global Developments*, 657 (2004).

[17] V. V. Kulik and J. C. Lee, "Space-time correction for reactivity determination in source-Driven subcritical systems," *Nuclear Science and Engineering*, **153**, 69 (2006).

[18] T. Gozani, "A modified procedure for the evaluation of pulsed source experiments in subcritical reacotrs," *Nukleonik*, **4**, 348 (1962).

[19] C. Masters and K. Cady, "A procedure for evaluating modified pulsed-neutron-source experiments in subcritical nuclear reactors," *Nuclear Science and Engineering*, **29**, 272 (1967).

[20] T. Gozani, "Consistent subcritical fast reactor kinetics," *Dynamics of Nuclear Systems, University of Arizaona Press, Tucson.*, 109 (1972).

[21] G. Kosaly and J. Valko, "Remarks on the use of well-known reactivity measuring techniques by the pulsed-source method," *Annals of Nuclear Energy*, **2**, 477 (1975).

[22] C. Preskitt, E. Nephew, J. Brown, and K. Van Howe, "Interpretation of pulsed-source experiments in peach bottom HTGR," *Nuclear Science and Engineering*, **29**, 283 (1967).

[23] M. El-Zeftawy and L. Ruby, "Kinetics distortion in a TRIGA reactor with an asymmetric relfector." *Nuclear Science and Engineering*, **45**, 335 (1971).

[24] G. I. Bell and S. Glasstone, *Nuclear reactor theory*, Van Nostrand Reinhold Company (1970).

[25] E. Larsen, "The spectrum of the multigroup neutron transport operator for bounded spatial domains," *Joural of Mathematical Physics*, **20**, 1776 (1979).

[26] T. M. Sutton and B. Aviles, "Diffusion theory methods for spatial kinetics calculations," *Progress in Nuclear Energy*, **39**, 119 (1996).

[27] R. A. Shober, D. R. Ferguson, and T. A. Daly, "FX2: A two-dimensional nuclear reactor kinetics code with thermal and hydraulics feedback," Argonne National Laboratory, ANL-78-97 (1978).

[28] G. Rampault, D. Plisson, J. Tommasi, R. Jacqmin, J. M. Rieunier, D. Verrier, and D. Biron, "The ERANOS code and data system for fast reactor neutronic analyses," *Proc. Reactor Physics Topl. Mtg. (PHYSOR 2002), Seoul, Korea* (2002).

[29] G. Rimpault, "Algorithmic features of the ECCO cell code for treating heterogeneous fast reactor subassemblies," *Proc. Intl. Conf. Mathematics and Computations, Reactor Physics, and Environmental Analyses, Portland, Oregon, American Nuclear Society* (1995).

[30] G. Palmiotti, C. B. Carrico, and E. E. Lewis, "Variational nodal methods with anisotropic scattering," *Nuclear Science and Engineering*, **115** (1993).

[31] A. Rineiski and J. Y. Doriath, "Time-dependent neutron transport with variational nodal method," *Proc. Int. Conf. Mathematical Methods and Supercomputing for Nuclear Applications, Saratoga, Springs, New York, American Nuclear Society* (1997).

[32] N. Sjostrand, "Measurements on a subcritical reactor using a pulsed neutron source," *Arkiv for Fysik*, **11**, 233 (1956).

[33] M. Isbasescu, “On the physical foundations of the method of Sjostrand for reactivity measurement by the pulsed neutron technique,” *Annals of Nuclear Energy*, **4**, 193 (1977).

[34] M. Becker and K. Quisenberry, “The spatial dependence of pulsed-neutron reactivity measurements,” *Symposium on Neutron Dynamics and Control, Tucson, Ariz.* (1964).

[35] T. Gozani, “The concept of reactivity and its application to kinetic measurements,” *Nukleonik*, **5**, 55 (1963).

[36] S. Kaplan, “The property of finality and the analysis of problems in reactor space-time kinetics by various modal expansions,” *Nuclear Science and Engineering*, **9**, 857 (1961).

[37] R. S. Modak and A. Gupta, “A scheme for the evaluation of dominant time-eigenvalues of a nuclear reactor,” *Annals of Nuclear Energy*, **34**, 213 (2007).

[38] R. B. Lehoucq, D. C. Sorensen, and C. Yang, “ARPACK user’s guide,” *Society for Industrial and Applied Mathematics,Philadelphia, Pennsylvania* (1998).

[39] D. Lathouwers, “Iterative computation of time-eigenvalues of the neutron transport equation,” *Annals of Nuclear Energy*, **30**, 1793 (2003).

[40] J. S. Warsa, T. A. Wareing, J. E. Morel, and J. M. McGhee, “Krylov subspace iterations for deterministic k-eigenvalue calculations,” *Nuclear Science and Engineering*, **147**, 26 (2004).

[41] D. S. Watkins, *Fundamentals of matrix computations, second ed.*, John Wiley & Sons (2002).

[42] C. C. Paige and M. A. Saunders, “LSQR: An algorithm for sparse linear equations and sparse least squares,” *ACM Transactions on Mathematical Software*, **8**, 43 (1982).

[43] Y. Saad, *Iterative methods for sparse linear systems, second ed.*, SIAM (2003).

[44] H. A. v. d. Vorst, “BI-CGSTAB: a fast and smoothly converging variant of BI-CG for the solution of nonsymmetric linear systems,” *SIAM Journal on Scientific and Statistical Computing*, **13**, 631 (1992).

[45] C. Lanczos, “Chebyshev plolynomials in the solution of large-scale linear sytems,” *Toronto symposium on computing techniquies*, 124 (1952).

[46] Y. Saad and H. A. van der Vorst, “Iterative solution of linear systems in the 20th century,” *Journal of Computational and Applied Mathematics*, **123** (2000).

[47] W. W. Little Jr. and R. W. Harie, “2DB - A two-dimensional fast reactor burnup code,” *Nuclear Science and Engineering*, **32**, 275 (1968).

[48] Westinghouse, “AP600 standard safety analysis report,” Westinghouse Electric Corp., DE-AC03-90SF18495 (2003).

[49] Y. Cao and J. Lee, “An improved modal-local method for ADS transient analysis,” *Transactions of the American Nuclear Society*, **96**, 675 (2007).

[50] F. Perdu, J. M. Loiseaux, A. Billebaud, R. Brissot, D. Heuer, C. Lebrun, E. Liatard, O. Meplan, E. Merle, H. Nifenecker, and J. Vollaire, “Prompt reactivity determination in a subcritical assembly through the response to a dirac pulse,” *Prongress in Nuclear Energy*, **42**, 107 (2003).

[51] G. Palmiotti, J. M. Rieunier, C. Gho, and M. Salvatores, “BISTRO optimized two dimensional Sn transport code,” *Nuclear Science and Engineering*, **104** (1990).

[52] T. E. Booth, J. T. Goorley, A. Sood, F. B. Brown, and et al., “MCNP-A general monte carlo N-particle transport code, version 5,” Los Alamos National Laboratory, LA-UR-03-1987 (2003).

[53] G. Aliberti, G. Rimpault, R. Jacqmin, J. F. Lebrat, P. J. Finck, G. Imel, A. Rineiski, P. Ravetto, and J. C. Sens, "Dynamic measurements and control of an Accelerator Driven System (ADS)," *Physor02* (2002).